VILNIUS GEDIMINAS TECHNICAL UNIVERSITY

Oleksandr MASALSKYI

INVESTIGATION AND APPLICATION OF HOT CARRIER PHENOMENON IN PHOTOVOLTAICS

DOCTORAL DISSERTATION

TECHNOLOGICAL SCIENCES
ELECTRICAL AND ELECTRONIC ENGINEERING (T 001)

Vilnius, 2023

The doctoral dissertation was prepared at Vilnius Gediminas Technical University in 2019–2023.

Supervisor

Assoc. Prof. Dr Jonas GRADAUSKAS (Vilnius Gediminas Technical University, Electrical and Electronic Engineering – T 001).

Consultant

Assoc. Prof. Dr Dainius JASAITIS (Vilnius Gediminas Technical University, Environmental Engineering – T 004).

The Dissertation Defence Council of Scientific Field of Electrical and Electronic Engineering of Vilnius Gediminas Technical University:

Chairman

Prof. Dr Darius PLONIS (Vilnius Gediminas Technical University, Electrical and Electronic Engineering – T 001).

Members:

Prof. Dr Habil. Marek GODLEWSKI (Institute of Physics of the Polish Academy of Sciences, Physics – N 002),
Dr Šarūnas MEŠKINIS (Kaunas University of Technology, Materials Engineering – T 008),
Prof. Dr Voitech STANKEVIČ (Vilnius Gediminas Technical University, Electrical and Electronic Engineering – T 001),
Prof. Dr Nerija ŽURAUSKIENĖ (Vilnius Gediminas Technical University, Electrical and Electronic Engineering – T 001).

The dissertation will be defended at the public meeting of the Dissertation Defence Council of the Scientific Field of Electrical and Electronic Engineering in the SRA-I Meeting Hall of Vilnius Gediminas Technical University at **9 a.m. on 15 December 2023**.

Address: Saulėtekio al. 11, LT-10223 Vilnius, Lithuania.
Tel.: +370 5 274 4956; fax +370 5 270 0112; e-mail: doktor@vilniustech.lt

A notification on the intended defence of the dissertation was sent on 9 January 2023. A copy of the doctoral dissertation is available for review at Vilnius Gediminas Technical University repository https://etalpykla.vilniustech.lt and the Library of Vilnius Gediminas Technical University (Saulėtekio al. 14, LT-10223 Vilnius, Lithuania) and at the Library of State Research Institute Center for Physical Sciences and Technology (Saulėtekio al. 3, LT-10257 Vilnius, Lithuania).

Vilnius Gediminas Technical University book No 2023-046-M

doi:10.20334/2023-046-M

© Vilnius Gediminas Technical University, 2023
© Oleksandr Masalskyi, 2023
oleksandr.masalskyi@vilniustech.lt

VILNIAUS GEDIMINO TECHNIKOS UNIVERSITETAS

Oleksandr MASALSKYI

KARŠTŲJŲ KRŪVININKŲ REIŠKINIO TYRIMAS IR PANAUDOJIMAS FOTOVOLTIKOJE

DAKTARO DISERTACIJA

TECHNOLOGIJOS MOKSLAI,
ELEKTROS IR ELEKTRONIKOS INŽINERIJA (T 001)

Vilnius, 2023

Disertacija rengta 2019–2023 metais Vilniaus Gedimino technikos universitete.

Vadovas

doc. dr. Jonas GRADAUSKAS (Vilniaus Gedimino technikos universitetas, elektros ir elektronikos inžinerija – T 001).

Konsultantas

doc. dr. Dainius JASAITIS (Vilniaus Gedimino technikos universitetas, aplinkos inžinerija – T 004).

Vilniaus Gedimino technikos universiteto Elektros ir elektronikos inžinerijos mokslo krypties disertacijos gynimo taryba:

Pirmininkas

prof. dr. Darius PLONIS (Vilniaus Gedimino technikos universitetas, elektros ir elektronikos inžinerija – T 001).

Nariai:

prof. habil. dr. Marek GODLEWSKI (Lenkijos mokslų akademijos Fizikos institutas, Lenkija, fizika – N 002),
dr. Šarūnas MEŠKINIS (Kauno technologijos universitetas, medžiagų inžinerija – T 008),
prof. dr. Voitech STANKEVIČ (Vilniaus Gedimino technikos universitetas, elektros ir elektronikos inžinerija – T 001),
prof. dr. Nerija ŽURAUSKIENĖ (Vilniaus Gedimino technikos universitetas, elektros ir elektronikos inžinerija – T 001).

Disertacija bus ginama viešame elektros ir elektronikos inžinerijos mokslo krypties disertacijos gynimo tarybos posėdyje **2023 m. gruodžio 15 d. 9 val.** Vilniaus Gedimino technikos universiteto SRA-I Posėdžių salėje.

Adresas: Saulėtekio al. 11, LT-10223 Vilnius, Lietuva.
Tel.: (8 5) 274 4956; faksas (8 5) 270 0112; el. paštas doktor@vilniustech.lt

Pranešimai apie numatomą ginti disertaciją išsiųsti 2023 m. lapkričio 14 d.

Disertaciją galima peržiūrėti Vilniaus Gedimino technikos universiteto talpykloje https://etalpykla.vilniustech.lt ir Vilniaus Gedimino technikos universiteto bibliotekoje (Saulėtekio al. 14, LT-10223 Vilnius, Lietuva) ir Valstybinio mokslinių tyrimų instituto Fizinių ir technologijos mokslų centro bibliotekoje (Saulėtekio al. 3, LT-10257 Vilnius, Lietuva).

Abstract

The dissertation analyses the direct impact of the hot carrier phenomenon on the operation of a single-junction solar cell. Ways to suppress the influence of the hot carrier effect are determined based on the achieved results. The structure of the ratchet-based sensor operating on the hot carrier effect is modelled, and its prototype is produced.

The dissertation includes an introduction, three main chapters, general conclusions, a list of used references, and the author's publications related to the dissertation topic.

The first chapter is an overview of the literature on the dissertation topic. This chapter observes the basic parameters of solar cells and possible losses. The structures of the first and second generation of solar cells are reviewed. Modern structures of third-generation solar cells that can minimise spectral losses are analysed. The last paragraph explains the formation of the hot carrier photocurrent under the action of infrared light in various semiconductor structures.

The second chapter represents methodologies used to achieve the obtained results. The chapter describes the manufacturing technology of the samples, the method of detecting the photo signal, the selected computer software and the arrangement of the experimental setup.

The third chapter gives an overview and explanation of the achieved results. The chapter analyses the hot carrier phenomenon's peculiarities and describes how to suppress its influence in a single junction solar cell. The chapter presents a modelled structure and the developed prototype of an electromagnetic radiation sensor operating based on the hot carrier effect.

The results of the dissertation have been reported in fourteen scientific publications. Three of them have been published in journals with refereed Clarivate Analytics Web of Science databases refereed journals with a citation index, one in conference proceedings, and ten peer-reviewed in other scholarly journals. The author has made eight presentations at international, regional and local scientific conferences and symposiums.

Reziumė

Disertacijoje analizuojamas tiesioginis karštųjų krūvininkų poveikis vienos sandūros saulės elemento veikimui. Remiantis pasiektais rezultatais yra nustatyti būdai, leidžiantys slopinti karštųjų krūvininkų įtaką. Sumodeliuotas reketinis jutiklis, veikiantis karštųjų krūvininkų reiškinio pagrindu, ir pagamintas jo prototipas.

Disertaciją sudaro įvadas, trys pagrindiniai skyriai, bendrosios išvados, naudotų šaltinių sąrašas ir autoriaus publikacijos, susijusios su disertacijos tema.

Pirmajame skyriuje pateikiama literatūros apžvalga disertacijos tema. Šiame skyriuje apžvelgiami pagrindiniai saulės elementų parametrai ir galimi nuostoliai. Aptariamos pirmosios ir antrosios kartos saulės elementų struktūros. Analizuojami modernūs trečiosios kartos saulės elementai, galintys sumažinti spektrinius nuostolius. Paskutinėje pastraipoje paaiškinama, kaip įvairiuose puslaidininkiniuose dariniuose susidaro karštųjų krūvininkų fotosrovė veikiant infraraudonajai spinduliuotei.

Antrajame skyriuje paaiškinmos metodikos, taikytos siekiant rezultatų. Skyriuje aprašoma bandinių gamybos technologija, fotosignalo matavimo metodas, pasirinktoji kompiuterinė programinė įranga ir eksperimento schema.

Trečiajame skyriuje pateikiama pasiektų rezultatų apžvalga ir jų paaiškinimai. Šiame skyriuje analizuojami karštųjų krūvininkų reiškinio ypatumai ir aprašomi būdai, leidžiantys slopinti jo įtaką vienos sandūros saulės elemento veikimui. Skyriuje aprašomi elektromagnetinės spinduliuotės jutiklio sumodeliuota struktūra ir sukurtas jo prototipas, veikiantis karštųjų krūvininkų reiškinio pagrindu.

Disertacijos rezultatai paskelbti keturiolikoje mokslinių publikacijų: trys iš jų išspausdinti recenzuojamuose mokslo žurnaluose, įtrauktuose į *Clarivate Analytics Web of Science* sąrašą ir turinčiuose citavimo rodiklį, vienas konferencijos medžiagoje, dešimt – kituose recenzuojamuose žurnaluose. Rezultatus autorius pristatė aštuoniose tarptautinėse, regioninėse ir nacionalinėse mokslinėse konferencijose ir simpoziumuose.

Notations

Abbreviations

AM – air mass (liet. oro masė);
AC – alternating current (liet. kintamoji srovė);
DC – direct current (liet. nuolatinė srovė);
e-gas – electronic gas (liet. elektronų dujos);
HC – hot carrier (liet. karštasis krūvininkas);
PSi – porous silicon (liet. akytas silicis);
I–*V* – current–voltage (liet. voltamperinė (charakteristika));
l–*h* – light and heavy (doped) (liet. silpnai ir stipriai (legiruotas));
PV – photovoltaics (liet. fotovoltika);
SC – solar cell (liet. saulės elementas).

Contents

INTRODUCTION 1
Problem Formulation 1
Relevance of the Dissertation 2
Research Object 2
Aim of the Dissertation 2
Tasks of the Dissertation 2
Research Methodology 3
Scientific Novelty of the Dissertation 3
Practical Value of the Research Findings 3
Defended Statements 4
Approval of the Research Findings 4
Structure of the Dissertation 5
Acknowledgement 5

1. REVIEW OF SOLAR CELL STRUCTURES AND HOT CARRIER PHENOMENON 7
1.1. History of Photovoltaics 7
1.2. Solar Spectrum for the Solar Cells 9
1.3. Fundamental Characteristics of a Solar Cell 10
1.4. Limitations and Basic Losses of Solar Cells 12
1.5. Classification of the Solar Cells 14
1.5.1. Single-junction Solar Cells 16
1.5.2. Thin film silicon Solar Cells 17

1.5.3. Perovskite Solar Cells 17
1.5.4. Multi-junction Solar Cells 18
1.5.5. Perovskite tandem Solar Cells 19
1.5.6. Quantum well Solar Cells 20
1.5.7. Hot carrier Solar Cells 21
1.6. Hot carriers and hot carrier photoresponse 22
1.6.1. Methods of hot carrier excitation 23
1.6.2. Process of hot carrier energy dissipation 24
1.6.3. Hot carrier photo signal across germanium p–n junction 26
1.6.4. Photocurrent of hot carrier across gallium arsenide p–n junction 27
1.6.5. Hot carrier photo signal across homogeneous gallium arsenide junction 29
1.6.6. Hot carrier photo signal across mercury cadmium telluride p–n junction 31
1.6.7. Hot carrier photo signal across indium antimonide p–n junction 33
1.7. Conclusions of the First Chapter and Formulation of the Dissertation Tasks 35

2. FABRICATION TECHNOLOGY OF THE SAMPLES AND RESEARCH METHODOLOGY 37
2.1. Fabrication of the samples 38
2.1.1. Gallium arsenide p–n junction diodes 38
2.1.2. Polycrystalline silicon industrial Solar Cells 38
2.1.3. Porous silicon diodes containing porous silicon surface layer 39
2.1.4. Ratchet-based sensor 40
2.2. Experimental setup 41
2.3. Program software 44
2.4. Conclusions of the Second Chapter 45

3. RESULTS OF INVESTIGATION OF THE HOT CARRIER EFFECT 47
3.1. Dependence of hot carrier photocurrent on the bias voltage 48
3.2. Composition of photovoltage signal across gallium arsenide p–n junction 51
3.3. Temperature dependence of hot carrier photocurrent across gallium arsenide p–n junction 56
3.4. Modelling of absorption spectra 64
3.5. Suppression of hot carrier impact using porous silicon layer 68
3.6. Ratchet-based gallium arsenide/aluminium gallium arsenide electromagnetic radiation sensor 71
3.7. Conclusions of the Third Chapter 76

GENERAL CONCLUSIONS 79

REFERENCES 81

LIST OF SCIENTIFIC PUBLICATIONS BY THE AUTHOR ON THE TOPIC OF THE DISSERTATION 89

SUMMARY IN LITHUANIAN 93

Introduction

Problem Formulation

Actions to increase the efficiency of a solar cell (SC) have been actively investigated in the past decades. A single *p–n* junction solar cell still has not reached the Shockley-Queisser limit of 33%, mainly because of intrinsic losses in the SC. A major part of the intrinsic losses (about 80%) is attributed to photons having energy below the band gap (spectral loss) and thermalisation loss (Hirst & Ekins-Daukes, 2011). The spectral loss is not accounted for in the Shockley-Queisser theory, potentially heats the free carriers. The thermalisation loss is induced by the absorption of photons with energy higher than the band gap. The excess photon energy is the difference between the photon energy and the width of the band gap, and it goes to the carrier heating followed by the lattice heating.

Novel modern SC structures (third generation of SCs), such as ones containing quantum well layers, multi-junctions, and others, allow for avoiding spectral loss and using the excess photon energy effectively. For instance, hot carrier SCs effectively utilise hot carrier energy and have a perspective to reach 66% efficiency, thus overcoming the Shockley-Queisser limit (Ross & Nozik, 1998). Unfortunately, these modifications are far away from implementation on an industrial scale.

Relevance of the Dissertation

Solar cells of the third generation are promising solutions that allow for the use of the solar spectrum more productively, which gives the possibility to boost a cell's efficiency (Akinoglu et al., 2021). Unfortunately, the price of third-generation solar cells is much higher than first and second-generation industrial SCs. However, in typical solar cells, a significant part of the absorbed solar spectrum (up to 55%) is potentially involved in the carrier heating process (Masalskyi & Gradauskas, 2022).

The deeper research into the nature of the hot carrier (HC) effect in a single junction cell can open ways to increase the efficiency of industrial SCs. Furthermore, the unavoidable presence of the hot carrier effect can be a notable reason for calling to revise the Shockley-Queisser limit of a single junction solar cell. Finally, radiation sensors operating based on the hot carrier effect have great potential to become a new word in solutions of electromagnetic radiation detection.

Research Object

The object of the research is the hot carrier effect in *p–n* diodes and its application in semiconductor structures for the detection of electromagnetic radiation.

Aim of the Dissertation

The dissertation aims to investigate the characteristics and impact of the hot carrier phenomenon in a single *p–n* junction solar cell and to develop a sensor of electromagnetic radiation operating based on the hot carrier effect.

Tasks of the Dissertation

To realise the aim of the dissertation, the following tasks need to be achieved:

1. To design a model that makes it possible to define the direct influence and to analyse the hot carrier impact on the total signal of a solar cell.
2. To simulate the absorption spectrum of solar cells by considering the carrier heating process.
3. To unclose the ways of leading to reduced influence of HC effect in SCs.
4. To develop a structure and produce an infrared sensor operating based on the hot carrier phenomenon.

Research Methodology

Experimental, quantitative, and analytical methodologies were chosen to investigate the object: the rise of an HC photoresponse across the p–n junction has been revealed. Fabricated samples were investigated in photocurrent mode. The developed model helped to look into the process of photoresponse formation across a p–n junction and to separate the signal of an SC into its components. The investigated samples were illuminated by pulsed neodymium-doped yttrium aluminium garnet laser of 1.064 μm wavelength and neodymium-doped yttrium orthovanadate laser of 1.342 μm wavelength. The signals were detected using Agilent Technologies DSO6102A. The investigated GaAs p–n photodiodes and the GaAs/AlxGa1-xAs sensor were grown using liquid phase epitaxy, and the silicon p–n junctions were taken from industrial silicon SCs (SoliTek, Vilnius, Lithuania).

Scientific Novelty of the Dissertation

The scientific novelties of the dissertation are as follows:

1. The model allowing the division of the photoresponse signal of a solar cell into its components that are caused by electron–hole generation, carrier heating and lattice heating was designed.
2. The spectrum absorbed by a single junction solar cell was modelled. It defines the portion of the solar spectrum potentially heating-free carriers.
3. The method of calculating hot carrier temperature by employing the temperature dependence of voltage drop coefficient of a *p–n* junction current–voltage (I–V) characteristic was suggested.
4. The negative effect of hot carriers on the output signal of an industrial single-junction solar cell was detected.
5. The ratchet-based GaAs/$Al_xGa_{1-x}As$ sensor of electromagnetic radiation operating based on the hot carrier effect was developed.

Practical Value of the Research Findings

The obtained results have remarkable practical importance.

The model of signal separation in a solar cell into its components helps to evaluate the direct hot carrier impact on the net photoresponse.

Revealing the influence of the HC effect in industrial solar cells is a reason for revising the maximum theoretical efficiency of a single-junction solar cell.

The formation of a graded gap surface layer can suppress the impact of the HC effect.

The ratchet-based GaAs/$Al_xGa_{1-x}As$ sensor operating based on the hot carrier effect manifests itself as a promising device for the detection of infrared radiation.

Defended Statements

According to the results, statements are expressed as hypotheses to be defended:

- The net photocurrent across a *p–n* junction results from simultaneous processes of electron–hole pair generation, lattice heating and free carrier heating; the latter exerts a negative impact on the operation of a single junction solar cell because the direction of hot carrier photocurrent is always opposite to the classical carrier generation-induced.
- Hot carrier photocurrent across GaAs *p–n* junction at ambient temperature 300 K biased up to +0.7 V has a recombination nature when the hot carrier temperature is 454 K.
- Radiation of the below-band gap photon energy heats the free carriers and amounts to up to 10% of the whole absorbed solar spectrum energy in Si and GaAs 5 μm-thick emitter surface layer of a single-junction solar cell; this effect is stronger in heavier doped and thicker emitter layers.
- The developed ratchet-based GaAs/$Al_xGa_{1-x}As$ graded gap structure, operating based on the hot carrier effect, detects infrared radiation of 1.064 μm wavelength, demonstrating $2 \times 10^{-8} \frac{A}{W}$ sensitivity at room temperature.

Approval of the Research Findings

The results of the dissertation have been reported in 14 scientific publications. Three were published in journals with refereed *Clarivate Analytics Web of Science* databases refereed publications with a citation index, one in conference proceedings, and ten were peer-reviewed publications (abstracts) in other peer-reviewed scientific journals.

The author has made eight presentations at international, regional and local scientific conferences and symposiums:

- 18th International Young Scientist Conference Developments in Optics and Communications (DOC 2022), Riga, Latvia.
- Conference of Young Scientists on Semiconductor Physics (Lashkaryov's readings 2021), Kyiv, Ukraine.

- Sixth International Conference on Sensors and Electronic Instrumentation Advances (SEIA 2020), Porto, Portugal.
- 23rd Sde Boker Symposium on Solar Electricity Production, Midreshet Ben Gurion, Israel.
- 65th International Conference for Students of Physics and Natural Sciences (Open Readings 2022), Vilnius, Lithuania.
- 44th Lithuanian National Physics Conference, Vilnius, Lithuania.
- 17th International Young Scientist Conference Developments in Optics and Communications (DOC 2021), Riga, Latvia.
- 64th International Conference for Students of Physics and Natural Sciences (Open Readings 2021), Vilnius, Lithuania.

Structure of the Dissertation

The dissertation includes an introduction, analytical literature review, discussion of research methodology, summarized investigation results and conclusions, references, annexes of scientific articles, and a summary in Lithuanian.

The total scope of the dissertation is 116 pages, and contains 43 equations, 53 figures, four tables and 84 references.

Acknowledgement

My sincerest gratitude goes to:

Assoc. Prof. Dr Jonas Gradauskas for the assistance of the research.

Assoc. Prof. Dr Dainius Jasaitis for advising me during my research.

Dr Jovita Damauskaitė, Prof. Dr Artūras Jukna, Prof. Dr Darius Plonis and Prof. Dr Voitech Stankevič for the valuable revision and comments on my thesis.

VILNIUS TECH for the opportunity to prepare this dissertation.

The doctoral committee and all of my colleagues from the Department of Physics and Laboratory of Electronic Processes for their insightful comments and suggestions.

FTMC for the fabrication of the samples and the possibility of carrying out experiments.

Prof. Eugene Katz for leading me during my internship at Jacob Blaustein Institute for Desert Research (BGU of Negev).

My family and friends for their support and belief in me.

1

Review of Solar Cell Structures and Hot Carrier Phenomenon

This chapter reviews the history of photovoltaics, the fundamental parameters of solar cells, their classification, and the principles of their operation. Investigations are reviewed regarding suppressing spectral and thermalisation losses via using new structures and materials for solar cells. Various methods are observed for exciting carriers and also processes of dissipation of extra energy. Structures are analysed in which hot carriers were studied. This chapter concludes by the formulated main objective and tasks of the investigation (Ašmontas, Fedorenko et al., 2020; Gradauskas, Ašmontas, Sužiedėlis, Šilėnas, Čerškus et al., 2020b; Gradauskas, Ašmontas, Sužiedėlis, Šilėnas, Vaičikauskas et al., 2020; Gradauskas et al., 2022; Masalskyi, Gradauskas, Ašmontas et al., 2022a; Masalskyi & Gradauskas, 2021a, 2022).

1.1. History of Photovoltaics

The rapidly increasing global energy demand has called for alternative energy sources. Solar energy has received attention as a renewable and environmentally

friendly option. Understanding the advantages, disadvantages, and historical development of solar energy technology is essential for explaining its significance in naming the world's energy needs and environmental challenges.

From the Industrial Revolution to today, global energy consumption has increased exponentially in response to the modern standard in developed countries. Consumption is leading to a constant expansion of global energy demand and production. However, the limited availability of primary exhaustible energy sources such as oil, coal and gas have long-term unfavourable environmental leverage. Solar energy is an environmentally friendly renewable energy source. Using solar energy has advantages and disadvantages.

The advantages include:

- free source;
- long operating time of industrial solar panels is about 25 years;
- ease of use in terms of monitoring;
- functionality – solar cells are convenient for home use.
- The disadvantages are:
- less efficient during night-time than daylight;
- need to accumulate the converted electricity.

The history of photovoltaics started with the discovery of the photoelectric effect in 1839 by A.-E. Becquerel. The scientist noticed a photovoltaic (PV) cell-induced photocurrent under illumination (Green, 2015).

In 1873, the English electrical engineer W. Smith carried out experiments and discovered that illumination changed the resistance of selenium. In 1876, W.G. Adams discovered that selenium could generate electricity on its own. This experiment showed that it was possible to generate electricity directly from solid materials without using thermal or mechanical types of energy. In 1883, Ch. Fritts created the first selenium cell. This module became the forerunner of the modern photovoltaic cells (Green, 2015).

In 1887, H.R. Hertz discovered a new property of semiconductors, which he called the photoelectric effect. A.G. Stoletov created the first photocell that was based on this effect. In 1907, A. Einstein developed a theoretical model for the photoelectric effect. In 1912–1916, R.A. Millikan experimentally confirmed Einstein's theory (Green, 2015).

In 1940, R.S. Ohl discovered the *p–n* junction while working with silicon-based samples. In 1949, W.B. Shockley developed a theoretical model of a *p–n* junction, thus creating the basis for the development of modern solar cells (Green, 2015).

The power conversion efficiency of the first photovoltaic cells was only 4%. In 1955, an efficiency of 11% was achieved, and these cells were used as a power

source for telephone amplifiers. In 1958, the USA and the USSR launched satellites into orbit around the Earth with equipment partially powered by solar batteries (Green, 2015).

The first mass-produced photovoltaic panels appeared in 1979 in the USA. Since the oil crisis began, intensive research and development have been carried out to enhance the efficiency, low prices and longer lifetime of PV cells (Green, 2015).

Generating electricity became popular in the mid-2000s, and the power conversion efficiency was increased. It is tough to find any industry field that does not use solar panels (Green, 2005).

1.2. Solar Spectrum for the Solar Cells

The solar radiation spectrum is an important issue for using solar energy effectively. By studying its intensity, spectral composition, and effects of varying sunlight angles, researchers can optimise solar energy technologies and improve the performance of photovoltaic devices. This section studies characteristics of the solar spectrum, with a particular focus on the term Air Mass (AM) and its role in solar energy research.

Fig. 1.1 shows standards of the solar spectrum which are used for PV device investigations.

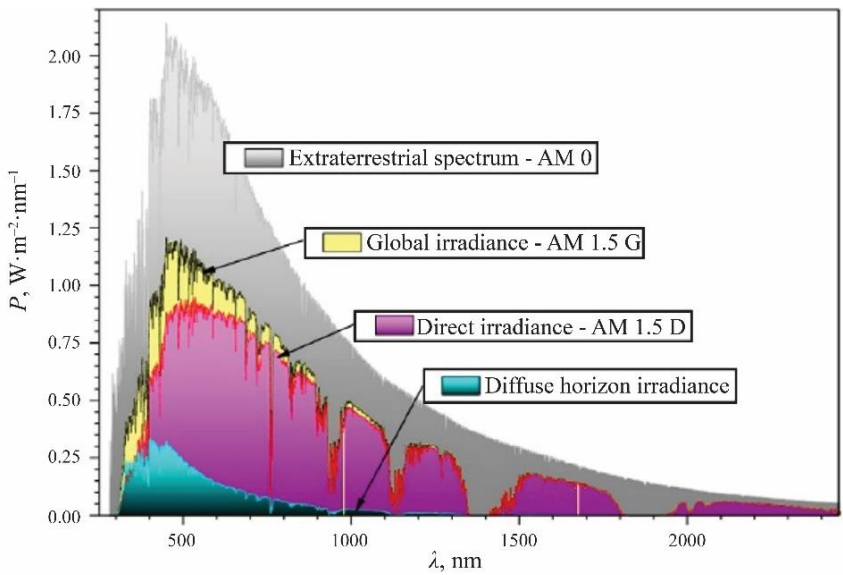

Fig.1.1. Spectra of the solar standards (Rodziewicz et al., 2021)

The spectrum of solar radiation is the portion of the electromagnetic radiation emitted by the Sun. Solar light, on its way from the Sun to the surface of the Earth, loses part of its power (Myers & Emery, 2002; Rodziewicz et al., 2021).

First, the solar spectrum is characterised by power falling on the surface of a certain area, and it depends on the regions of the Earth.

Another important parameter of the solar spectrum is the so-called spectral composition of sunlight (Rodziewicz et al., 2021).

The Air Mass concept is introduced to characterise it, for example:

- The standard AM 0 (Fig. 1.1) corresponds to the spectrum of sunlight above the atmosphere of the Earth (Rodziewicz et al., 2021);
- The standard AM 1 corresponds to the radiation on the Earth's surface when the Sun is strictly above the observation object (the sun angle between the surface of the object and falling sunlight is 90o), i.e., the sunlight passes through one atmosphere;
- The standard AM 1.5 corresponds to the radiation on the surface of the Earth when the sun angle is 48.2o (Myers & Emery, 2002; Rodziewicz et al., 2021).

Since it is impossible to maintain a permanent sun angle of 90 because of the Earth and Sun cycle, the standard AM 1.5 is used to test solar cells.

1.3. Fundamental Characteristics of a Solar Cell

Understanding a solar cell's fundamental characteristics is essential for evaluating and optimising its operation and comparing different solar cell technologies.

The basic parameters of a solar cell are as follows:

- Current–voltage (I–V) characteristic;
- Short circuit current;
- Open circuit voltage;
- Fill Factor;
- Efficiency.

The current–voltage characteristic of a solar cell provides valuable insights into its behaviour and performance. The *I–V* characteristic is the dependence of current flowing through a solar cell upon voltage across the cell. For a single junction solar cell, the *I–V* characteristic is described by the equation (Sah et al., 1957):

$$I = I_0\left(e^{\frac{qV}{kT}} - 1\right) - I_{\mathrm{LG}}. \tag{1.1}$$

Here, I is the current flowing through the cell, I_0 is the saturation current or reverse current, q is the electron charge, k is the Boltzmann's constant, T is the

absolute temperature, I_{LG} is the induced photocurrent, and V is the voltage across the cell.

The I–V curve of a solar cell is depicted in Fig. 1.2.

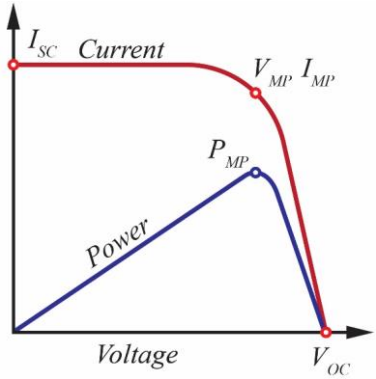

Fig. 1.2. Typical current–voltage (red) and power–voltage (blue) curves of a solar cell. I_{sc} is the short circuit current, V_{oc} is the open circuit voltage, V_{MP} is the voltage for maximum power, I_{MP} is the current for maximum power, P_{MP} is the maximum power (created by the author)

The short circuit current of SC is the current flowing through the solar cell when the voltage across the cell is equal to zero (the cell is short-circuited). The short circuit current is the largest in a solar cell. It is described by the formula (Sze & Ng, 2006):

$$I_{\mathrm{SC}} = qG\left(L_{\mathrm{n}} + L_{\mathrm{p}}\right). \tag{1.2}$$

Here, G is the generation rate, L_{n} and L_{p} are the diffusion lengths of electrons and holes, respectively.

The open-circuit voltage is the maximum voltage that can be generated by a solar cell, and it can be described (Sze & Ng, 2006):

$$V_{OC} = \frac{kT}{q} ln\left(\frac{I_{\mathrm{SC}}}{I_0} + 1\right). \tag{1.3}$$

The fill factor is the parameter of the I–V curve that is equal to the maximum power of a solar cell over the short-circuit current and open-circuit voltage:

$$FF = \frac{P_{\mathrm{MP}}}{I_{\mathrm{SC}} V_{\mathrm{OC}}}. \tag{1.4}$$

If the shunt and series resistances in a solar cell are neglected (ideal case), then the fill factor can be described as (Green, 1982):

$$FF = \frac{V_{\mathrm{OC}} - \ln\left(V_{\mathrm{OC}} - 0.72\right)}{1 + V_{\mathrm{OC}}}. \tag{1.5}$$

Here, 0.72 is the approximation factor for the precision of two significant figures that can be used for any semiconductor single-junction solar cell.

The efficiency is defined as the ratio of the electrical power generated by the solar cell to the power of the incident solar radiation:

$$\eta = \frac{P_{\mathrm{gen}}}{P_{\mathrm{in}}} = \frac{V_{\mathrm{OC}} I_{\mathrm{SC}} FF}{P_{\mathrm{in}}}. \tag{1.6}$$

Here, P_{gen} is the generated power by solar cells, and P_{in} is the incident power. The efficiency of SC depends on the spectrum and intensity of the incident solar radiation and temperature.

1.4. Limitations and Basic Losses of Solar Cells

Looking into the loss mechanisms in an ideal solar cell is a necessary step towards increasing its efficiency. Estimating the intrinsic losses and exploring strategies to avoid them allow for enhancing the efficiency of solar cells. By reducing losses and pushing the efficiency limits, solar cell technology would make significant contributions to meet the increasing global demand for clean and sustainable energy.

The Shockley–Queisser limit determines the maximum efficiency of 33% for an ideal single-junction solar cell (Shockley & Queisser, 1961). This limit identifies that semiconductors having a band gap between 1 eV and 1.5 eV have the greatest potential to form an efficient single junction cell (Rühle, 2016).

New photovoltaic materials are being researched constantly. Si and GaAs are the most widespread materials for solar cell production, and they have already reached an efficiency of about 24% and 29%, respectively (Fig. 1.3). Si is used because it is an abundant material that has a well-developed fabrication technology, high enough efficiency, low cost, and long lifetime of the cells. GaAs is relatively insensitive to heat, have a long lifetime, and have efficiency even higher than Si. Unfortunately, GaAs is a much more expensive semiconductor (Ehrler et al., 2020).

To achieve higher efficiency, it is necessary to reduce the fundamental intrinsic and extrinsic losses in solar cells. Extrinsic losses include the following types: contact shadowing, series resistance, and parasitic recombination. Generally, the extrinsic losses can be reduced by applying novel techniques of manufacturing, which is why these losses are not accounted for when calculating the theoretical efficiency of a single junction solar cell. On the contrary, intrinsic losses are a consequence of physical processes in the bulk of a semiconductor,

and they are hardly avoidable. The composition of intrinsic losses is depicted in Fig. 1.4.

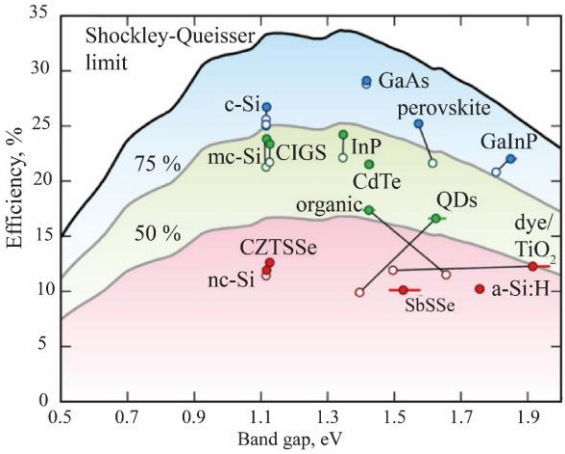

Fig. 1.3. Record the efficiency of the solar cell made of different materials against their band gap in comparison to the Shockley–Queisser limit (top solid line) (Ehrler et al., 2020)

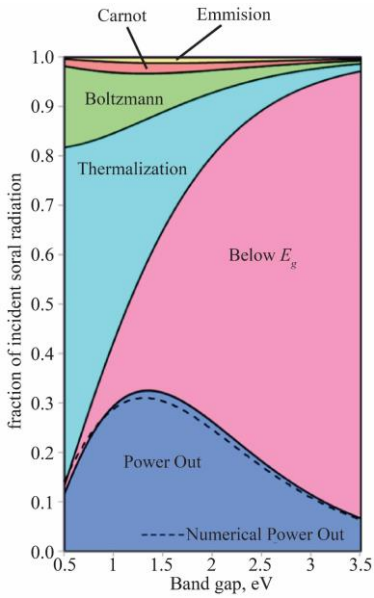

Fig. 1.4. Dependence of intrinsic losses on the width of the band gap (Hirst & Ekins-Daukes, 2011)

The intrinsic losses consist of (Araújo & Martí, 1994; Conibeer, 2007; De Vos et al., 1993; Hirst & Ekins-Daukes, 2011; Markvart, 2007):

1. Below band gap (E_g) loss. This loss can be described as the photons having energy lower than the width of the band gap are not absorbed.
2. Thermalisation loss. It manifests itself due to mismatching of energies of excited carriers and the width of the band gap. Carriers with extra energy thermalise through the lattice heating process.
3. Emission losses. Absorbers are also emitters; re-emission reduces efficiency.
4. Carnot loss. The conversion of thermal energy into electrical work requires some energy to be sacrificed to the cold reservoir.
5. Boltzmann loss. It is caused by the inequality of absorption and emission angles.

It is worth noting that the sum of thermalisation and below-band gap losses takes about 80% of all intrinsic losses and has to be reduced first of all (Hirst & Ekins-Daukes, 2011).

Understanding loss mechanisms in an ideal solar cell is the mandatory step to increase its efficiency. Estimation of the intrinsic losses and finding possibilities to overcome them opens ways to enhance the efficiency of the SCs (Henry, 2008).

1.5. Classification of the Solar Cells

Different generations and types of solar cells help to tailor solar cell technology for specific applications and optimised efficiency. Continued research and development in solar cell technology promises further advancements and increases the adoption of solar energy as a sustainable power source.

Various types of solar cells are suitable for different purposes and tasks. The difference between the types of SCs is usually defined by used structures, materials, and solar spectrum wave range (Mohammad Bagher et al., 2015). These features are also referred to as the first, second and third-generation solar cells. This classification has been used for the past three decades and is the basic classification for solar cells (Ananthakumar et al., 2019).

The *First Generation* of solar cells includes single junction solar cells traditionally made of Si. This generation of solar cells is the oldest and the most commonly used technology type and includes the following constructions (Akinoglu et al., 2021):

1. The monocrystalline solar cell is a type of SC where Si is the purest since it contains little undesirable impurities. High purity of Si is a requirement

for high efficiency because of the diffusion length that reaches 100 μm. The efficiency can achieve 24.2%, and the price per unit capacity of a cell is comparably high due to the more expensive fabrication process and the use of highly purified silicon (Akinoglu et al., 2021).

2. Polycrystalline solar cells are cheaper because the cost of the starting material (multicrystalline plates) is lower than that of the monocrystalline Si, but their efficiency is around 15% (Akinoglu et al., 2021).

The *Second Generation* is represented by many types of thin-film solar cells made of amorphous silicon, gallium arsenide cadmium telluride or copper indium gallium selenide. These types of SCs are easy to develop, cheap because they require less material, are flexible, which opens the way for alternative applications, and are less sensitive to high temperatures. The main problem is the large size of solar cells, which makes them narrowly targeted. Moreover, these have a shorter lifetime than the first-generation SCs, and their efficiency is also less (Mohammad Bagher et al., 2015).

The *Third Generation* includes SC structures that are still under development. The cells are made of various new materials and structures, such as nanotubes, organic layers, and semiconductor wires/wells/dots. The third generation was founded with the main purpose of overcoming the Shockley–Queisser limit and making solar cells more commercially available (Conibeer, 2007). This generation consists of the following spectrum processing groups (Akinoglu et al., 2021):

1. Spectral conversion. The principle is based on modifying the spectrum absorbed by a solar cell. This process is used for better absorption of sunlight and allows to boost the efficiency of SCs significantly. Spectral conversion of SCs represented by up- and down-conversion solar cells. Up-conversion SC converts two or more low-energy photons, which penetrate the cell, into one high-energy photon. Converted photon has energy slightly higher or equal to the band gap of a solar cell is absorbed. Down-conversion SC transforms one high-energy photon, which can be absorbed inefficiently due to thermalisation losses, into two or more lower-energy photons. All these converted photons have sufficient energy to be absorbed by the cell. (Akinoglu et al., 2021; van Sark et al., 2012).
2. Spectral splitting. This principle includes multi-junction solar cells. The idea is based on the fact that each PV material selectively absorbs the solar spectrum depending on its band gap. Thus, the use of several subcells made of different materials simultaneously in a single solar cell results in an efficiency increase. The efficiency record of 39.2% was achieved in a six-junction solar cell under one sun illumination and 47.1% under concentrated light of 143 suns (Geisz et al., 2020).

3. To effectively harvest the excess carrier energy, the hot carrier solar cell structure was proposed. This structure has energy-selective contacts that help to avoid thermalisation loss (mismatching between the width of the band gap and photon energy). This way, the heated free carrier goes to energy-selective contact and contributes to the formation of the output signal of the solar cell. The absorbers with the longest hot carrier relaxation time should be chosen to harvest hot carriers' energy before their thermalisation (Akinoglu et al., 2021).

1.5.1. Single-junction Solar Cells

A single junction solar cell is a device that harvests photon energy from the Sun and transforms it into electrical current. The *p–n* junction is the basic operating element of a semiconductor solar cell (Fig. 1.5).

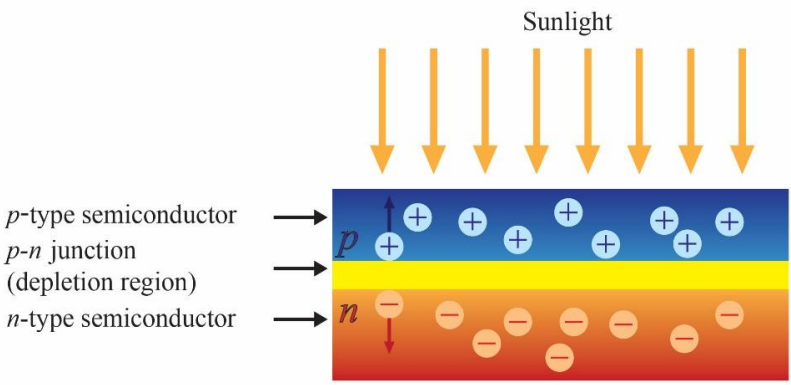

Fig. 1.5. Schematic structure of a single junction solar cell (created by the author)

According to the classical Shockley–Queisser theory, when a single junction solar cell is illuminated, two light absorption mechanisms can be possible (Shockley & Queisser, 1961):

1. If a photon has energy lower than the band gap width of a semiconductor, the cell does not absorb this photon.
2. If a photon has energy equal to or higher than the semiconductor band gap, the cell absorbs this photon.

The absorbed energy lets electrons move into the conduction band, leaving a hole in the valence band. The photocarriers are separated by the electric field of the *p–n* junction. Thus, the current through the *p–n* junction is generated due to the drift of the carriers. Holes charge the *p*-region positively, and electrons charge

the *n*-region negatively. Extra photon energy (if any) exceeding the forbidden energy gap goes to the heating of the semiconductor lattice (Shockley & Queisser, 1961).

1.5.2. Thin film silicon Solar Cells

The principle of operation of thin film solar cells is the same as in the single-junction SCs since their structure includes a *p–i–n* junction. In the manufacturing process of a solar cell, the *p*- and *n*-layers have a thickness of 20–50 nm, and the region *i* has a thickness of 200–300 nm. In the illuminated solar cell, free electron–hole pairs are mainly formed in the *i* layer, and under an internal electric field, they are separated and reach the electrodes (Rajagopal, 2008).

The experimental efficiency of thin-film solar cells made of amorphous silicon was 14% in 2021 (Kang, 2021), while a theoretically possible maximum efficiency is 15% (Lee & Ebong, 2017).

The thin-film SCs have the following advantages:

- the flexibility of the cell;
- less need of material (than the first generation of the solar cells) during the manufacturing;
- low price;
- the low mass of a cell;
- low sensitivity to overheating;

and the following disadvantages:

- efficiency is up to 15%;
- lifetime is 10–20 years.

1.5.3. Perovskite Solar Cells

A perovskite solar cell is representative of the third-generation SCs, showing rapid progress in their efficiency growth (Guo et al., 2017; Yin et al., 2019).

Organic–inorganic lead halide perovskite is an ideal material for PV devices, with efficiency reaching 25.8% under one sun illumination (Min et al., 2021). A perovskite solar cell is a multi-layered device (Fig. 1.6). Perovskite solar cell consists of the absorber perovskite layer and wide band gap layers of carrier transport. The hole transport layer acts as the p^+ layer, and the electron transport layer acts as the n^+ layer.

The photons are absorbed in the perovskite layer, where they generate electron–hole pairs. The pairs are separated via an internal electric field, and the electrons move to the electron transport layer, and the holes move to the hole transport layer (Zekry et al., 2019).

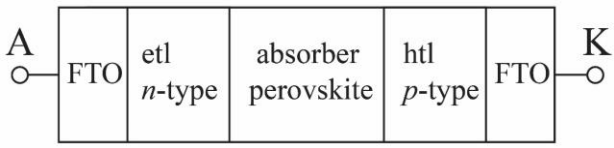

Fig. 1.6. Schematic model of a perovskite solar cell, etl is the electron transport layer, htl is the hole transport layer, and FTO is the layer made of fluorine-doped tin oxide (Zekry et al., 2019)

The main disadvantages of perovskite SCs are instability of the absorber, short lifetime and presence of toxic compounds such as PbI in the composition (Schnier et al., 2017).

1.5.4. Multi-junction Solar Cells

The multi-layered structure of solar cells allows for avoiding inefficient absorption of the solar spectrum or, in other words, helps to reduce the below band gap and thermalisation losses in a solar cell. Thus, multi-junction solar cells work efficiently with a much larger portion of the solar spectrum, and they reach higher efficiency than a single-junction solar cell (Liu et al., 2020).

The absorption mechanism of a multi-junction solar cell is depicted in Fig. 1.7. Generally, the structure consists of several single-junction solar subcells with serial connections between each other (Liu et al., 2020).

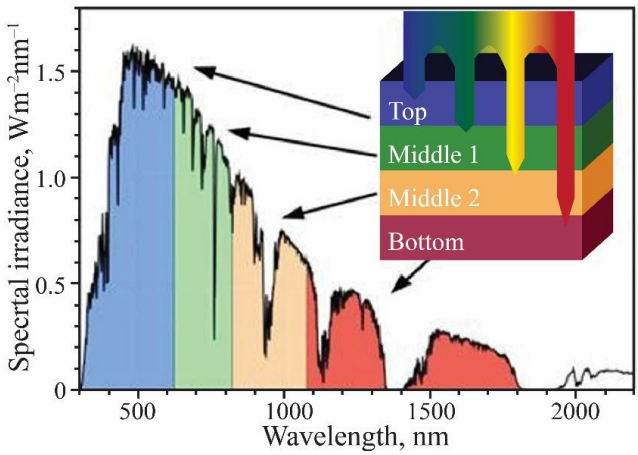

Fig. 1.7. Absorption mechanism of a multi-junction solar cell (Ikeri et al., 2019)

The subcells are connected to tailor the widths of the subcell's band gap. The first subcell has the widest band gap and connects to the next subcell via the recombination layer. This layer provides an electrical connection between the subcells (Liu et al., 2020).

The subcell connection ensures the following absorption model (Fig. 1.7) (Ikeri et al., 2019):

- Absorption in the "Bottom" subcell. A photon having energy equal to or slightly higher than the band gap of the "Bottom" subcell but less than the width of the band gap of the "Middle 2" subcell. Photon goes to the last subcell ("Bottom") and generates an electron–hole pair in it. Moreover, a small excess energy (if any) goes to the thermalisation.
- Absorption in the "Middle 1" subcell. A photon with energy equal to or slightly higher than the width of the band gap "Middle 1" but less than the width of the band gap of the "Top" subcell. Photon passes through the "Top" subcell to the "Middle 1" one and generates an electron–hole pair in it.
- Absorption in the "Top" subcell. The photon with energy that is higher or equal to the band gap of the "Top" subcell generates an electron–hole pair in it.

Theoretically, an infinite number of subcells would have limited efficiency, almost but not 100%, due to the presence of radiative recombination (Yamaguchi et al., 2006). Three-junction SC can reach an efficiency of 36% under 200 suns (Polman & Atwater, 2012), and six-junction SC achieved 39.2% efficiency under one sun (Geisz et al., 2020).

Industrial prototypes of multi-junction solar cells are very expensive in comparison to the others; their maintenance is complicated, and their durability is very short.

1.5.5. Perovskite tandem Solar Cells

A perovskite tandem solar cell is a variation of the multi-junction solar cell design, and its structure consists of only two subcells. The first subcell is made of perovskite due to the variable width of the band gap, and the second subcell is usually made of Si because of its durability. The configuration, particularly of these materials, is optional, but it provides low cost and material band gap matching. Perovskite tandem solar cells can be a two-terminal or four-terminal structure, as depicted in Fig. 1.8 (Minnaert & Veelaert, 2012).

In the two-terminal structure, the subcells are connected in series (Fig. 1.8a), which requires current matching. The output current of the solar cell is equal to the smaller current of a subcell (Minnaert & Veelaert, 2012).

The four-terminal structure has no current limit because it consists of two independent solar cells (Fig. 1.8b). The main disadvantage is that three out of four contacts must be optically transparent and highly electrically conductive. Since no perfectly transparent contacts exist, a part of the light is absorbed by the contacts, reducing the efficiency. Also, the insulating layer between the subcells creates additional losses (Minnaert & Veelaert, 2012).

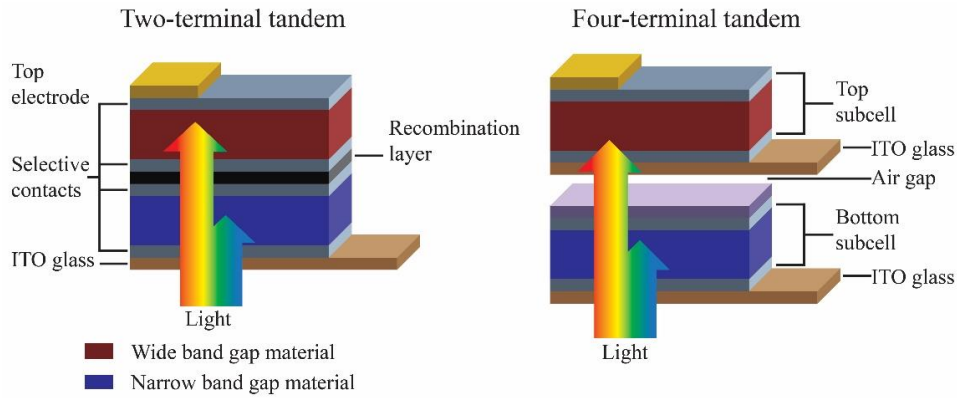

(a) (b)

Fig. 1.8. Structures of two-terminal (a) and four-terminal (b) tandems. ITO is the indium tin oxide; wide- and narrow-band gap absorbers are presented in blue and red, respectively (Minnaert & Veelaert, 2012)

The group of scientists from Helmholtz-Zentrum Berlin has achieved 32.5% efficiency in tandem solar cells consisting of a silicon bottom cell and a perovskite top cell. While the theoretical efficiency of ideal two- and four-terminal structures is about 45% (Dupré et al., 2018). To achieve maximum efficiency in the tandem structure, perfect matching is required between the widths of band gaps of the subcells. The main disadvantage of perovskite tandem solar cells is the instability of the perovskite layer (2 years) (Dupré et al., 2018).

1.5.6. Quantum well Solar Cells

Quantum well layers are considered a way of helping to increase the efficiency of solar cells, and it is a promising candidate to exceed the Shockley–Queisser limit (Akinoglu et al., 2021). The energy band diagram of a quantum well solar cell (Barnham & Duggan, 1998), depicted in Fig. 1.9, generally consists of a quantum well region incorporated into the intrinsic region located between the hole and electron transport layers.

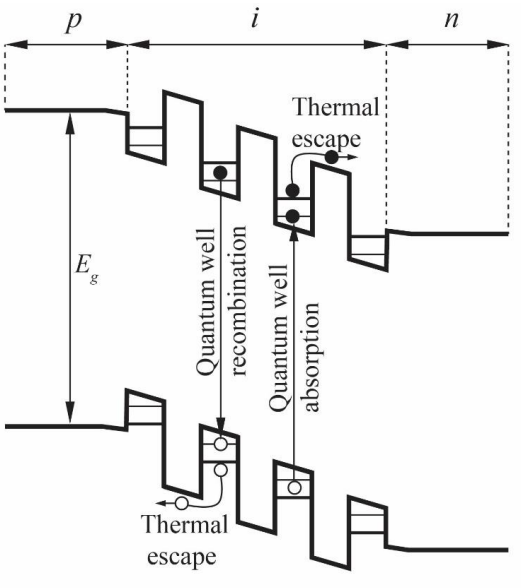

Fig. 1.9. Energy band diagram of the quantum well solar cell (Adams et al., 2010)

The absorbed light in a quantum well leads to generating electron–hole pairs in the well. The energy of the photons that can be absorbed depends on the size of the quantum wells. Before electrons and holes contribute to the net photocurrent, the carriers have to overcome the quantum well's barrier. All excited carriers in a quantum well can theoretically contribute to the net photocurrent, and the device can achieve an efficiency of 26% under one sun illumination (Welser et al., 2019).

1.5.7. Hot carrier Solar Cells

Hot carrier solar cell (Ross & Nozik, 1998) is the third generation SC which can theoretically achieve an efficiency of up to 65% under one sun (Chung et al., 2016).

The concept of the hot carrier solar cell is depicted in Fig. 1.10. The cell consists of the absorber and energy-selective contacts. The optically excited carriers are extracted by contacts before the carriers cool down to the band gap edges.

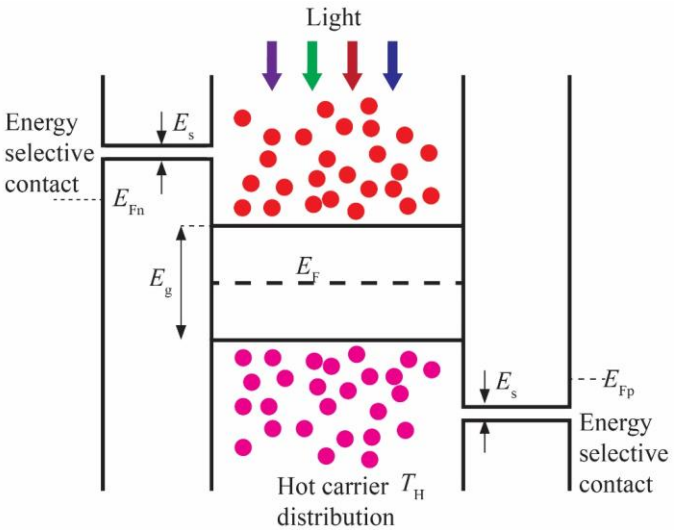

Fig. 1.10. Energy band diagram of a hot carrier solar cell. E_g is the band gap, E_F is the Fermi level, E_{Fn} is the electron Fermi level, E_{Fp} is the hole Fermi level, E_S is the transmission range of energy-selective contact, and T_H is the temperature of the hot carriers (created by the author)

To boost the efficiency, the cooling speed of the excited carriers should be slowed down to allow harvesting of still "hot" carriers (Guo et al., 2017), thus achieving higher photocurrent across the solar cell. Harvesting of energy of hot carriers requires extraction of HCs from the absorber via energy-selective contacts. The contacts transfer carriers only within a very narrow range of energies (Conibeer et al., 2014).

1.6. Hot carriers and hot carrier photoresponse

Hot carriers are excited to free electrons and holes in nonequilibrium high-energy states. Extremely fast cooling time (around 1 ps) of HC and extraction are the main peculiarities of the hot carrier effect (Ahmed et al., 2021).

Different HC excitation methods help to understand the nature of this effect better.

1.6.1. Methods of hot carrier excitation

The very main requirements for the methods of carrier heating and investigation are the exclusion of lattice heating and changes in the concentration of carriers during the experiment (Požela, 1993).

The ways to get extra energy for carrier heating are microwave irradiation, optical irradiation and carrier heating by a strong electric field (Denis & Požela, 1971).

1. Microwave irradiation method. Microwaves are electromagnetic waves having a frequency of 0.3–300 GHz that is equal to 1.24 μeV–1.24 meV photon energy. The microwave photon energy is much lower than the width of the band gap of semiconductors (Zhou et al., 2019).

The method of heating electrons in *n*-type Ge was proposed in 1959. The experiments were carried out under the following conditions (Morgan, 1959):

- constant direct current (DC) field was applied to the sample;
- modulated microwave field was applied along the axis of the sample.

Particularly under these circumstances, the changes in conductivity were detected.

The advantages of the microwave technique are the following (Denis & Požela, 1971):

1) The microwave field is less distorted by inhomogeneities in the sample at frequencies higher or comparable to the inverse dielectric relaxation time.
2) The use of an alternating field of ultrahigh frequency makes it possible to carry out the non-contact heating of the carriers.

Despite the convenience, the method has at least two significant disadvantages (Požela, 1993):

1) First, an alternating electric field leads to a periodic heating of carriers. This circumstance complicated the quantitative interpretation of the “photoelectric effect”.
2) Second, the magnitude of the microwave field in the sample is determined with a noticeable error.

2. Method of DC voltage pulses. In this method, a voltage that heats the carriers is applied to a sample with ohmic contacts. The pulse duration should be chosen so that carriers injected into the bulk drift to a depth much less than the length of the sample. It means that necessary depth should provide conductivity changes, and the field in the sample can be neglected. Also, the duration of the pulse has to be long enough to heat the free carriers but short enough to prevent the lattice heating process. Experimentally, the maintenance of the constant temperature of a sample can be realised by various heat dissipation techniques (Denis & Požela, 1971).

3. Optical irradiation method. This way is the most important for PV devices. The absorption coefficient has a sharp border at the energy equal to the width of E_g of the materials (Fig. 1.11a). Since photons having energy below the band gap cannot produce an electron–hole pair due to lack of energy, these photons have the potential to heat the free carriers in the conductive band to high energy states (Fig. 1.11b, process 4).

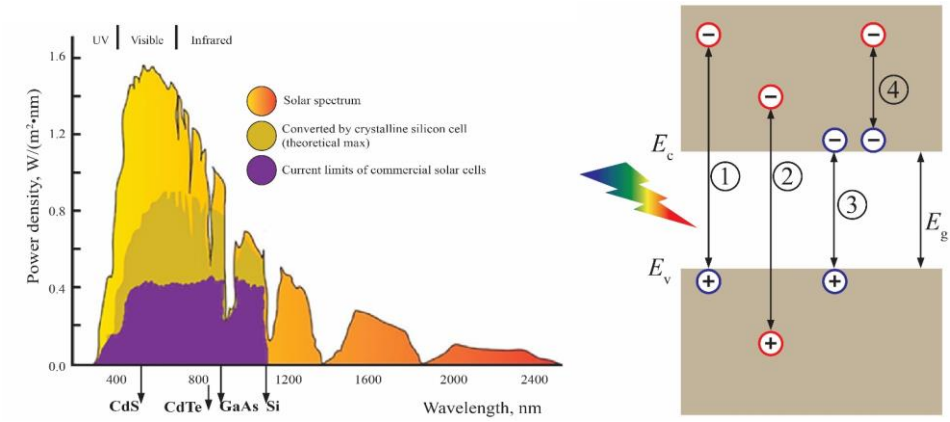

(a) (b)

Fig. 1.11. a) Absorbed solar spectrum by solar cells made of different materials (Akinoglu et al., 2021) b) Schematic model of hot carriers' excitation process. 1 is the generation of hot electron–hole pair, 2 is the generation of hot electron–hot hole pair, 3 – is the generation of electron–hole pair, and 4 – is the free carrier heating process (created by the author)

All other processes in Fig. 1.11 are related to the photons having energy higher or equal to the band gap. During the process of photoexcitation, the photons having energy equal (Fig. 1.11b, 3) or higher (Fig. 1.11b, 1 and 2) than the band gap transmit their energy to the carriers in the valence band and excite them to the high energy states in the conduction band (Ahmed et al., 2021).

1.6.2. Process of hot carrier energy dissipation

Dissipation of hot carrier energy is the multi-stage mechanism through carrier–carrier and carrier–phonon scattering processes (Zhang et al., 2021).

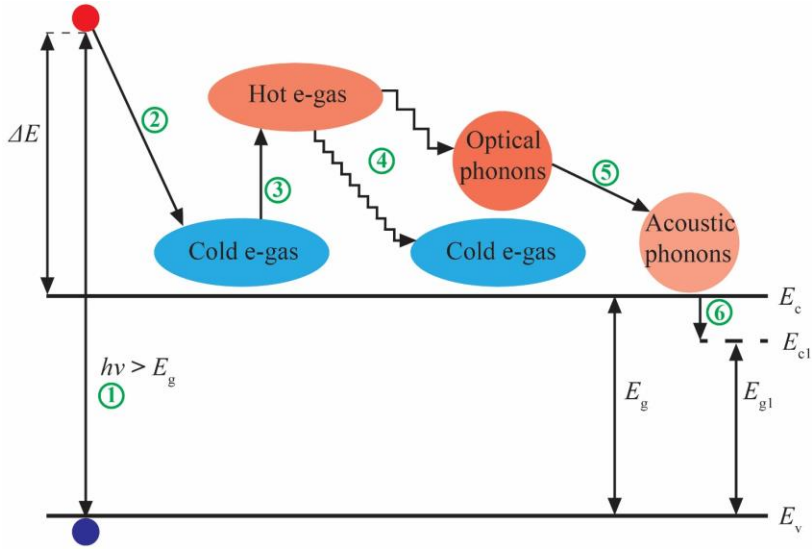

Fig. 1.12. Schematic process of hot carrier energy dissipation. E_g, E_{g1} are the widths of the band gap before and after the energy dissipation process, respectively; E_c, E_{c1} are the position of the bottom edge of the conduction band before and after the energy dissipation process, respectively; E_v is the valence band edge, $h\nu$ is the photon energy, ΔE is the excess carrier kinetic energy, and e-gas is the electron gas (created by the author)

Generally, hot carrier energy dissipation consists of the following stages (Fig. 1.12, green numbers) (Conibeer et al., 2014; Zhang et al., 2021):

1. Electron–hole pair generation from the photon having energy higher than the band gap of the material.
2. Elastic scattering between the excited carriers and cold electron gas (e-gas).
3. The scattering ceases when the e-gas reaches a higher temperature and it obeys the Fermi–Dirac distribution. Usually, stages 2 and 3 have a duration of 10–100 fs.
4. Cooling down of the e-gas to the edge of the conduction band while simultaneously emitting discrete portions of energy as optical photons (the term “optical photon” means non-phasing oscillations of the atoms in the lattice). The stage 4 lasts for 0.01–1 ps.
5. Optical phonon decay into acoustic phonons (the term “acoustic photon” means coherent oscillations of the atoms from the equilibrium position). This process results in the heating of the lattice.
6. The lattice heating process modifies the band structure of the material (usually changes the width of the band gap).

In general, the HC energy dissipation process has a duration of about 1 ps (Conibeer et al., 2014; Zhang et al., 2021). To use the hot carrier effect, the fast relaxation time of carrier energy should be extended, or the harvesting of energy from still "hot" carriers should be provided as fast as possible.

1.6.3. Hot carrier photo signal across germanium *p–n* junction

The classical photo effect manifests itself in regular photosensitive devices, such as solar cells, only when the incident light photon energy is higher than the band gap of the material (Shockley & Queisser, 1961). Later, it was proven (Umeno et al., 1978; Wasiak et al., 2017; Zanatta, 2019) that even light with photon energy lower than the width of the band gap can be absorbed.

The below band gap absorption caused the rise of anomalous hot carrier photovoltage with polarity opposite to the ordinary photovoltaic effect. Instead of the classical electron–hole pair generation, the free carrier excitation in the *n*- and *p*-sides of the *p–n* junction induces voltage (Umeno et al., 1978).

HC photovoltage experimentally was discovered across Ge *p–n* junctions (Fig. 1.13).

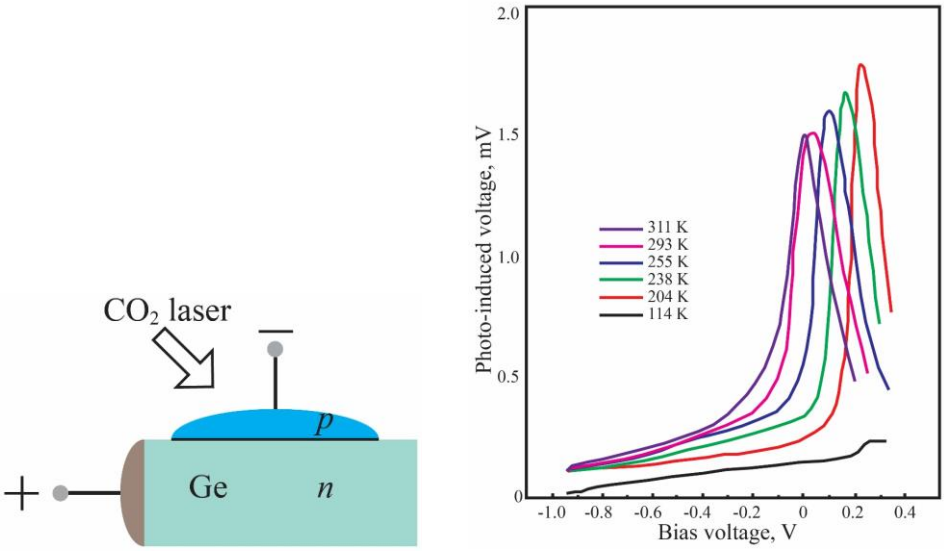

a) b)

Fig. 1.13. a) Ge *p–n* junction under illumination with CO_2 laser radiation; b) dependence of induced hot carrier photovoltage on bias voltage at different temperatures (Umeno et al., 1978)

The sample was illuminated with a CO_2 laser having the following parameters: 10.6 μm wavelength (with photon energy $h\nu = 0.117$ eV) and peak power 0.5 kW (Fig. 1.13a). The polarity of induced hot carrier photovoltage was opposite to the classical photovoltage. The experimental dependences of photovoltage on bias voltage are depicted in Fig. 1.13b. In the given experiment, the interband absorption was impossible since the band gap energy of 0.66 eV was much higher than the photon energy. In this case, the induced photovoltage appeared due to the intraband absorption (Umeno et al., 1978).

In the illuminated *p–n* junction, the major carriers on both *p*- and *n*- regions were excited optically, they became hot carriers and diffused over the potential barrier. The excitation process of the carriers and formation of photovoltage is depicted in Fig. 1.14 (Umeno et al., 1978).

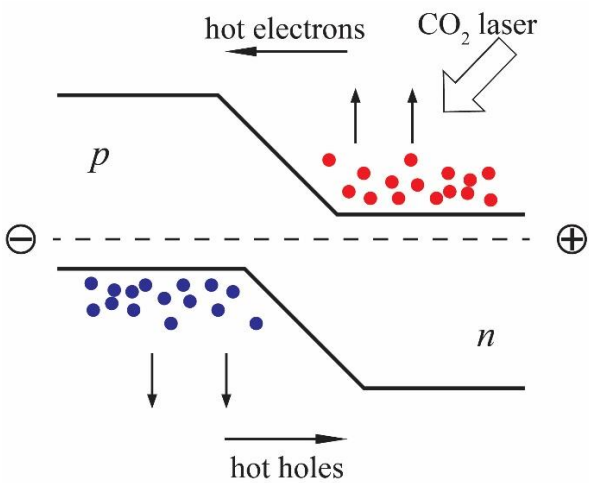

Fig. 1.14. Schematic representation of free carrier heating and formation of photovoltage across *p–n* junction (Umeno et al., 1978)

1.6.4. Photocurrent of hot carrier across gallium arsenide *p–n* junction

The experimental setup that revealed the presence of hot carrier phenomena in GaAs *p–n* junctions is depicted in Fig. 1.15.

The GaAs samples were illuminated with CO_2 laser pulses with a wavelength of 10.6 μm, pulse duration of 200 ns, repetition rate of 30 Hz, and maximum power density of 10 MW/cm^2. The diameter of the contact was around 0.5 mm (Ašmontas et al., 2001). Fig. 1.16 shows the dependence of photocurrent across the *p–n* junction on the applied bias voltage.

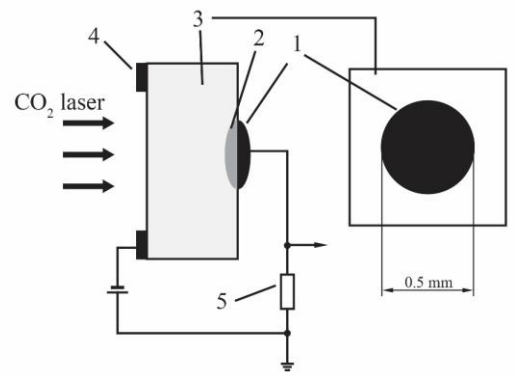

Fig.1.15. Schematic circuit of measurements: 1 – metal back contact, 2 – doped region, 3 – substrate, 4 – front ohmic contact, 5 – load resistance (Ašmontas et al., 1997)

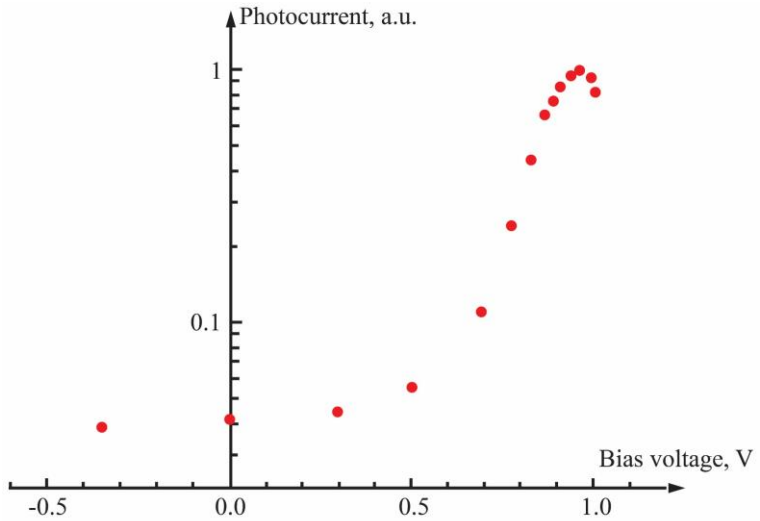

Fig. 1.16. Dependence of photocurrent on bias voltage across GaAs *p–n* junction (Ašmontas et al., 2001)

Fig. 1.16 shows a similar dependence of photoresponse on bias, as depicted in Fig. 1.13b. The fast growth of the photocurrent was observed when the forward bias "opened" the junction. When the reverse bias was applied, the photocurrent was small because of the recharging of the *p–n* junction under pulsed laser light. The small magnitude of photocurrent at the reverse bias proved insignificant changes of carrier concentration in GaAs *p–n* junction illuminated with CO_2 laser (Ašmontas et al., 2001).

Also, the increase of photocurrent in the forward bias region was caused by the decreasing height of the potential barrier. Thus, optically heated carriers could easily diffuse across the potential barrier and contribute to the photoresponse of the *p–n* junction by inducing photocurrent with polarity opposite to the standard electron–hole pair excitation (Ašmontas et al., 2001).

In a strongly asymmetrical *p–n* junction, when the *p*-region is doped much heavier than the *n*-region, the contribution of hot electron photocurrent is weak. In this case, the HC photocurrent density across the *p–n* junction can be described as (Ašmontas, 1984):

$$J_{\mathrm{ph}} = J_0 \left\{ exp\left[\frac{qU_{\mathrm{b}}}{kT_{\mathrm{p}}} + \frac{qV_{\mathrm{bi}}}{kT_0}\left(1 + \frac{T_0}{T_{\mathrm{p}}}\right)\right] - 1 \right\} - J_{\mathrm{ps0}} \left\{ exp\left[\frac{qV_{\mathrm{bi}}}{kT_{\mathrm{p}}}\right] - 1 \right\}. \quad (1.7)$$

Here, U_{b} is the applied bias voltage, $J_{\mathrm{ps0}} = eD_{\mathrm{p}}p_{\mathrm{n}}/L_{\mathrm{p}}$ is the saturation current density in the dark, J_0 is the saturation current density under illumination, D_{p} is the diffusion coefficient of holes, L_{p} is the diffusion length of holes, T_0 is the lattice temperature, V_{bi} is the height of the potential barrier, and T_{p} is the temperature of hot holes.

When the *n*-region was doped much heavier, the heated electrons mainly contribute to net photocurrent across the *p–n* junction, and then, the impact of heated holes can be neglected (Ašmontas, 1984).

1.6.5. Hot carrier photo signal across homogeneous gallium arsenide junction

As mentioned above, maximum photocurrent across the junctions can be detected when the potential barrier height is reduced by the applied voltage bias. An inherent feature of homogeneous junctions (lightly and heavily doped regions) is a small potential barrier that makes these junctions useful structures to detect hot carrier photo signals.

When the homogeneous GaAs junctions were illuminated with CO_2 laser light (the same conditions of the experiment as in the previous section), the obtained photoresponse U consisted of two components (Fig. 1.17) (Ašmontas et al., 2001):

$$U = U_{\mathrm{f}} + U_{\mathrm{T}}. \quad (1.8)$$

Here, U_{f} is the fast part of the signal, caused by the heating of free carriers, U_{T} is the slow part of the signal, caused by the lattice heating process. The contribution of these components to the output signal is depicted in Fig. 1.17. The components of the signal were approximated concerning the shape of the laser pulse. The fast component was described (Ašmontas et al., 2001):

$$U_{\mathrm{f}}(t) = k_{\mathrm{f}} I_{\mathrm{p}} \left(\frac{t}{\tau_{\mathrm{p}}}\right)^4 exp\left[-4\left(\frac{t}{\tau_{\mathrm{p}}} - 1\right)\right]. \tag{1.9}$$

Here, where I_{p} is the laser peak intensity, τ_{p} is the laser rise time, and k_{f} is the coefficient that can be found from the experiment.

The slow component U_{T} can be expressed by (Ašmontas et al., 2001):

$$U_T = \frac{24 k_{\mathrm{T}} I_{\mathrm{p}} e^4}{\tau_{\mathrm{T}} \tau_{\mathrm{p}}{}^4 a^5}\left[\left(1 - ta + \frac{(ta)^2}{2} - \frac{(ta)^3}{6} + \frac{(ta)^4}{24}\right) \times exp\left(\frac{4t}{\tau_{\mathrm{p}}}\right) - exp\left(-\frac{4}{\tau_{\mathrm{T}}}\right)\right]. \tag{1.10}$$

Here, $a = \frac{1}{\tau_{\mathrm{T}}} - 4/\tau$, k_{T} is the amplification coefficient, which was found from the experiment, and τ_{T} is the time constant of photoresponse decay.

Fig. 1.17 shows the temporal behaviour of the experimental photoresponse and calculated theoretical components alongside the laser pulse.

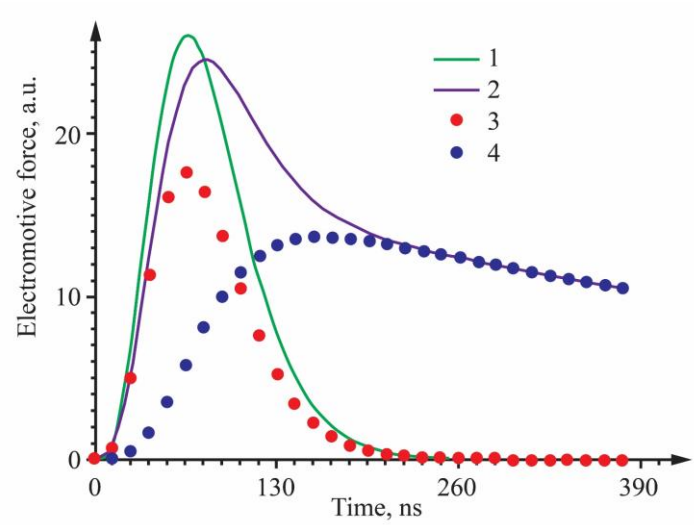

Fig. 1.17. Shapes of the CO_2 laser pulse (1) and photoresponse signal across GaAs n–n^+ junction (2). Theoretically calculated hot carrier (3) and lattice heating (4) components of the photoresponse (Ašmontas et al., 2001)

The results in Fig. 1.17 allowed for approximately distinguishing the contribution of hot carriers and lattice heating components to the net photoresponse signal induced across the junction. Fig. 1.18 shows the linear dependence of photoresponses across n–n^+ and p–p^+ GaAs junctions on laser intensity.

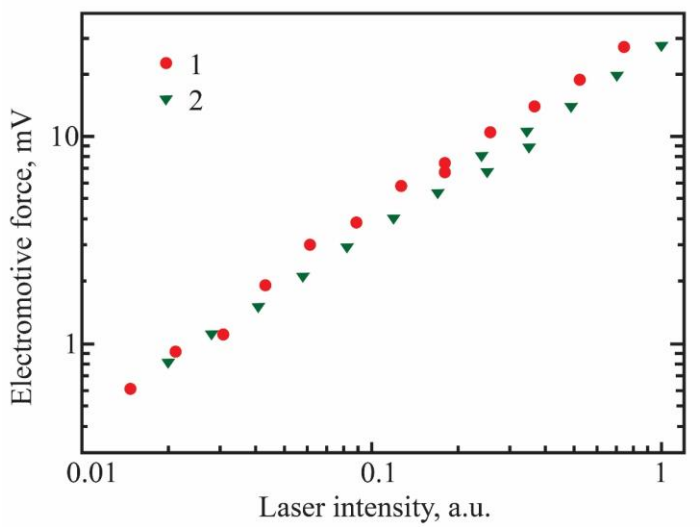

Fig. 1.18. Photoelectromotive force across GaAs homogenous junctions versus laser intensity. (1) n–n^+ and (2) p–p^+ junctions (Ašmontas et al., 2001)

According to the given results, the magnitudes of the photoresponses (Fig. 1.18) were almost similar. It was concluded that the temperature of the heated holes and electrons was almost the same (Ašmontas et al., 2001).

1.6.6. Hot carrier photo signal across mercury cadmium telluride *p–n* junction

Hot carrier signal was also detected in narrow-band materials by intraband-free carrier excitation. Studying peculiarities of HC signal arising may help to look through the unknown features of this effect due to the height of the potential barrier and cryogenic temperature.

$Hg_{0.8}Cd_{0.2}Te$ is a narrow band gap (0.16 eV) semiconductor. The width of the E_g is comparable with the photon energy of the CO_2 laser but only at room temperature. The given material relates to the tellurium-containing semiconductors. In classical semiconductors, such as GaAs and Si, the band gap decreases with increasing temperature, while $Hg_xCd_{1-x}Te$ has inverse band gap dependence on temperature that can be approximated via a formula where the width of the band gap is in eV (Rogalski, 2005):

$$E_g = -0.302 + x(1.93 - 0.81x + 0.832x^2) + 5.35 \times 10^{-4}(1 - 2x)T. \quad (1.13)$$

Here, x is the HgTe mole fraction, and T is the temperature. According to Eq. 1.13, at the temperature of liquid nitrogen (80 K), the height of the band gap was equal to 0.09 eV (Rogalski, 2005). $Hg_{0.8}Cd_{0.2}Te$ *p–n* junction was cooled down to 80 K to simultaneously observe the hot carriers and classical (electron–hole generation) photocurrent in the total current signal (Ašmontas et al., 2003).

Fig. 1.19 shows laser pulse shape and photoresponses across $Hg_{0.8}Cd_{0.2}Te$ at different laser intensities.

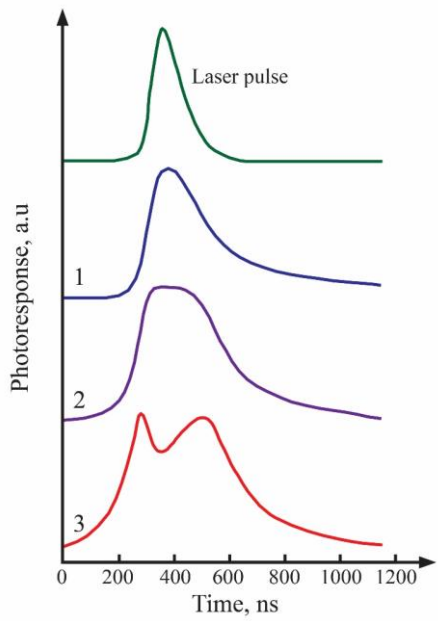

Fig. 1.19. Temporal traces of the laser pulse (dotted line) and photoresponses (1–3) at increasing laser light intensities from low to high, respectively (Ašmontas et al., 2003)

$Hg_{0.8}Cd_{0.2}Te$ photodiodes were prepared on *n*-type single crystal substrates by diffusion of arsenic from the vapour source into the wafer with followed annealing process under Hg-saturation condition ($n \approx 1 \div 6 \times 10^{15}$ cm^{-3} at 80 K). The samples were illuminated with a CO_2 laser that had the following parameters: wavelength 10.6 μm ($h\nu = 0.117$ eV), pulse duration 200 ns, and maximum laser intensity 1 MW/cm^2 (Ašmontas et al., 2003).

Pulse 1 in Fig. 1.19 shows classical photoresponse that was caused by interband absorption. The classical photoresponse becomes saturated due to the limitation of the potential barrier height (Fig. 1.19 pulse 2). A further increase of the

laser intensity (Fig. 1.19 pulse 3) causes the inducing of photosignal having opposite polarity to the classical photocurrent. The negative component appeared due to carrier heating under the strong illumination of the *p–n* junction (Fig. 1.19 pulse 3). The hot carrier signal completely followed the laser pulse shape.

Also, the dependence of the classical and hot carrier photo signals on light intensity (Fig. 1.20) was linear, which is typical for the HC effect and interband single photon absorption (Ašmontas et al., 2003).

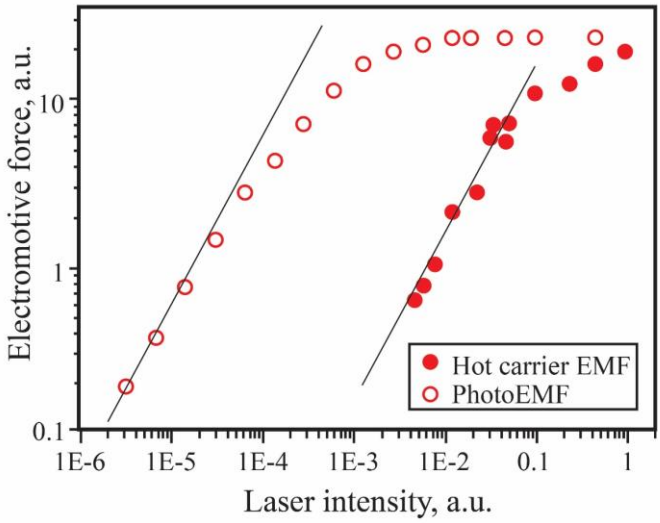

Fig. 1.20. Hot carrier and classical photoresponse dependences on laser intensity (Ašmontas et al., 2003)

1.6.7. Hot carrier photo signal across indium antimonide *p–n* junction

InSb is a narrow-band semiconductor, and its band gap equals 0.23 eV at 80 K temperature. This property makes InSb suitable for investigation of the hot carrier effect under CO_2 laser illumination at low temperatures because the width of the band gap was slightly higher than the laser photon energy (Ašmontas et al., 2003).

The InSb samples were prepared by liquid phase epitaxy deposition of a *p*-type 10 μm-thick layer on an *n*-type wafer with carrier concentrations $p = 10^{16}$ cm^{-3} and $n = 2 \times 10^{14}$ at 80 K temperature, respectively. The samples were illuminated with a CO_2 laser, as described by Ašmontas et al. (2003). Fig. 1.21 shows the photoresponse across the sample at high radiation intensity.

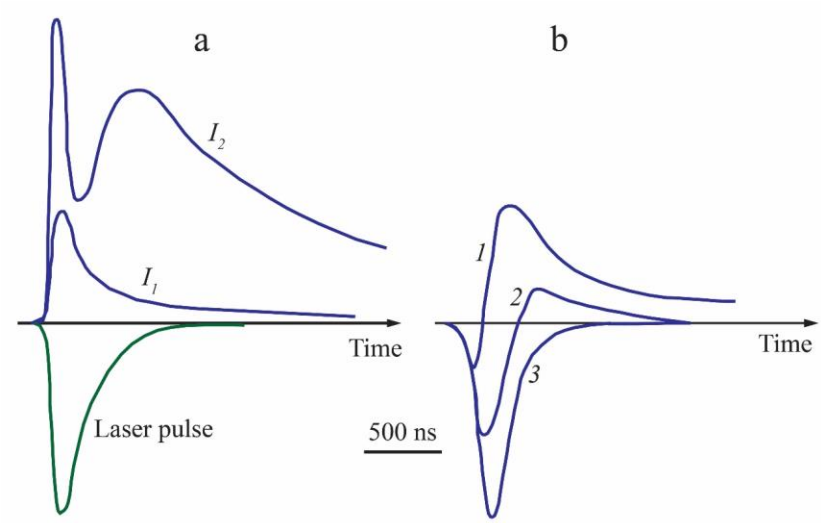

Fig. 1.21. Oscilloscope traces of photoresponse across InSb *p–n* junction: a) at different light intensities, $I_1 \ll I_2$; b) under applied forward bias: 0.167 V (1), 0.2 V (2) and 0.227 V (3) at constant intensity I_1 (Ašmontas et al., 2003)

As Fig. 1.21a shows, the photoresponse induced across the *p–n* junction corresponds to the classical photoresponse (with respect to polarity) caused by electron–hole pair generation via two-photon absorption since the photoresponse had a square dependence on laser light intensity (Ašmontas et al., 2003). The value of classical voltage was limited by the height of the potential barrier. Increasing laser intensity led to the appearance of the hot carrier photoresponse in the output signal (Fig. 1.21a at I_2). The signal with opposite polarity manifested itself due to the heating of the carriers and their diffusion through the potential barrier. The potential barrier was made lower by means of the forward voltage bias (Fig. 1.21b), and the hot carrier signal induced across a *p–n* junction was observed at lower intensity I_1 (Ašmontas et al., 2003).

Also, in InSb the hot carrier photoresponse could be detected simultaneously with the classical (Ašmontas et al., 2003).

1.7. Conclusions of the First Chapter and Formulation of the Dissertation Tasks

The following conclusions based on this chapter can be drawn:

1. The main reason for the low Shockley–Queisser limit is the intrinsic losses in the solar cells since the extrinsic losses are an engineering problem and can be solved by better encapsulation and improved manufacturing techniques. Forasmuch as 80% (Hirst & Ekins-Daukes, 2011) of the intrinsic losses are below the band gap and the thermalisation losses, these two types are particularly referring to the appearance of excess carrier energy.
2. To investigate the hot carrier effect properly, the lattice heating process should be reduced to a minimum.
3. The first- and second-generation solar cells can avoid spectral losses only by modifying their band structure, which was developed in the third-generation solar cells. The most promising types of them are the hot carrier solar cell and the multi-junction solar cell.
4. The hot carrier effect can be applied in the development of long-wavelength radiation detectors. The wide-band semiconductors need intense light and a forward-biased potential barrier to detect radiation with a wavelength much lower than the band gap. The narrow-band semiconductors can be used to detect radiation with a wavelength lower than the band gap, and they require cryogenic temperature to form a potential barrier. Therefore, a useful tool to develop infrared radiation detectors would be a structure with a small potential barrier at 300 K temperature and a wide band gap.

Based on the conclusions, the following tasks can be defined:

1. The hot carrier phenomenon in a single junction solar cell should be investigated to find approaches and conditions that allow for distinguishing and reducing the effect. In this case, the dependence of the HC effect on temperature, bias voltage, and light spectrum should be analysed to define the peculiarities of the effect arising in the solar cells.
2. The way to reduce spectral and thermalisation losses in structures containing *p–n* junction should be searched.
3. The share of spectrum absorbed by a single junction solar cell having the potential to heat the carriers should be calculated.
4. An infrared radiation sensor based on the HC effect should be developed.

2

Fabrication Technology of the Samples and Research Methodology

The methodology of the dissertation consists of two main parts: theoretical modelling (Masalskyi & Gradauskas, 2022) and experimental research (Ašmontas, Fedorenko et al., 2020; Gradauskas, Ašmontas, Sužiedėlis, Šilėnas, Vaičikauskas et al., 2020; Masalskyi, Gradauskas, Ašmontas et al., 2022b; Masalskyi, Gradauskas, Ašmontas, Sužiedėlis, Šilėnas et al., 2021; Masalskyi & Gradauskas, 2021b, 2022). Theoretical methods consist of the separation of photovoltage signal components by the programming environment MatLab, and the modelling of novel PV structures is made by 1D Poisson for PC.

The experimental part is based on the measurement of photoresponse induced by pulsed laser radiation across semiconductor samples and consists of two main parts: (a) peculiarities of photovoltage components' formation across a *p–n* junction (investigation of their dependence on temperature, bias, structure, radiation wavelength, etc.); and (b) photoelectrical investigations of the developed ratchet sensor.

2.1. Fabrication of the samples

This section encompasses the range of methods and techniques used for the specific requirements of different sample types and analytical goals. The sample preparation involves the technologies of growing the samples and analysis of their main parameters.

2.1.1. Gallium arsenide *p–n* junction diodes

The schematic structure of the GaAs diodes' is depicted in Fig. 2.1. The top 5 μm-thick *p*-type layer (hole density 5×10^{17} cm^{-3}) was liquid phase epitaxy-grown on the *n*-type substrate with electron density 3×10^{17} cm^{-3}. Traditional photolithography techniques and thermal evaporation of the Au-Ge-Ni alloy were applied to form the 2.5×2.5 mm^2 sample with ohmic contacts. The contacts were built at the edge of the sample to prevent them from the direct laser beam and thus to avoid photo signal formation in the vicinity of the contacts.

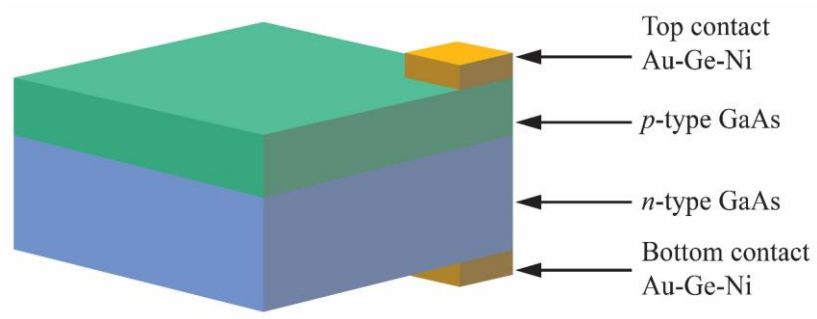

Fig. 2.1. Schematic structure of GaAs diodes (created by the author)

2.1.2. Polycrystalline silicon industrial Solar Cells

The cells (Fig. 2.2) were cut from industrial silicon solar cells (SoliTek, Vilnius, Lithuania). The carrier densities in the emitter and base were $n \approx 10^{20}$ cm^{-3} and $p \approx 10^{16}$ cm^{-3}, respectively. The samples had dimensions 2×2 mm^2.

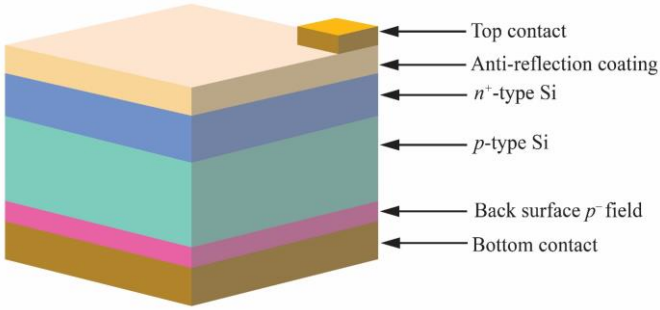

Fig. 2.2. Typical structure of a polycrystalline silicon solar cell (created by the author)

2.1.3. Porous silicon diodes containing porous silicon surface layer

The structure of the diodes is depicted in Fig. 2.3a. The diodes were produced by chemical vapour deposition of an *n*-type epitaxial Si layer (the thickness of 2.5 μm and electron density 6×10^{17} cm^{-3}) on a *p*-type silicon substrate (hole density 6×10^{16} cm^{-3}).

The nanoporous layer was synthesised on an *n*-Si surface using the photo-catalytic electrochemical anodic process in which a 1:4 mixture of ethanol and concentrated HF (49%) were used as an electrolyte. The electrochemical etching of the Si surface was carried out in a transparent electrochemical cell with a Pt gauze electrode (Fig. 2.3b) (Ašmontas, Fedorenko et al., 2020). The fabrication was carried out at V. E. Lashkaryov Institute of Semiconductor Physics, National Academy of Science, Ukraine.

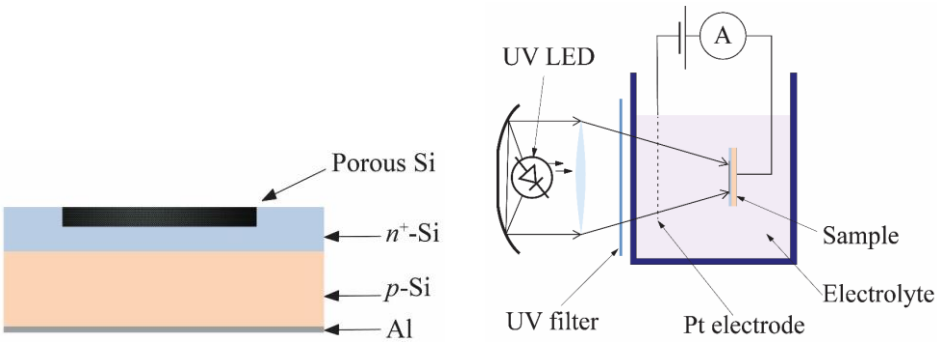

(a) (b)

Fig. 2.3. (a) Schematic structure of Si diode and (b) the system used to form a porous surface layer (Ašmontas, Fedorenko et al., 2020)

During the anodization, the front *n*-surface of the *p–n* junction was illuminated using a high-power light-emitting diode operating at 365 nm wavelength with luminous intensity 8000 W/m^2, the current density was 40 mA/cm^2, and the thickness of the porous Si layer was 1.9 μm.

2.1.4. Ratchet-based sensor

The structure and energy band diagram of the GaAs/$Al_xGa_{1-x}As$ sensor is depicted in Fig. 2.4. The samples were fabricated on a 350 nm-thick *n*-type GaAs wafer (electron density 5×10^{17} cm^{-3}). The two layers of $Al_xGa_{1-x}As$ with AlAs mole fraction "*x*" varying from 0.2 to 0 were liquid phase epitaxy-grown with electron density 10^{18} cm^{-3}. The first $Al_xGa_{1-x}As$ layer was grown up at an initial temperature of 654 ^{o}C, the speed was 1 ^{o}C/min, and the thickness was equal to 1 μm.

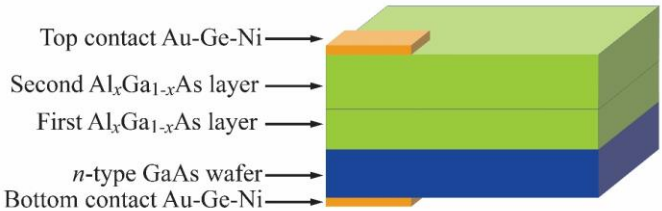

(a)

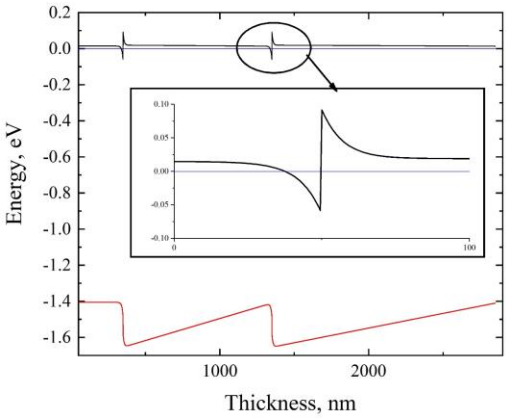

(b)

Fig. 2.4. (a) Schematic structure (not to scale) of the ratchet-based sensor, and (b) its energy band diagram; the black line is the bottom of the conduction band, the blue line is the Fermi level, and the red line is the top of the valence band (created by the author)

The second layer was grown up at the same speed, but the initial temperature was 610 ^{o}C; the thickness was equal to 1.5 μm. The ohmic contacts were formed

by photolithography with the following evaporation and annealing of the Au-Ge-Ni alloy.

2.2. Experimental setup

This section provides an overview of the experimental setup and instrumentation used in the study. The research used a measurement circuit, lasers with specific wavelengths, and temperature-controlled conditions to investigate, characterise, and analyse the hot carrier effect in GaAs *p–n* junction diodes, polycrystalline silicon industrial solar cells, and the ratchet-based sensor.

The schematic measurement circuit used in the research is depicted in Fig. 2.5. The measurements were performed in a photocurrent regime. Two lasers were used to illuminate the samples of GaAs *p–n* junction diodes, the polycrystalline silicon industrial solar cells and the ratchet-based sensor. The load resistor (R = 50 Ohm) was chosen to match the circuit impedance and to obtain appropriate time-dependent characteristics of the photoresponse. To provide the measurements with the bias voltage, a handmade DC voltage source (0–9 V and 0–0.3 A) was used.

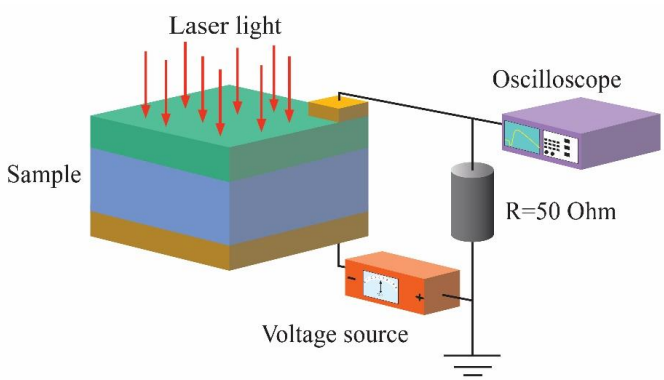

Fig. 2.5. Schematic representation of measurement circuit (created by the author)

The temporal behaviour of the photovoltage and laser pulse shape was recorded by digital storage oscilloscope Agilent Technologies DSO6102A, and the laser pulse shape was registered by high-speed optical signal reference detector 11HSP-FS1 (Standa Ltd., Vilnius, Lithuania).

The experiments were carried out in an 80–300 K temperature range. Low-temperature conditions were maintained using a handmade optical cryostat (Fig. 2.6).

Fig. 2.6. Handmade optical cryostat (created by the author)

Laser light of 1.064 μm wavelength was chosen concerning the width of GaAs forbidden energy gap that is equal to 1.42 eV. Laser photon energy was equal to 1.16 eV and was lower than the band gap. As the source of 1.064 μm wavelength radiation, the neodymium-doped yttrium aluminium garnet laser was used (Fig. 2.7b) with the following parameters: 17–25 ns pulse duration (Fig. 2.7a), repetition rate 50 Hz and maximum pulse intensity 10 MW/cm^2.

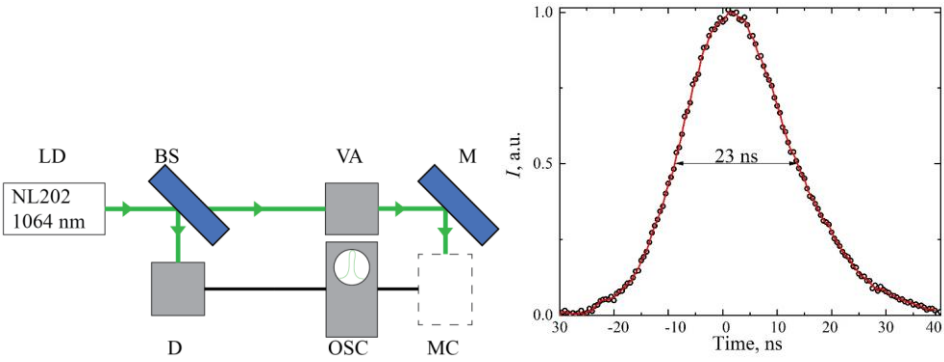

(a) (b)

Fig. 2.7. (a) Neodymium-doped yttrium aluminium garnet oscillator and amplifier at 1.064 μm wavelength. (b) Temporal trace of the 1.064 μm laser pulse. LD – laser diode (NL2002-Nd:YAG), BS – beam splitter plate, VA – variable attenuator for laser pulse, M – high reflectance mirror, D – high-speed optical signal reference detector 11HSP-FS1 (Standa Ltd., Vilnius, Lithuania), OSC – digital storage oscilloscope Agilent Technologies DSO6102A, MC – measurement circuit (created by the author)

The laser power was varied by optical filters having different transmission coefficient values at 1.064 μm wavelength. The average power of the laser radiation was measured via an optical power meter (Thorlabs Inc., New Jersey, USA), and later, pulse power was calculated with respect to the repetition rate and pulse duration.

Another laser of 1.342 μm wavelength (photon energy 0.92 eV) was chosen with respect to the polycrystalline silicon band gap, which is equal to about 1.1 eV. The wavelength was chosen to avoid single-photon excitation of electron–hole pairs. The source of laser light was the neodymium-doped yttrium orthovanadate diode (Fig. 2.8b) with the following parameters: 1.342 μm wavelength, pulse duration 1.7 ns (Fig. 2.8a), and the range of light intensity 0.06 kW/cm^2–0.4 MW/cm^2. The light intensity was varied by adjusting the laser pump power.

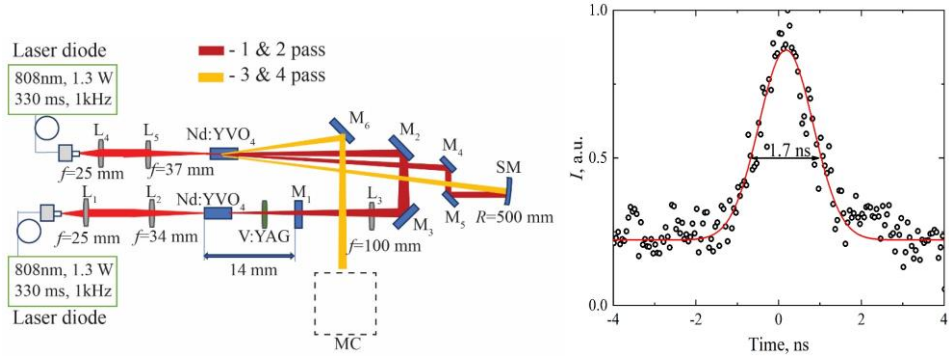

(a) (b)

Fig. 2.8. (a) 1.4-pass neodymium-doped yttrium orthovanadate Q-switched oscillator and amplifier. (b) Temporal trace of the 1.342 μm wavelength laser pulse. M_1 – mirror HR = 99%, M_2, M_3, M_4, M_5, M_6 – high reflection mirrors, L_1, L_2, L_3, L_4, L_5 – lenses, SM – spherical mirror whose radius of curvature is R = 500 mm, MC – measurement circuit. Neodymium-doped yttrium orthovanadate 3 × 3 × 5 mm^3 *a*-cut crystals with 1% doping level were used

Capacitive photovoltage measurements of Si diodes containing porous Si surface layers were carried out within the wavelength range from 400 to 1200 nm. The experimental setup is illustrated in Fig. 2.9. The light from a halogen lamp was directed through a monochromator and beam splitter onto the sample under investigation. A non-destructive method was employed using a press-on ITO electrode with an approximate area of 7 × 7 mm² (Kostylyov et al., 2021).

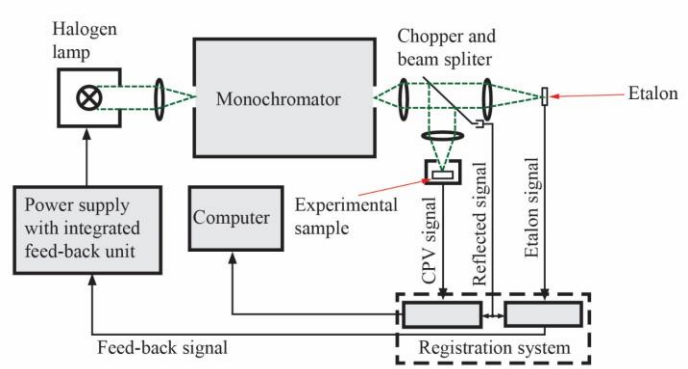

Fig. 2.9. Schematic experimental setup for detection capacitive photovoltage signal of Si diodes containing surface PSi layer (Kostylyov et al., 2021)

A silicon etalon photodiode is used as a reference photosensor. To ensure lock-in amplification, an AC voltage with a frequency of 20 Hz ran an oscillating beam splitter providing a reference signal. The spectral measurements were carried out at the Center for Testing of photoconverters and photoelectric modules, located at the V.E. Lashkaryov Institute of Semiconductor Physics of the NAS of Ukraine.

2.3. Program software

The separation of photovoltage into its components was simulated by the programming and numeric computing platform MatLab.

Table 2.1. MatLab script for solving differential equations

Script	Explanation
clc;	clears all the text from the Command Window;
close all;	to close all open figures, use the command;
clear all;	to clear all variables from the current workspace
s=dsolve(‘Dy=(((LaserPulse)))^q)/DecayConstant),y(0)=0’)	solves the differential equation with conditions, where “s” is the expected solution; LaserPulse is a fitting function of a laser pulse, DecayConstant is the relocation time for the necessary photovoltage component, and y(0)=0 is the initial condition for the deferential equation.

The developed model assumed that the *p–n* junction could be described as a first-order linear time-invariant system (Won et al., 2009). MatLab software was used to solve the differential equations. The MatLab script with explanations is attached in Table 2.1.

The energy band diagram of the ratchet-based GaAs/$Al_xGa_{1-x}As$ was modelled by Poisson 1D for the PC program. The program calculated diagrams for all investigated structures by solving the one-dimensional Poisson and Schrodinger equations self-consistently.

The share of spectrum absorbed by a single junction solar cell having the potential to heat the carrier was calculated by means of the OriginPro program.

2.4. Conclusions of the Second Chapter

1. GaAs *p–n* photodiodes were chosen for the investigation since they are direct semiconductors, and their band gap is close to the one corresponding to the maximum SC efficiency evaluated by the Shockley–Queisser theory. Si solar cells were chosen to reveal the hot carrier phenomenon in industrial solar cells. The Si diodes containing porous surface layers were chosen due to simple manufacturing technology and the possibility of creating the graded (varying) forbidden energy gap.
2. The ratchet-based sensor was developed to obtain a comparably small height of the potential barrier, which does not depend on ambient temperature. The small barriers can open the possibility of using this structure in detecting infrared (long wavelength) light, and the wide band gap prevents the classical electron–hole generation, which makes the investigation of the HC effect better.
3. The laser wavelengths were chosen with respect to the width of the band gap of the investigated materials. The photon energies were lower than the band gap of the samples, which could minimise interband absorption, thereby avoiding suppression of the hot carrier photocurrent across the samples. Also, a laser is a useful tool to investigate the HC effect due to high monochromatic light intensity and short pulsed light.

3

Results of Investigation of the Hot Carrier Effect

Investigating and understanding the hot carrier effect is important for improving the operation of PV devices. This chapter presents an experimental investigation of the hot carrier effect, focusing on the methodologies and techniques described in the Second Chapter.

By using the prepared samples, precise optical excitation, temperature control, and modelling methods, the chapter gives an explanation of the behaviour of carriers with excess energy and their impact on the output signal of PV devices (Ašmontas, Fedorenko et al., 2020; Gradauskas et al., 2022; Gradauskas, Ašmontas, Sužiedėlis, Šilėnas, Vaičikauskas et al., 2020; Masalskyi, Gradauskas & Zharchenko, 2022; Masalskyi, Gradauskas, Ašmontas et al., 2022a; Masalskyi & Gradauskas, 2021b, 2022). The acquired knowledge from such investigations guides the development of novel device structures and optimisation strategies to minimise losses caused by hot carriers.

3.1. Dependence of hot carrier photocurrent on the bias voltage

The influence of bias voltage on hot carrier photocurrent can be determined by assuming that the device usually operates unbiased, forward or reverse-biased. Under equilibrium conditions, the height of the potential barrier can be expressed as (Sze & Ng, 2006):

$$V_{\mathrm{bi}} = \frac{kT}{q} ln\left(\frac{N_{\mathrm{A}} N_{\mathrm{D}}}{n_{\mathrm{i}}^2}\right). \tag{3.1}$$

Here, N_{A} is the acceptor concentration, N_{D} is the donor concentration, and n_{i} is the intrinsic carrier concentration.

The resistivity of the depletion region is higher than the rest of the device; thus, almost all of the applied voltage drops across the depletion region. When the forward bias is applied to a *p–n* junction, an external electric field has an opposite direction with respect to the built-in internal field in the depletion region. Then, the total electric field is a difference between these two fields (minus sign in Eq. 3.2). When a reverse bias is applied, the total electric field is the sum of the field in the depletion region and the applied bias field (plus sign in Eq. 3.2). The height of potential barrier can be expressed as (Sze & Ng, 2006):

$$V_{\mathrm{bi}} = \frac{kT}{q} ln\left(\frac{N_{\mathrm{A}} N_{\mathrm{D}}}{n_{\mathrm{i}}^2}\right) \mp U_{\mathrm{b}}. \tag{3.2}$$

To investigate hot carrier photocurrent dependence on bias voltage, the samples containing *p–n* junction, GaAs photodiodes and Si industrial solar cells were exposed to pulsed laser light. The illumination wavelength of 1.064 μm ($h\nu = 1.16$ eV) and 1.34 μm ($h\nu = 0.92$ eV) was used with respect to the band gap width of the materials:

1. As for GaAs, wavelengths were chosen because the photon energy of the laser light was lower than the band gap, which allowed to avoid generation due to single-photon absorption.
2. As for Si, the first wavelength was chosen to check the possibility of observing the hot carrier and the classical photocurrent simultaneously. The second wavelength was expected to be long enough to prevent single-photon electron–hole pair generation.

According to the developed model of photovoltage formation (Fig. 3.1), three mechanisms can be distinguished: electron–hole pair generation (process 1), free electron heating (process 2; or corresponding hole heating, not shown in the picture), and electron–hole pair generation with simultaneous carrier heating process by absorption of photon with energy higher than the band gap (process 3) (Gradauskas, Ašmontas, Sužiedėlis, Šilėnas, Vaičikauskas et al., 2020).

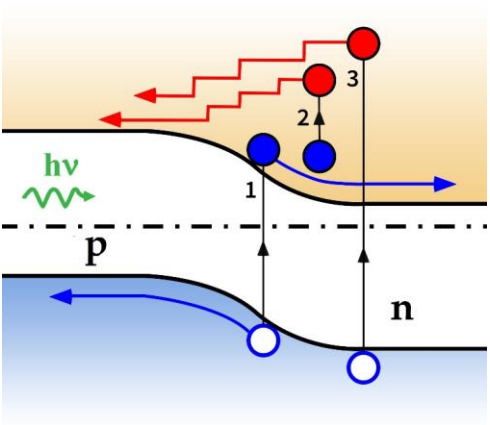

Fig. 3.1. Model of photovoltage formation across *p–n* junction. Red stepped arrows indicate diffusion and gradual thermalisation of a hot carrier, and blue arrows indicate a drift of electrons and holes in a built-in internal electric field (Gradauskas, Ašmontas, Sužiedėlis, Šilėnas, Vaičikauskas et al., 2020)

Fig. 3.2 shows *I–V* curves of GaAs and Si samples exposed to 1.064 μm and 1.342 μm-long laser radiation of the same light intensity of 0.4 MW/cm^2 at room temperature.

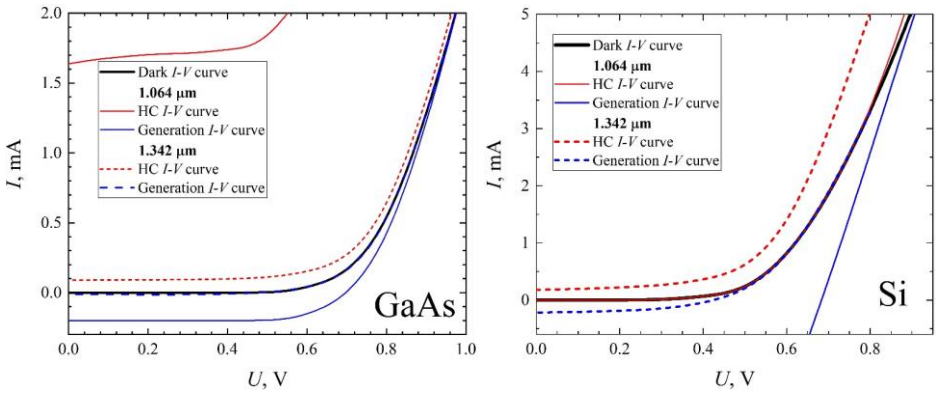

(a) (b)

Fig. 3.2. *I–V* characteristics of (a) GaAs and (b) Si *p–n* junctions illuminated with 1.064 μm (solid lines) and 1.342 μm (dashed lines) wavelength laser light of 0.4 MW/cm^2 intensity. The black line is *I–V* curve in the dark, red line indicates the hot carrier photocurrent, blue line shows the photocurrent caused by the generation of electron–hole pairs (Masalskyi, Gradauskas, Ašmontas, Sužiedėlis, Šilėnas et al., 2021; Masalskyi, Gradauskas, Ašmontas, Sužiedėlis, Širmulis et al., 2021)

In GaAs (Fig. 3.2a), the magnitude of both hot carrier and generation short circuit current under 1.342 μm illumination were smaller as compared to 1.064 μm-long excitation. Obviously, its magnitude has a strong dependence on photon energy. The results show that the generation current magnitude in the short circuit mode drops down 20 times while the hot carrier current only drops down by 15. It means that the change of the photon energy closer towards the band gap much more strongly affects the interband absorption than the intraband one due to a shaper increase in the absorption coefficient of the interband absorption (Dargys & Kundrotas, 1994).

In Si (Fig. 3.2b), it is obvious that the generation photocurrent rises stronger than the hot carrier one when the photon energy is higher than the band gap. The HC photocurrent can be seen at high values of external bias when the potential barrier is low enough.

Forward bias voltage puts favourable conditions for the flow of hot carriers across the lowered potential barrier of a *p–n* junction (Fig. 3.3a) as compared to the barrier heightened by the reverse bias (Fig. 3.3b).

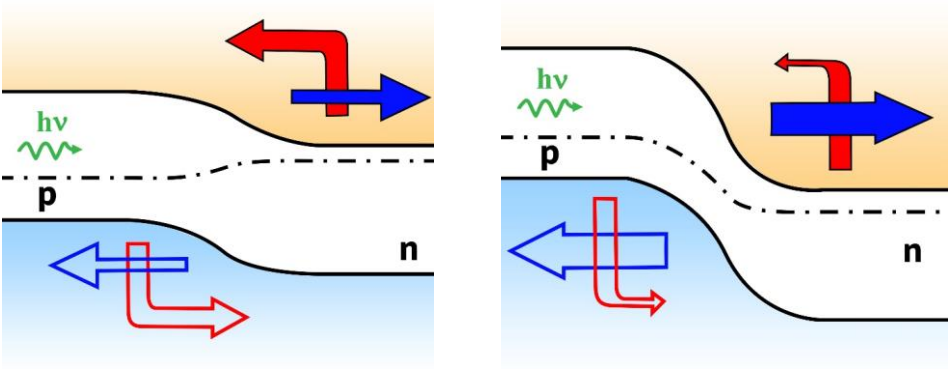

(a) (b)

Fig. 3.3. Schematic description of the hot carrier (red arrows) and generation-induced carrier (blue arrow) flow when forward (a) and reverse (b) bias voltage is applied (Gradauskas, Ašmontas, Sužiedėlis, Šilėnas, Čerškus et al., 2020a)

Indeed, the experiments reveal that the hot carrier photocurrent increases with the forward bias voltage (Fig. 3.4). When the *p–n* junction is opened, the hot carrier photocurrent rises exponentially. Further application of forward bias leads to saturation of the HC photocurrent because of the Joule heating effect (Umeno et al., 1978).

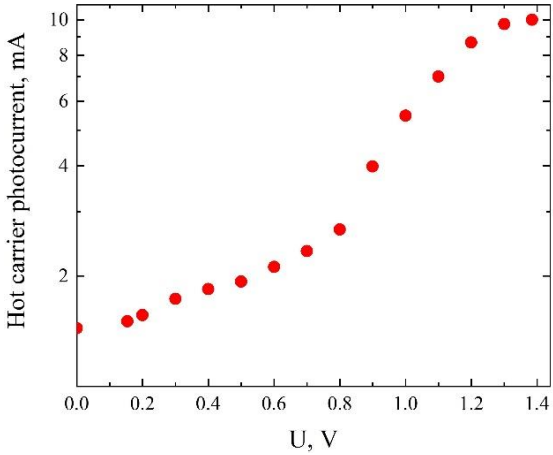

Fig. 3.4. Dependence of the hot carrier photocurrent on bias voltage across GaAs *p–n* junction illuminated with 1.064 μm wavelength at 3.6 MW/cm^2 light intensity and room temperature (created by the author)

It is worth noting that a single junction solar cell is forwardly biased by the generated electron–hole pairs, which works for the good of the hot carrier flow across the junction. Moreover, in the mode of max power, as shown in Fig. 1.2, an SC operates at forward bias, which means favourable conditions for hot carrier photocurrent flow and, thus, a negative influence on solar cell operation.

3.2. Composition of photovoltage signal across gallium arsenide *p–n* junction

According to the classical Shockley–Queisser theory, the illumination of a semiconductor with energy larger than its band gap leads to electron–hole pair generation. As a result, the classical photovoltage is induced across a *p–n* junction due to the separation of electrons and holes in the internal built-in electric field (Fig. 3, process 3). Extra photon energy left after the pair generation is used for the lattice heating. The theory also assumes that photons having lower energy than the width of the band gap are not absorbed at all (Shockley & Queisser, 1961).

The developed approach assumes the possibility of the presence of two additional mechanisms causing the rise of photovoltage with polarity opposite to the classical. When the photon energy is lower than the band gap, the intraband-free carrier absorption leads to carrier heating (Fig. 3.1, process 2). As a result, the hot carrier photovoltage is induced across a potential barrier with the following lattice heating. The polarity of the hot carrier photovoltage is opposite to the classical

photovoltage (Fig. 3.1, process 1). When the photon energy is much higher than the band gap, the interband absorption leads to electron–hole pair generation (Fig. 3.1, process 3). The remaining extra energy is used to excite the free carriers into the hot ones. The carriers can overcome the potential barrier and, this way, induce photovoltage across it before losing the extra energy (Ašmontas, Gradauskas et al., 2020).

In general, illumination-induced photocurrent across a *p–n* junction consists of three components. The first component, U_{G}, is caused by an electron–hole pair generation (classical photovoltage), and its speed is determined by the rate of the recombination process. The second one, U_{hc}, has opposite polarity and follows the laser pulse shape; this is an inherent feature of the hot carrier photovoltage since its speed is fundamentally determined by the carrier energy relaxation time, which is typical of the order of picoseconds in semiconductors. The third one, U_{T}, has the same polarity as U_{hc} but is much slower; it is attributed to the thermoelectric electromotive force caused by the lattice heating resulting from the hot carrier thermalisation.

The GaAs samples were illuminated with laser light of 1.064 μm wavelength to prove the developed approach. The laser had the same parameters as in the previous section 3.1.

Fig. 3.5 shows oscilloscope traces of photocurrent (photovoltage across 50 Ohm resistance in Fig. 2.5) pulse across illuminated GaAs *p–n* junction at different laser intensities.

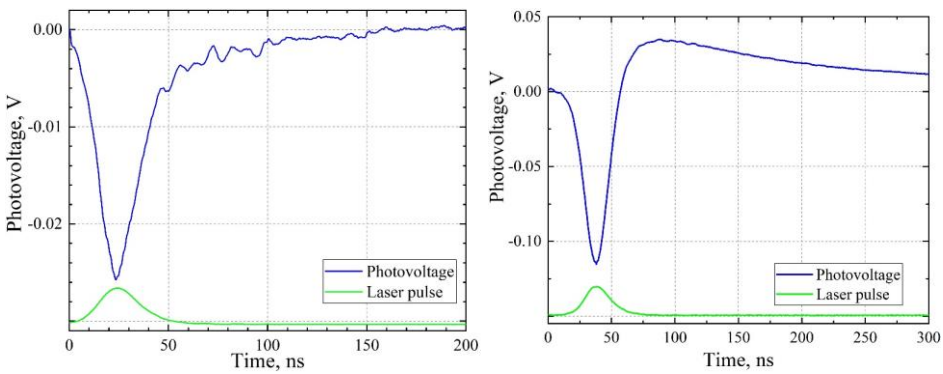

(a) (b)

Fig. 3.5. Oscilloscope traces of photovoltage across GaAs *p–n* junction (blue) illuminated with 1.064 μm laser pulse (green) of 51 kW/cm^2 (a) and 264 kW/cm^2 (b) intensity. No bias voltage is applied (Masalskyi, Gradauskas & Zharchenko, 2022)

The negative polarity pulse is supposed to be the sum of U_{hc} and U_{T} components (Fig. 3.5a). The laser intensity is not enough to induce the classical photovoltage due to the multiphoton interband absorption. It is approximately possible to distinguish two components in time. The hot carrier signal follows the laser pulse, i.e., when the pulse is gone, the HC photovoltage is gone also. The "tail" of the signal is attributed to the process of the lattice heating. Another situation is depicted in Fig. 3.5b, when, under the action of higher light intensity, the photovoltage has two different polarities. As in the previous situation, the negative polarity is a sum of U_{hc} and U_{T}, and the positive polarity relates to the classical photovoltage U_{G}. The absence of classical photovoltage at low laser intensity correlates with results depicted in Fig. 3.6, where the dependence of photovoltage pulses of positive and negative polarity on laser intensity is shown. The measured peak value of the negative component shows a linear dependence on the laser intensity (red circles); this is an inherent feature of the intraband absorption ($h\nu < E_{\mathrm{g}}$) and thermal effects. The positive component follows the square law (blue triangles), thus proving its origin to be related to the mechanism of two-photon absorption. It is worth noting that the generation-caused component is observed only at high intensities (approximately starting from 200 kW/cm^2) while the negative polarity of the signal is detected on the whole studied range.

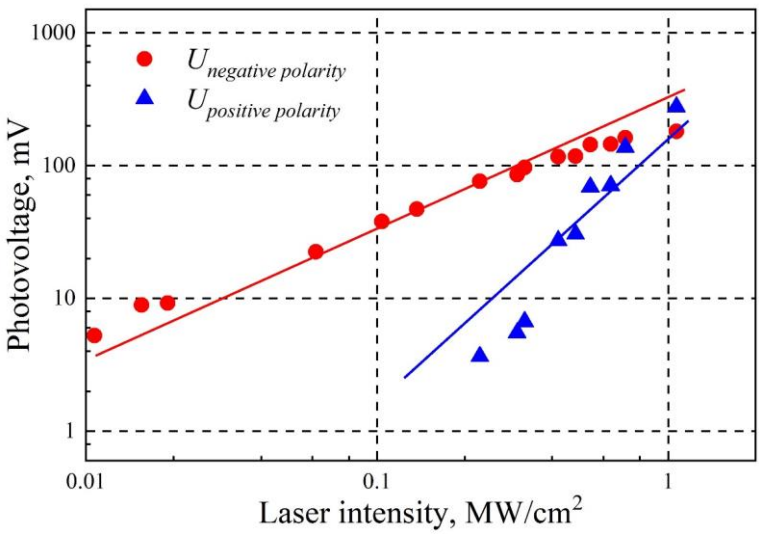

Fig. 3.6. Dependence of peak values of the negative polarity (red dots) and positive polarity (blue triangles) sub-pulses of the photovoltage on laser intensity induced across GaAs *p–n* junction illuminated with 1.064 μm wavelength at zero bias. Solid lines are guides for the eye of linear (red) and square (blue) dependence (Gradauskas, Ašmontas, Sužiedėlis, Šilėnas, Vaičikauskas et al., 2020)

As mentioned above, the total photovoltage across the GaAs *p–n* junction is composed of three components (Gradauskas, Ašmontas, Sužiedėlis, Šilėnas, Vaičikauskas et al., 2020)

$$U(t) = U_{\mathrm{hc}}(t) + U_{\mathrm{T}}(t) + U_{\mathrm{G}}(t). \tag{3.3}$$

Here, U_{G} is the photovoltage that is caused by an electron–hole pair generation, U_{hc} is the photovoltage that is caused by free carrier heating, and U_{T} is the photovoltage attributed to lattice heating resulting from the hot carrier thermalisation.

The developed model assumes that the *p–n* junction can be described as the linear time-invariant system (Won et al., 2009), and the time dependence of photovoltage can be characterised by the differential equation (Gradauskas, Ašmontas, Sužiedėlis, Šilėnas, Vaičikauskas et al., 2020) as:

$$\tau \frac{dU}{dt} + U = \overline{U}(t). \tag{3.4}$$

Here, τ is the exponential decay constant, and $U = U(t)$ is the photovoltage function of time. $\overline{U}(t)$ is the forcing function, and it depends on the laser pulse and on the physical phenomenon giving rise to a particular photovoltage component. The exponential decay time constant of each of the components was determined separately. The generation-related time constant τ_{G} was measured as the exponential decay far after the laser pulse was gone, and it was equal to 155 ns. Since hot carrier energy relaxation time in GaAs is of the order of one picosecond (Glover, 2003), it means that the free carriers are hot as long as the laser pulse is present, and τ_{hc} is equal to the laser rise-time τ_{p} that is equal to 33 ns. The value of the relaxation time decay constant τ_{T} was estimated to equal 50 ns by using the method of the transient thermoelectric effect (Sasaki et al., 1998): one side of the barrierless *n*-GaAs sample was illuminated with laser light of intensity less than 200 kW/cm^2, and the thermoelectric force was investigated.

The shape of the laser pulse was approximated as (Grigor′ev et al., 1971):

$$I_{\mathrm{L}}(t) = I_{\mathrm{p}} \left(\frac{t}{\tau_{\mathrm{p}}}\right)^{\mathrm{m}} exp\left[m\left(1 - \frac{t}{\tau_{\mathrm{p}}}\right)\right]. \tag{3.5}$$

Here, I_{p} is the peak intensity, and $I_{\mathrm{p}} = I(\tau_{\mathrm{p}})$. The best fit with the experimental laser pulse shape was achieved with index m = 10.

The generation of an electron–hole pair is caused by the nonlinear phenomenon of the two-photon absorption. Therefore, the forcing function has a square dependence on the laser intensity (Gradauskas, Ašmontas, Sužiedėlis, Šilėnas, Vaičikauskas et al., 2020):

$$\overline{U}_{\mathrm{G}}(t) = K_{\mathrm{G}} {I_{\mathrm{L}}}^2(t). \tag{3.6}$$

Here, K_G is the amplification coefficient, which was chosen to fit the magnitude of the experimental photovoltage.

The hot carrier component is caused by a linear process of free carrier heating. U_{hc} can be expressed as:

$$U_{hc}(t) = K_{hc} I_L(t). \tag{3.7}$$

Here, K_{hc} is the amplification coefficient that was chosen to match the magnitude of photovoltage.

The thermal process related to lattice heating is a linear phenomenon. The forcing function of the lattice heating linearly depends on the laser intensity:

$$\overline{U}_T(t) = K_T I_L(t). \tag{3.8}$$

Here, the value of K_T was estimated to fit the photovoltage signal shape.

The results of the three components induced across the *p–n* junction were calculated using Eqs. 3.3–3.8, as depicted in Fig. 3.7.

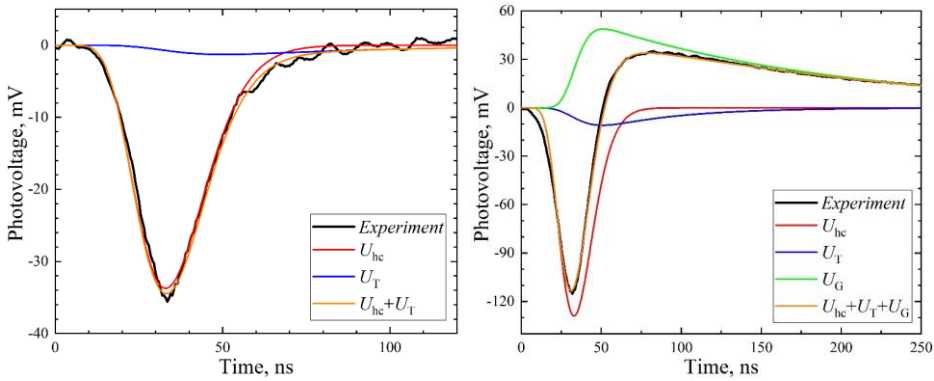

(a) (b)

Fig. 3.7. Photovoltage pulse simulation under (a) 51 kW/cm^2 and (b) 264 kW/cm^2 excitation. U_G – carrier generation-induced component (green); U_{hc} – hot carrier photovoltage (red); U_T – thermal lattice heating-caused photovoltage (blue), and the sum of the components (orange). For comparison, the experimental photovoltage trace is shown in black (Gradauskas et al., 2021; Masalskyi & Gradauskas, 2021b)

Several points should be noted. First, the experimental value of the U_G component is lower than the modelled. It means that the difference in magnitude occurs because of the competition of both negative and positive polarities of the photovoltage in the output signal. Second, the modelled and the measured U_{hc} component peak values differ over the entire range of measured power. The influ-

ence of the other two components caused this change: U_{T} supports the experimental U_{hc} at low intensities (Fig. 3.7a), and U_{G} cuts down U_{hc} at higher laser intensities (Fig. 3.6 and Fig. 3.7b). Third, the input of the slow lattice heating-caused component U_{T} seems to increase at a higher excitation level since part of the energy remaining from the electron–hole generation is most probably used to heat the carriers and to support the formation of the hot carrier photovoltage (Gradauskas, Ašmontas, Sužiedėlis, Šilėnas, Vaičikauskas et al., 2020; Masalskyi, Gradauskas, Ašmontas et al., 2022).

3.3. Temperature dependence of hot carrier photocurrent across gallium arsenide *p–n* junction

The research is initiated to determine the peculiarities of the hot carrier effect with temperature. The hot electron energy relaxation time at 80 K is ten times longer than at room temperature (Dargys & Kundrotas, 1994). It means that the influence of hot carriers is supposed to be stronger at lower temperatures since they can longer stay "hot". Such results were shown by Ašmontas et al. (1996), where the magnitude of HC photo signal at 80 K temperature was measured higher as compared to the room temperature results across GaAs *p–n* junction.

Fig. 3.8 shows *I–V* characteristics with and without illumination across GaAs *p–n* junction at 80 K and 300 K temperatures under pulsed laser illumination of 1.064 μm wavelength and pulse duration 25 ns at different laser light intensities.

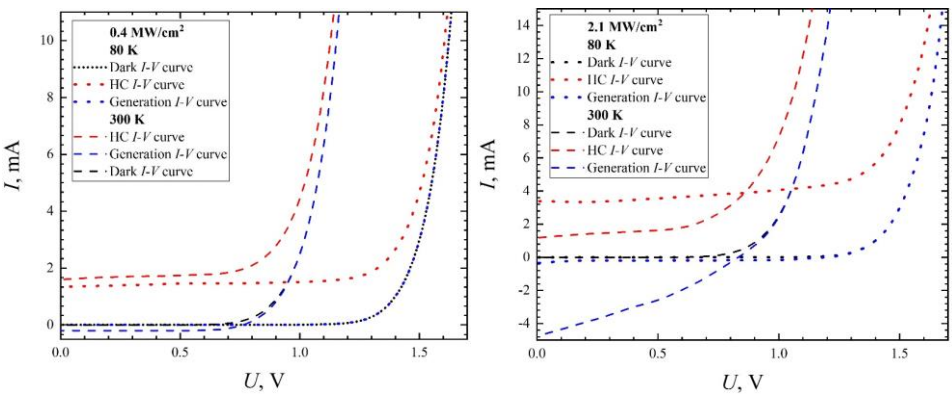

(a) (b)

Fig. 3.8. *I–V* characteristics of dark (black line) hot carriers (red line) and classical (blue line) photocurrent at 80 K (solid line) and 300 K (dashed line) temperatures under laser illumination of 1.064 μm wavelength at various light intensities: (a) 0.4 MW/cm^2 and (b) 2.1 MW/cm^2 (created by the author)

The results in Fig. 3.8a show the absence of generation-caused photocurrent at low temperatures. It can be explained by the widening of the band gap, which significantly determines the probability of two-photon absorption and a lower absorption coefficient (Dargys & Kundrotas, 1994). The reasons for smaller HC current at a lower temperature, taking about the short-circuit current mode, are the lower value of the intraband absorption coefficient (Dargys & Kundrotas, 1994) and the absence of additional energy for carrier heating from the two-photon absorption 0.9 eV, since two photons have $h\nu = 2.32$ eV and band gap of GaAs is equal 1.42 eV (Fig. 3.9b). These two factors together have a stronger influence on photocurrent than the longer relaxation time of the hot carriers. At room temperature, the laser intensity is enough (about 200 kW/cm^2) (Fig. 3.6) to induce the classical photocurrent caused by two-photon absorption. In this case, the hot carrier photocurrent arises via the intraband absorption and is supported by the energy that is left after the interband absorption (Fig. 3.9a). At higher intensities, the generation-caused photocurrent manifests itself even at 80 K since the laser power is increased (Fig. 3.8b). The short-circuit current of generation photocurrent has a lower value at 80 K than at 300 K because of the same reasons mentioned above.

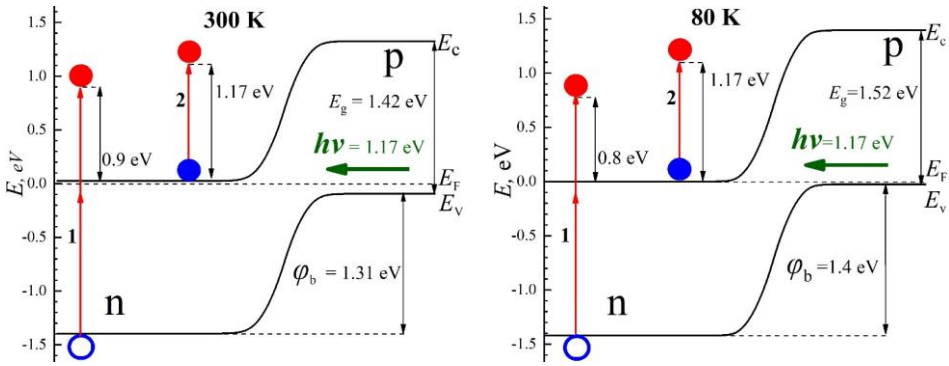

(a) (b)

Fig. **3.9**. Schematic band diagram of GaAs *p–n* junction and carrier excitation processes at (a) 300 K and (b) 80 K: 1 – interband two-photon absorption and 2 – intraband free carrier single photon absorption. φ_b is the height of the potential barrier, E_c is the bottom of the conduction band, E_v is the top of the valence band, and E_F is the Fermi level (created by the author)

The hot carrier signal at 80 K is higher than at 300 K, as was expected. The reasons for this can be the following: first, the longer relaxation time; second, the use of a portion of energy (0.8 eV) left after the interband absorption. The last reason is a square law dependence of the generation current on laser intensity

while the hot carrier current has a linear law (Fig. 3.6). In this case, the suppression action of the HC signal by generation current is stronger than supporting action of classical photoresponse by extra energy after intraband absorption.

Fig. 3.10 shows the dependence of hot carrier and generation short-circuit current across GaAs *p–n* junction on the temperature in the range of 80–300 K under 0.4 MW/cm^2 intensity (the same conditions as for Fig. 3.8a). The drop in the magnitude of the classical current is almost ten times at 80 K as compared to the room temperature, while the hot carrier photocurrent drop is only about 15%. The different behaviour of the currents was explained above. The notable fact is that the dependence character of the hot carrier and generation photocurrents is similar, which evidences the connectivity of both processes.

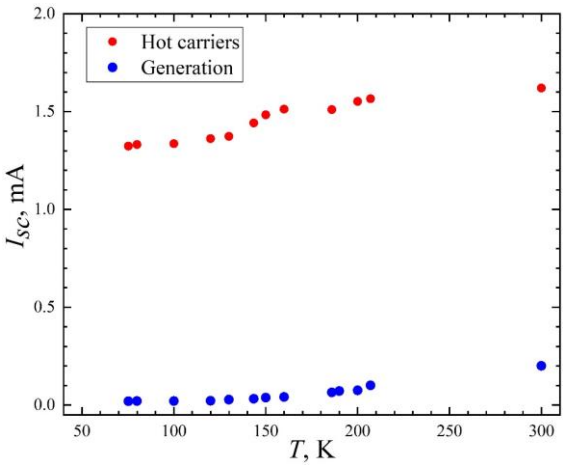

Fig. 3.10. Dependence of hot carrier (red dots) and generation (blue dots) short-circuit current on the temperature at 0.4 MW/cm^2 laser power of 1.064 μm wavelength (created by the author)

The *I–V* characteristics of GaAs *p–n* junction at two different temperatures are depicted in Fig. 3.11. The shift to the right of the *I–V* curves with lower temperatures can be described by the temperature coefficient of *I–V* characteristics. This coefficient is typical of each particular material.

The temperature coefficient gives the value of voltage drop per one degree at the constant current, and it is constant for any material with temperatures above 20 K. The coefficient can be described as (Schaffner & Shea, 1955):

$$\alpha_{\mathrm{T}} = \frac{\Delta U}{\Delta T} |i = const|. \tag{3.9}$$

Here, ΔU is the value of change in voltage and ΔT is the corresponding temperature change.

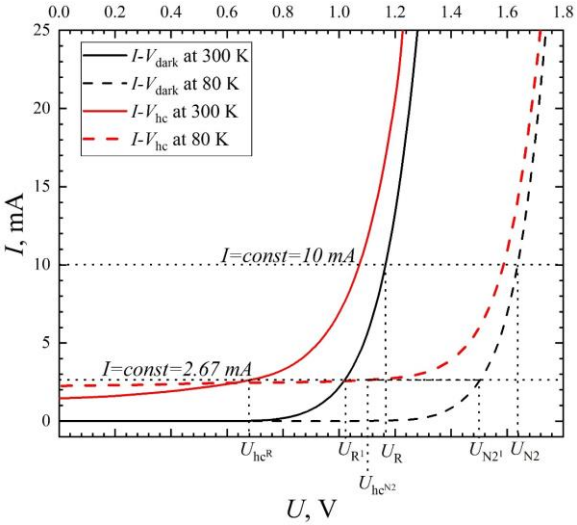

Fig. 3.11. *I–V* characteristics of GaAs *p–n* junction in the dark (black lines) and hot carrier (red lines) under laser illumination with intensity 0.7 MW/cm^2 of 1.064 μm wavelength. The solid lines represent 300 K and the dashed lines refer to 80 K temperature. The values of applied forward bias voltage are: U_R = 1.15 V, U_{N2} = 1.64 V, U_{hc}^R = 0.7 V, U_{hc}^{N2} = 1.1 V, U_R^1 = 1.03 V, U_{N2}^1 = 1.5 V (created by the author)

Thus, the coefficient can be calculated according to Eq. 3.9 and using data taken from Fig. 3.11:

$$\alpha_T = \frac{U_{N2} - U_R}{T_{N2} - T_R} = \frac{1.64\ \text{V} - 1.15\ \text{V}}{80\ \text{K} - 300\ \text{K}} = -2.2\ \text{mV/K}. \quad (3.10)$$

Here, U_{N2} is the voltage value taken from the I–V_{dark} characteristic at temperature 80 K, U_R is the voltage taken from the I–V_{dark} characteristic of 300 K temperature, T_{N2} is the temperature of liquid nitrogen, and T_R is the room temperature. All voltage values were taken at constant I = 10 mA. The obtained temperature coefficient was close enough to the calculated one –2.0 mV/K for GaAs solar cells (Landis et al., 2011).

To estimate the temperature of hot carriers in GaAs *p–n* junction, an initial point of voltage was taken corresponding to the opening mode of a *p–n* junction. In this case, the value of voltage is taken from the hot carrier *I–V* curve, and it equals U_{hc}^R = 0.7 V at the constant current 2.67 mA, which corresponds to the

voltage point at the *I–V* curve in the dark at room temperature and equals U_R^1 = 1.03 V. Using Eq. 3.9, the temperature change can be described as:

$$\Delta T = \frac{\Delta U}{\alpha_T} = \frac{1.03\ \mathrm{V} - 0.7\ \mathrm{V}}{0.0022\,\frac{V}{K}} = 154\ K. \tag{3.11}$$

Considering the ambient temperature of 300 K, the temperature of the hot carriers is equal to 454 K. The same philosophy was used to calculate the hot carrier temperature in liquid nitrogen at the same constant current value representing the same conditions of current flow across the *p–n* junction. As a result, the carrier temperature was equal to 262 K. Also, it should be noted that the carriers were heated up to 182 K in liquid nitrogen, while at room temperature, they were heated up to 154 K. It means that the heating process is stronger at low temperatures, which is connected to the increased of the energy relaxation time of the hot carriers (Dargys & Kundrotas, 1994). The obtained temperature change correlates with the results by Ašmontas et al. (1996), where the values of hot carriers photocurrent are higher at low than at room temperature.

The obtained results seem reasonable if compared with the findings of other researchers (Table 3.1).

Table 3.1. Hot carrier temperature values at 300 K ambient temperature

Material	Hot carrier temperature, K	Reference
In and GaAs	430	(Cavassilas et al., 2022)
GaAs	500–700	(Yang et al., 2016)
InGaAsP	300–1400	(Nguyen et al., 2018)

To see the density of occupied states by hot carriers by carrier statistics, the above-calculated temperature was used. In general, the density of occupied states by free electrons in the conduction band can be expressed (Sze & Ng, 2006):

$$n(E) = N(E)f(E). \tag{3.12}$$

Here, $f(E)$ is the Fermi–Dirac probability function, and $N(E)$ is the density of states in the conduction band. The density of occupied states by free holes in the valence band is (Sze & Ng, 2006):

$$p(E) = P(E)(1 - f(E)). \tag{3.13}$$

Here, $P(E)$ is the density of states in the valence band. The Fermi–Dirac function is expressed as (Sze & Ng, 2006):

$$f(E) = \frac{1}{1 + \exp\left(\frac{E - E_F}{kT_C}\right)}. \tag{3.14}$$

Here, E is the energy, T_c is the carrier temperature, E_F is the Fermi level energy. The Fermi–Dirac function describes the probability of carrier occupation energy levels in a semiconductor. Assuming that the temperature of the environment is 300 K, the energy of the Fermi level was recalculated using the equation (Sze & Ng, 2006):

$$E_F = \frac{E_c+E_v}{2} + \frac{kT}{2}\ln\left(\frac{N_v}{N_c}\right). \tag{3.15}$$

Here, E_c is the bottom energy of the conduction band (equals 1.42 eV), E_v is the top energy of the valence band (equals 0 eV), N_c is the effective density of states in the conduction band, N_v is the effective density of states in the valence band, and these are 4.5×10^{17} cm^{-3} and 1.2×10^{19} cm^{-3}, respectively, for GaAs. All values of the variables were taken from Dargys and Kundrotas (1994) at the temperature of 300 K. After the calculation, the value of E_F was equal to 0.75337 eV. It should be pointed out that the Fermi level shifts up and down from the middle position, and this shift depends on the doping level. Thus, the position of the Fermi level for *n*-type and *p*-type semiconductors can be found as (Sze & Ng, 2006):

$$E_F = E_c - kT\ln\left(\frac{N_c}{N_d}\right), \text{ for } n\text{-type.} \tag{3.16}$$

$$E_F = E_v + kT\ln\left(\frac{N_v}{N_a}\right), \text{ for } p\text{-type.} \tag{3.17}$$

Here, N_d is the donor concentration, N_a is the acceptor concentration; $N_d = 3 \times 10^{17}$ cm^{-3} and $N_a = 5 \times 10^{17}$ cm^{-3} in this case. Thus, $E_F = 1.40$ eV and $E_F = 0.082$ eV for the *n*- and *p*-type of GaAs, respectively. These values were also calculated by Poisson 1D for the PC program, which gave very similar results of $E_F = 1.405$ eV and $E_F = 0.084$ eV for the *n*- and *p*-type of GaAs, respectively.

The densities of states in the conduction and the valence bands can be found (Sze & Ng, 2006):

$$N(E) = \frac{M_c\sqrt{2}m_{de}^{3/2}\sqrt{E-E_c}}{\pi^2 h^3}, \text{ for } E > E_c. \tag{3.18}$$

$$P(E) = \frac{\sqrt{2}m_{dh}^{3/2}\sqrt{-E+E_v}}{\pi^2 h^3}, \text{ for } E < E_v. \tag{3.19}$$

Here, M_c is the number of equivalent maximums in the conduction band, h is the Planck constant, m_{de} is the effective electron mass of density states and m_{dh} is the effective hole mass of density states. It is more convenient to express $N(E)$ and $P(E)$ through the N_c and N_v since they are constants for particular temperatures, thus they are described as (Sze & Ng, 2006):

$$N_c = 2M_c\left(\frac{2\pi m_{de}kT}{h^2}\right)^{3/2}. \tag{3.20}$$

$$N_{\mathrm{v}} = 2\left(\frac{2\pi m_{\mathrm{he}} kT}{h^2}\right)^{3/2}. \tag{3.21}$$

After substituting Eq. (3.20) to Eq. (3.18) and Eq. (3.22) to Eq. (3.20), $N(E)$ and $P(E)$ are expressed as:

$$N(E) = \frac{N_{\mathrm{c}}\sqrt{E-E_{\mathrm{c}}}}{4\pi^{3.5}k^{1.5}T^{1.5}}, \textit{ for } E > E_{\mathrm{c}}. \tag{3.22}$$

$$P(E) = \frac{N_{\mathrm{v}}\sqrt{E_{\mathrm{v}}-E}}{4\pi^{3.5}k^{1.5}T^{1.5}}, \textit{ for } E < E_{\mathrm{v}}. \tag{3.23}$$

Using $f(E)$ from Eq. (3.14), $N(E)$ from Eq. (3.22), and $P(E)$ from Eq. (3.23), Eqs. (3.12) and (3.13) turn into:

$$n(E) = \frac{N_{\mathrm{c}}\sqrt{E-E_{c}}}{4\pi^{3.5}k^{1.5}T^{1.5}} \times \frac{1}{1+\exp\left(\frac{E-E_{\mathrm{F}}}{kT_{\mathrm{c}}}\right)}. \tag{3.24}$$

$$p(E) = \frac{N_{\mathrm{v}}\sqrt{E_{\mathrm{v}}-E}}{4\pi^{3.5}k^{1.5}T^{1.5}} \times \left(1 - \frac{1}{1+\exp\left(\frac{E-E_{\mathrm{F}}}{kT_{\mathrm{c}}}\right)}\right). \tag{3.25}$$

The calculated densities of states in the conduction and the valence band, the Fermi–Dirac function and concentrations of free electrons and holes for intrinsic GaAs at temperature 300 K are depicted in Fig. 3.12.

Eqs. 3.25 and 3.26 can be used to calculate the density of occupied states by free electrons and holes in the *p*- and *n*- regions of the *p*–*n* junction in GaAs. The result of the calculation is depicted in Fig. 3.13.

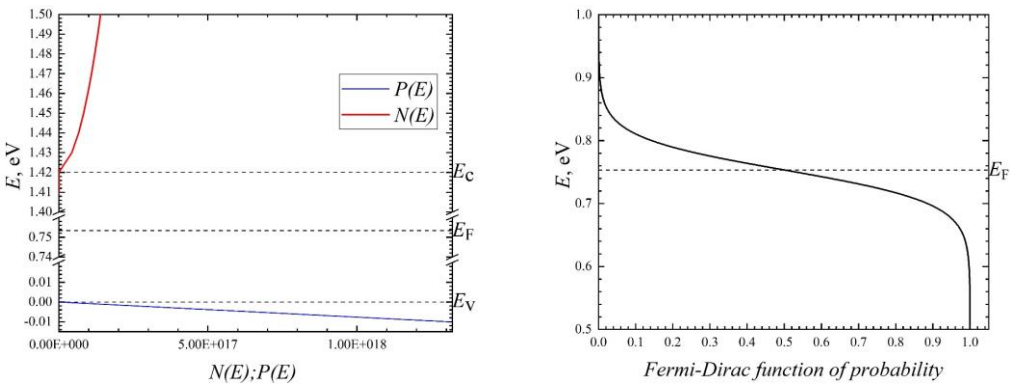

a) b)

Fig. 3.12. To be continued

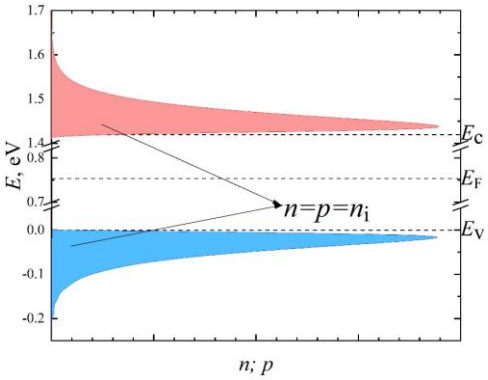

c)

Fig. **3.12**. (a) Density of states in the conduction and valence bands, (b) the Fermi–Dirac probability function for carriers having temperature 300 K, and (c) the density of occupied states by electrons and holes per unit volume and energy in intrinsic GaAs (created by the author)

Two situations are analysed in Fig. 3.13 to compare free carrier concentrations under conditions when the temperature of hot carriers was calculated.

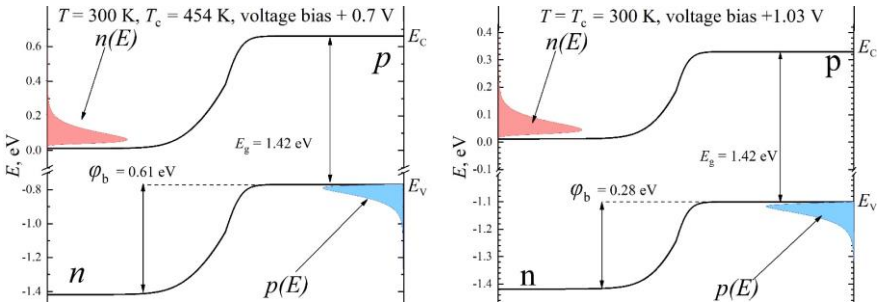

(a) (b)

Fig. **3.13**. Schematic model of concentrations of free electrons and holes in GaAs *p–n* junction (a) U_{hc}^{R} = 0.7 V, forward voltage bias and carrier temperature 454 K; (b) U_{R}^{1} = 1.03 V forward voltage bias and carrier temperature 300 K. φ_b is the height of the potential barrier (created by the author)

Fig. 3.13a shows that carriers have a temperature of 454 K while the lattice temperature is 300 K. The potential barrier is still high, even when biased with 0.7 V. The peak value of $n(E)$ and $p(E)$ are much less than the height of the potential barrier. This supports the hypothesis that hot carriers cannot diffuse over the barrier, and most probably, the current has a recombination character.

Fig. 3.13b shows the situation when the dark current ($T = T_c$ 300 K) has the same value as the hot carrier, i.e., the conditions for the current flow are similar. The potential barrier is still higher than the peak values of the free electron and hole concentrations, which means that the currents have a recombination character. Also, the assumption that the hot carrier current has a recombination mechanism is supported by even a separate excited carrier having excess energy of 1.17 eV (Fig. 3.9, process 2), which does not have enough energy to diffuse over the potential barrier.

It is worth mentioning that in an unbiased *p–n* junction, the carrier should have at least 2500 K temperature to diffuse over the barrier and induce the current. The temperature value was calculated in such a way that part of the carrier statistics was at the same energy level as the potential barrier height.

3.4. Modelling of absorption spectra

As mentioned in the First Chapter, solar cells have two types of losses: extrinsic and intrinsic. The below band gap and thermalisation losses are assumed to be the main mechanisms of intrinsic losses. On the one hand, they comprise about 80% (occupancy share depends on material) of whole intrinsic losses (Hirst & Ekins-Daukes, 2011). On the other hand, the absorption of photons having energy higher and lower than the band gap is a reason for the appearance of hot carrier photoresponse across a *p–n* junction, which can be treated as another kind of spectral loss. Therefore, the absorption spectra were modelled to calculate the portion of the whole solar radiation that has the potential to heat carriers.

The investigated materials are Si and GaAs. Silicon is the most widespread semiconductor for solar cell fabrication, and GaAs for its 1.42 eV width of the band gap, which is close to the optimal value to reach the maximum efficiency (Fig. 1.3).

Part of solar radiation that generates electron–hole pairs can be described as (Masalskyi & Gradauskas, 2022):

$$I_G = I_0 \frac{E_g}{hv}, \quad for\ hv \geq E_g \tag{3.26}$$

Here, I_0 is the incident solar irradiation, and v is the frequency. Eq. (3.26) is applied for all photons with energy equal to or larger than the band gap.

The rest of the solar energy can be used for carrier heating and can be expressed as (Masalskyi & Gradauskas, 2022):

$$I_{hc} = \begin{cases} I_0 \frac{hv - E_g}{hv}, & for\ hv > E_g; \\ I_0 \quad , & for\ \ hv < E_g. \end{cases} \tag{3.27}$$

Two situations that lead to the carrier's heating are possible. First, when photons have energy higher than the band gap, they generate the heated electron–hole pairs (Fig. 3.9a, process 1). Second, photons having energy smaller than the band gap cause free carrier heating via the intraband absorption (Fig. 3.9a, process 2). It is worth noting that the described approach is applied at room temperature when all impurity levels are assumed to be ionised (Sze & Ng, 2006).

Fig. 3.14 shows the results of the calculation carried out using Eqs. (3.26) and (3.27). The standard AM 1.5 G has been used as an incident solar radiation.

The result of calculations (Table 3.2) revealed that 19.0% of the entire solar spectrum AM 1.5 G of low energy photons and 33.2% of high energy photons contribute to the process of carrier heating in silicon. The respective values are 33.0% and 21.7% for gallium arsenide. It means that even assuming that a solar cell absorbs the entire AM 1.5 G solar spectrum, more than half of it has the potential to heat carriers (Masalskyi & Gradauskas, 2022).

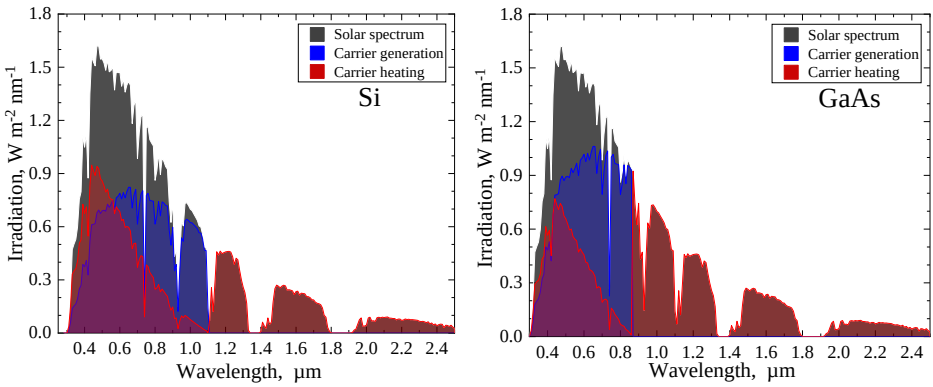

(a) (b)

Fig. 3.14. Terrestrial air mass 1.5 solar spectrum (grey), and its potential contributions to carrier generation (blue) and carrier heating (red) in silicon (a) and GaAs (b) (Masalskyi, Gradauskas & Zharchenko, 2022)

Table 3.2. Contributions of incident solar spectrum into electron–hole pair generation and carrier heating, as shown in Fig. 3.14

Solar spectrum contribution, %	Si	GaAs
Generation	47.8	45.3
Hot carriers ($h\nu < E_g$)	19	33.0
Hot carriers ($h\nu > E_g$)	33.2	21.7

Light absorption in a semiconductor should be considered. The absorbed part of incident light can be expressed by the Beer–Lambert–Bouguer law (the developed model does not consider the reflectivity of material):

$$I_{\mathrm{abs}} = 1 - I_0 e^{-\alpha \mathrm{d}}. \tag{3.28}$$

Here, α is the absorption coefficient of a material, and d is the light penetration depth. Values of α for inter- and intraband absorption were taken from references (Adachi, 1998; Dargys & Kundrotas, 1994; Green, 2008). Using Eq. (3.28) in Eqs. (3.26) and (3.27), the portions that go to the generation of electron–hole pairs and carrier heating can be described as (Masalskyi & Gradauskas, 2022):

$$I_{\mathrm{G-abs}} = \left(1 - I_0 e^{-\alpha \mathrm{d}}\right)\frac{E_{\mathrm{g}}}{h\nu}, \qquad for\ h\nu \geq E_{\mathrm{g}} \tag{3.29}$$

$$I_{hc-abs} = \begin{cases} \left(1 - I_0 e^{-\alpha d}\right)\frac{h\nu - E_{\mathrm{g}}}{h\nu}, & for\ h\nu > E_{\mathrm{g}}; \\ \left(1 - I_0 e^{-\alpha d}\right) \quad , & for\ \ h\nu < E_{\mathrm{g}}. \end{cases} \tag{3.30}$$

For the calculation of the absorbed portion of solar radiation, the *n*-type of silicon and GaAs were chosen since most solar cells have a *n*-type emitter. The thickness of the emitter layer was taken equal to 500 nm and doped with concentration $n = 10^{19–20}$ cm^{-3} (Masalskyi & Gradauskas, 2022).

The calculation results for Si and GaAs using Eqs. (3.29) and (3.30) are depicted in Fig. 3.15 and are summarised in Table 3.3.

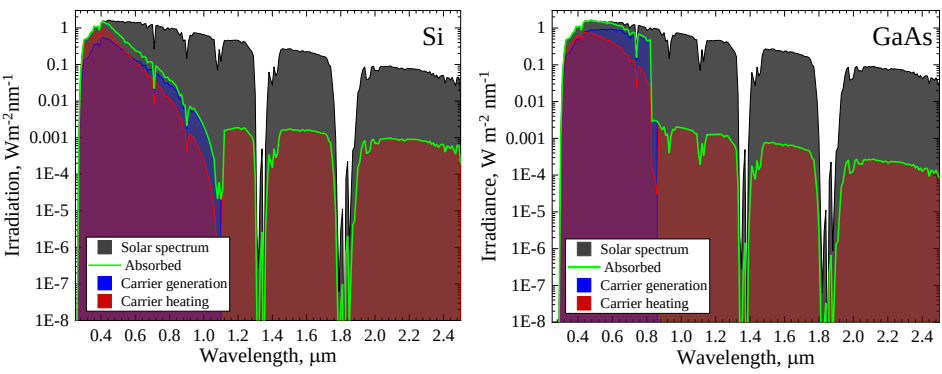

(a) (b)

Fig. 3.15. Solar spectrum AM 1.5 G (grey), its absorbed part (green line) and a portion of the absorbed part spent for carrier generation (blue area) and carrier heating (red area) in silicon (a) and GaAs (b), calculated using Eqs. (3.29) and (3.30). The carrier density is $n = 10^{19}$ cm^{-3}, and the light penetration depth is $d = 500$ nm for both materials (Masalskyi & Gradauskas, 2022)

Table 3.3. The contribution of solar spectrum absorbed by silicon and gallium arsenide as calculated according to Eqs. (3.29) and (3.30). The carrier density is equal to $n = 10^{19}$ cm^{-3}, and the light penetration depth is $d = 500$ nm

Absorbed solar spectrum contribution, %	Si	GaAs
Generation	40.2	63.5
Hot carriers ($h\nu < E_g$)	0.5	0.2
Hot carriers ($h\nu > E_g$)	59.3	36.3

The obtained results revealed that in silicon, 40.2% of the whole absorbed light goes to the classical electron–hole generation and 59.8% is spent on the carrier heating process. A small amount, only 0.5% of the absorbed photons with low energy (below the band gap), was used to heat the carriers. As for GaAs, 63.5% of the absorbed solar spectrum contributes to the ordinary carrier generation, and 36.5% is dedicated to carrier heating; the share of the absorbed low-energy photons ($h\nu < E_g$) of the entire AM 1.5 G that heats carriers amounts to 0.2%. It should be underlined that the approach assumes that all the absorbed photons with energy smaller than the band gap heat only free electrons (Masalskyi & Gradauskas, 2022).

The developed approach is further applied to show how significant can be the absorption of low-energy photons. In this way, various values of carrier concentration up to 10^{20} cm^{-3} of an emitter layer and its thickness up to 5 μm were analysed. The results of the calculation are depicted in Fig. 3.16 (Masalskyi & Gradauskas, 2022).

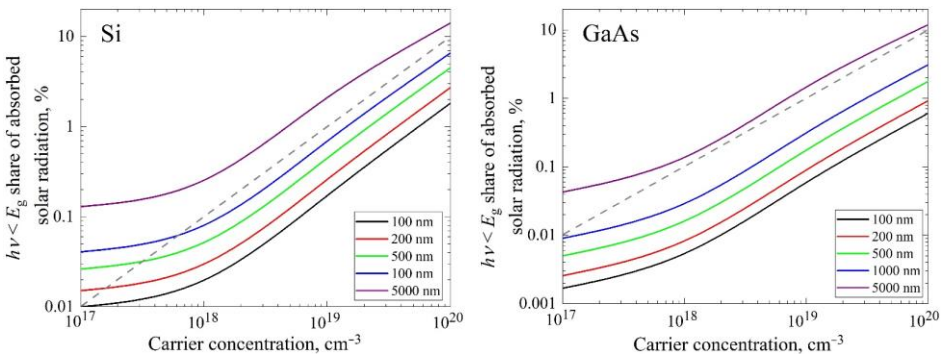

(a) (b)

Fig. 3.16. Dependence of absorbed below band gap solar radiation percentage on carrier concentration at various absorber thicknesses in Si (a) and GaAs (b). Dashed lines are guides for the eye of linear dependence (Masalskyi & Gradauskas, 2022)

Fig. 3.16 demonstrates an almost linear dependence of absorbed below-band gap solar radiation percentage on carrier density. The linear is well-expressed to observe at high concentration levels for both Si and GaAs. Linear dependence is an essential feature of intraband absorption (Dargys & Kundrotas, 1994). For the industrial silicon solar cells with their 0.5 μm-thick emitter doped up to $n = 10^{20}$ cm^{-3}, the share of absorbed solar spectrum AM 1.5 G can be more than 4% in the below band gap region. Such an amount of the absorbed below band gap solar light heats free carriers and induces hot carrier photovoltage with followed lattice heating. As a result, the classical photovoltage is suppressed.

As Table 3.3 shows, the wider band gap semiconductor absorbs a bigger portion of light for carrier generation, i.e., the radiation for carrier heating gets smaller.

The results also show that Si industrial solar cell absorbs only 26% of the entire solar spectrum (Fig. 3.15a, green line), and more than half of it has the potential to heat the carriers. This fact reveals that a huge share of the spectrum supports the rise of the hot carrier phenomenon that reduces SC's efficiency in industrial cells (Masalskyi & Gradauskas, 2022).

3.5. Suppression of hot carrier impact using porous silicon layer

A graded gap absorber in a solar cell is a relatively new technique for improving the efficiency and extending the absorption spectra of the devices. The layers with a variable width of the band gap (Fig. 3.17) can help to improve the SC efficiency by more than 5% (Aissat et al., 2018) as compared to the same structure without the graded gap layer.

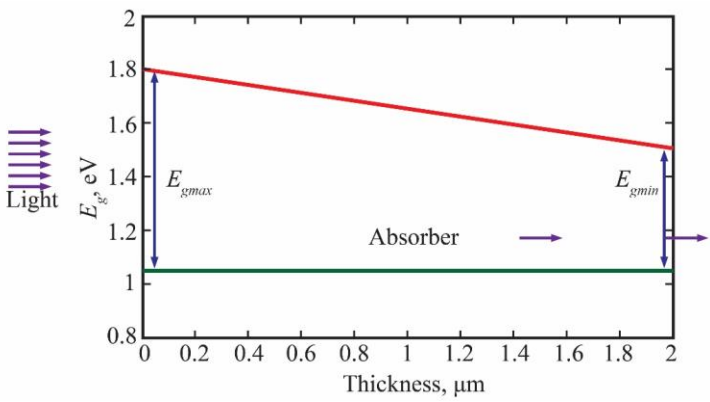

Fig. 3.17. Energy band diagram of a graded gap layer (Aissat et al., 2018)

The principle of light absorption in SC containing a graded gap surface layer is the same as in typical solar cells. The illumination falls from the side of a wider band gap (left side in Fig. 3.17). Thus, the photons with higher energy are absorbed, and photons having lower energy pass further. A photon is absorbed when its energy matches the particular band gap width. The graded gap layers are applied in the solar cells for two reasons: first, to prevent the absorption of photons with high energy, leading to the creation of hot carriers, and later, the lattice heating. Second, the graded gap layer induces an additional mechanism of photovoltage, which increases the total photovoltage of the cell.

Different methods exist for creating a graded gap layer. Šilėnas et al. (2014) reported that a layer can be formed by changing the composition of the material, for instance, in $Al_xGa_{1-x}As$ by changing the AlAs mole fraction "*x*". Another option is the fabrication of nano-sized structures, such as nanowires. In this case, the variable band gap occurs due to the quantum confinement effect (Medvid, 2010).

To investigate the suppression of the hot carrier impact, the porous layer was formed on the front side of the Si photodiodes; the structures were illuminated with the light of 8000 W/cm^2 intensity and of wavelength range 400–1200 nm (Ašmontas, Fedorenko et al., 2020).

Fig. 3.18 shows the spectral dependence of capacitive photovoltage induced across the samples with and without the porous Si (PSi) top layer.

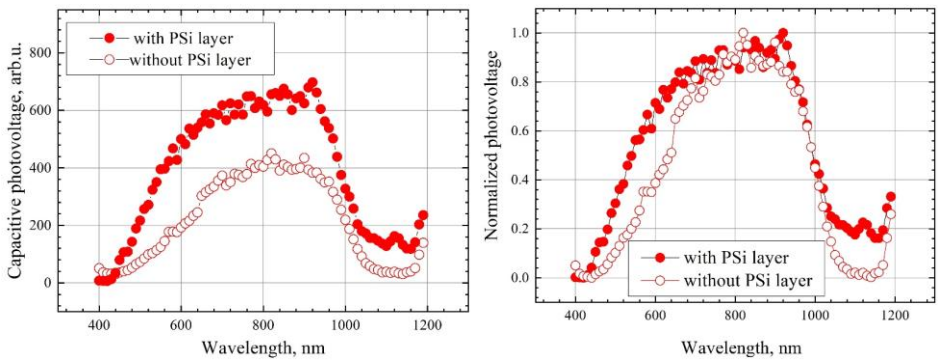

(a) (b)

Fig. 3.18. Capacitive photovoltage spectra (a) and normalised photovoltage (b) across Si *p–n* junction without (open dots) and with (solid dots) surface PSi layer (Masalskyi & Gradauskas, 2022)

Results in Fig. 3.18a reveal that the photovoltage is significantly influenced by the appearance of PSi. This layer decreases the reflectance coefficient. The PSi layer creates the n^+ region on the band offset with the *n*-region of a *p–n* junction, which reduces the recombination of the generated carriers.

Fig. 3.19 shows schematics of photo signal formation in the PSi top layer containing samples to explain the obtained results depicted in Fig. 3.18.

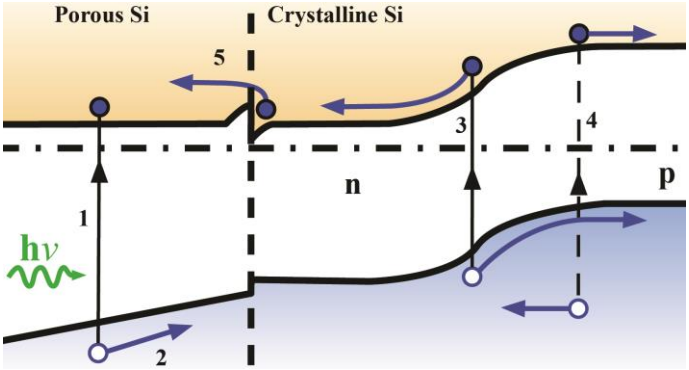

Fig. 3.19. Photosignal formation in silicon *p–n* junction covered with PSi layer: 1 − generation of electron–hole pair by a high-energy photon, 2 − hole drift in the electric field of the graded gap layer of PSi, 3 − classical photovoltage formation in *p–n* junction, 4 − generation of electron–hole pair by a high-energy photon and the corresponding hot-carrier photovoltage across *p–n* junction, and 5 − rise of photovoltage at the boundary PSi/crystalline Si (Ašmontas, Fedorenko et al., 2020)

In the developed structure, the total photovoltage across the sample increases not only due to decreased reflection but also due to additional processes 1, 2 and 5 (Fig. 3.19). All two photovoltages have the same polarity as the classical photovoltage (process 3). The photovoltage in the short-wavelength region (Fig. 3.18b) is raised as a result of the application of the graded-gap layer, which more effectively absorbs the high energy photons (processes 1 and 2) and thereby decreases the detrimental hot carrier impact on the output signal (process 4). Also, the intrinsic built-in electric field of the graded gap layer accelerates photogenerated holes (process 2). It means that photogenerated carriers overpass PSi and avoid significant recombination. Finally, the hot carrier photovoltage across the PSi/*n*-Si interface (process 5) extends the effective spectrum in the long-wavelength region (Fig. 3.18b).

As for the conclusion, the developed Si *p–n* junction containing the surface PSi layer has additional mechanisms composing the total photovoltage. These mechanisms are caused by the application of the graded gap surface PSi layer. In this case, the magnitude output signal of the diode is about 30% (at 800 nm wavelength) higher as compared to the same diode without a PSi layer. Also, the widening of the effective spectrum is observed: the spectrum becomes wider in long and short-wavelength regions.

3.6. Ratchet-based gallium arsenide/aluminium gallium arsenide electromagnetic radiation sensor

A radiation sensor is a passive electronic element that converts the energy of radiation into an electrical signal. These sensors are a valuable tool in many industries, especially in the rapidly developing modern laser technologies. Since the operation of a typical radiation sensor is related to the absorption of a light photon in the sensor material, they are usually divided into two types: thermal and quantum sensors.

Thermal sensors, such as bolometers or pyroelectric detectors, use electromagnetic radiation as a heat source. The quantum sensors are made of semiconductors, and their nature is determined by the band gap of the particular material, energy of impurity level or other energy levels. Therefore, these sensors are selective, and their operating range is limited by these energies. The sensitivity of the sensors is mostly determined by the type of absorption. The interband absorption is much stronger than the intraband one (Dargys & Kundrotas, 1994). Consequently, sensors that use interband absorption are more sensitive, but they can detect only photons having energy higher or equal to the band gap. This mechanism significantly limits the detectable radiation spectral range of sensors made of wide-bandgap semiconductors.

To detect the long-wavelength region, the quantum sensors are made of narrow-bandgap semiconductors; their operation usually requires low cryogenic temperatures (Ašmontas et al., 2003). The second way to detect this wavelength range can be realised via devices having band-modified structures, such as ratchet sensors (Tanaka et al., 2013), but their production requires complicated semiconductor structures, such as nanowires or asymmetric nano-sized metal gates based on the Schottky contact. The third way to detect the long wavelength is by using wide band gap semiconductors based on the hot carrier phenomenon; however, the sensitivity on these devices is low.

The proposed ratchet-based structure can be used for the detection of the long-wavelength range in an effort to avoid maintaining low cryogenic temperatures or applying complicated fabrication technology and also to supply the possibility to increase sensitivity. The photoresponse formation across the ratchet-based structure illuminated with radiation having photon energy lower than the band gap is depicted in Fig. 3.20.

The operation principle of the ratchet-based sensor is as follows. In the absence of radiation, free electrons are concentrated in the periodic potential wells of the conduction band.

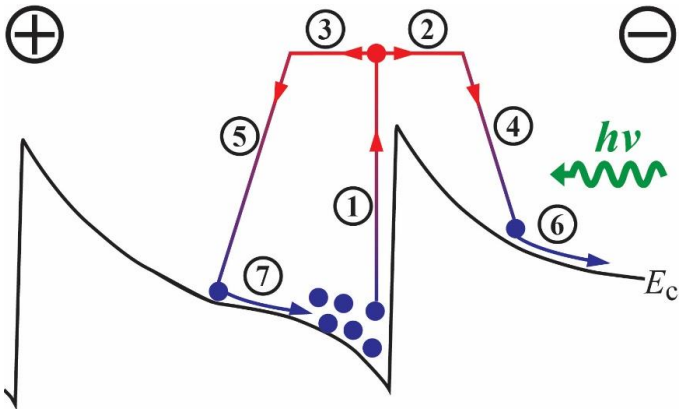

Fig. 3.20. Schematic energy band diagram of the ratchet-based structure (not to scale) and photoresponse formation across it illuminated with photon energy $hv < E_g$. 1 – intraband free electron excitation; 2 – diffusion of a hot electron across the band offset to the right towards adjacent potential well; 3 – diffusion of the hot electron to the left towards the graded gap region; 4, 5 – cooling of the hot electron to the edge of conduction band; 6 – drift of electron in the internal built-in electric field to the next potential well; 7 – drift of electron in the internal built-in electric field to the initial potential well (created by the author)

Under illumination, the average kinetic energy of electrons increases, and they become hot electrons. HCs rise above the band offset and diffuse in both directions (Fig. 3.20, processes 2 and 3). During the cooling down (Fig. 3.20, processes 4 and 5), the diffused electrons fall to the bottom of the conduction band and, under the action of the internal built-in electric field, drift to the bottom of a potential well. Some of the electrons diffuse over the closest band offset peak and reach another potential well (Fig. 3.20, process 6). The other part of electrons that have diffused to the opposite side returns to the initial potential well (Fig. 3.20, process 7). The proposed structure detects radiation having photon energy less than the smallest band gap of the active graded gap layers.

Based on the above consideration, the ratchet-based GaAs/$Al_{0.2}Ga_{0.8}As$ electromagnetic radiation sensor was developed. The AlAs mole fraction „x = 0.2“ provided a low band offset (about 151.5 meV) of the heterojunction. The height of the band offset was chosen with respect to the revealed hot carrier distribution (Fig. 3.13a) in the GaAs *p–n* junction. The height of the barrier allows the diffusion of hot carriers over the barrier. The thickness of the $Al_xGa_{1-x}As$ with “x = 0–0.2”, i.e., the distance between the potential wells was 1 μm (Fig. 2.4b), which is much longer than the diffusion length of hot carriers (<150 nm). Particularly, such thickness prevents the transport of the excited carriers to the next potential well on the left (Fig. 3.20, process 3).

During the experiments, the developed sensor was illuminated with laser radiation of 1.064 μm wavelength and up to 10 MW/cm^2 light intensity range. The illumination was targeted on the top $Al_{0.2}Ga_{0.8}As$ layer, and a diaphragm was used to avoid illumination of the ohmic contacts of the sample and induce photoresponse across them. The wavelength of the illumination was chosen with respect to the width of the band gap since the pure hot carrier effect was investigated. Fig. 3.21 provides the temporal behaviour of the illumination-induced photocurrents at 300 K and 80 K.

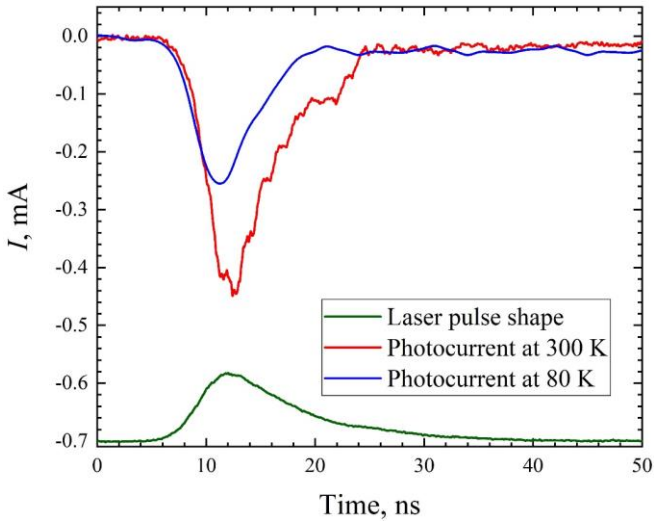

Fig. 3.21. Temporal behaviour of photocurrent induced across ratchet-based sensor under pulsed laser illumination of 1.064 μm at 7.5 MW/cm^2 light intensity. The green line indicates laser pulse shape (in arb. units), the blue line shows photocurrent at 80 K, and the red line represents photocurrent at 300 K (created by the author)

The photocurrent across the sensor is induced by processes 1, 2, 4, and 6 in Fig. 3.20. The polarity of the signal corresponds to the "+" and "–" polarity depicted in Fig. 3.20. The decrease in the detected signal at 80 K compared to 300 K can be attributed to several factors. First, the absorption coefficient of GaAs decreases as the temperature is reduced (Dargys & Kundrotas, 1994). This reduction in the absorption coefficient results in less light being absorbed by the material at lower temperatures. Secondly, at cryogenic temperatures, the intrinsic carrier concentration decreases (Dargys & Kundrotas, 1994). This decrease means fewer available carriers to contribute to the total photocurrent. Furthermore, although the energy relaxation time of free carriers increases by approximately ten times at 80 K (Dargys & Kundrotas, 1994), the diffusion length only increases by about

three times. This diffusion length is still smaller than the distance between band offsets (Fig. 3.20). As a result, hot carriers are unable to effectively diffuse to the previous potential well and induce a photocurrent with a positive polarity. The photocurrent across the sensor does not have a long-lasting component related to the lattice heating (like it was in the case of *p–n* junction, Fig. 3.7a) since the height of the band offset almost does not depend on temperature, whereas it is caused by a difference of the band gaps between GaAs and $Al_{0.2}Ga_{0.8}As$. The height of the band offset modelled in the 80–800 K temperature range is depicted in Fig. 3.22.

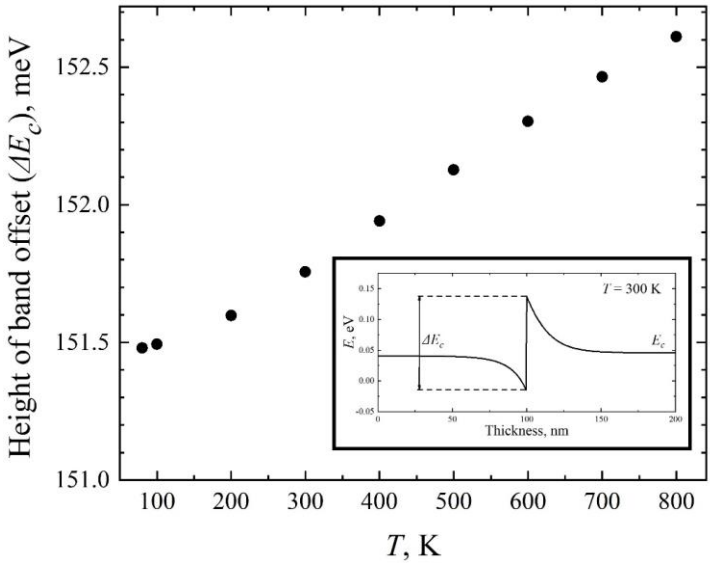

Fig. 3.22. Dependence of the height of $GaAs/Al_{0.2}Ga_{0.8}As$ potential barrier on temperature (created by the author)

The height difference of the band offset between 80 K and 300 K temperatures is only 0.3 meV. Furthermore, the increase in the band offset from 80 K to 800 K is merely 1 meV. This negligible change in the band offset allows to pass over the band modification of the developed sensor over a wide range of temperatures. The dependence of photocurrent peak value on laser intensity at 80 K and 300 K is depicted in Fig. 3.23.

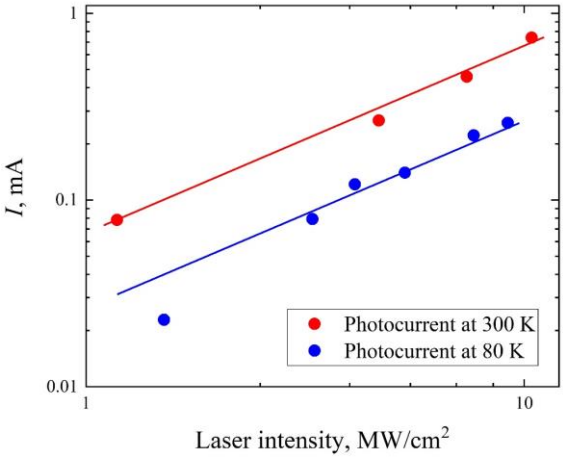

Fig. 3.23. Dependence of the photocurrent across the ratchet-based sensor on laser intensity at 80 K (blue dots) and 300 K (red dots). Solid lines are guides for the eye of linear dependence (created by the author)

The linear dependence at 300 K and 80 K is the evidence of the hot carrier nature of the induced current in the sensor, as mentioned in section 3.2 in the case of *p–n* junction (Fig. 3.6). In the entire range of intensity, the photocurrent stays smaller at cryogenic temperature. It is worth noting that in developed sensors, the linear dependence of output photocurrent on light intensity provides a convenient approach for plotting the fitting function. This appealing feature makes this device highly advantageous for a wide range of industrial applications.

As for perspectives, the magnitude of the signal can be increased by adding more layers of the graded gap $Al_xGa_{1-x}As$. The sensor may also detect radiation whose photon energy is higher than E_g. The part of the photon energy remaining after the generation of an electron–hole pair, i.e., $hv - E_g$, most probably would be used to heat primarily electrons since the effective mass of electrons in semiconductors is, as a rule, less than the effective mass of holes. In such a case, the polarity of the expected photoresponse induced by hot electrons coincides with the polarity of the photoresponse of the investigated case of $hv < E_g$, and the sensitivity of the sensor would be higher since the interband absorption in semiconductors is by several orders of magnitude stronger than the absorption of radiation by the free carriers. Moreover, the developed sensor, in contrast to narrow band gap semiconductors, does not require cryogenic temperatures, which makes it a promising candidate for application as an infrared detector.

3.7. Conclusions of the Third Chapter

1. The applied bias voltage influences the hot carrier and the classical photocurrent in illuminated GaAs and Si *p–n* junctions. The forward bias reduces the magnitude of the classical photocurrent. As for hot carrier photocurrent, the forward bias puts supportive conditions for the hot carrier current flow since the height of the barrier is getting lower. Since a single junction solar cell operating in a regime of the maximum output power is forwardly biased, the detrimental contribution of the hot carrier photocurrent to the net output signal is supported. It means that the hot carrier phenomenon needs to be considered and reduced or avoided at all.
2. Photovoltage across a *p–n* junction consists of three simultaneous components rising due to electron–hole pair generation, hot carrier effect and lattice heating. The first two are evident experimentally, while the lattice heating component results from the hot carrier effect. The proposed model of a *p–n* junction allows for revealing the individual contribution of each component to the net output signal. The magnitude of the net photovoltage is a mutual result of interaction between all three components. The individual contribution of each component depends on particular conditions, such as light wavelength, intensity, semiconductor band gap, temperature and bias voltage. The magnitude of the hot carrier component might even get stronger than the electron–hole pair generation-caused component under 51 kW/cm^2 excitation. This fact is explained by additional carrier heating by means of excess energy left after the interband absorption equals 0.9 eV.
3. The dependence of hot carrier photocurrent across a GaAs *p–n* junction on temperature sets on the influence of light intensity. The values of hot carrier photocurrent at 80 K are lower than at 300 K under 0.4 MW/cm^2 excitation since increasing the band gap and decreasing the absorption coefficient. At the higher light intensities, 2.1 MW/cm^2, the hot carrier photocurrent is higher at 80 K. This result is most probably caused by the increasing energy relaxation time of hot carriers.
4. A calculation method is proposed for the hot carrier temperature based on the *I–V* curves temperature coefficient. The method allows for the estimation of hot carrier temperature both at 300 K and 80 K ambient temperature. The absolute temperature change of the hot carriers was shown to be bigger at low temperatures than at room temperature. Explanation of stronger carrier heating at low temperatures could be grounded on increased hot carrier energy relaxation time with lower temperatures.

5. Modelling of the absorption spectra of solar radiation in typical *n*-type emitters of SCs reveals information about total absorption in these devices. The results reveal that both below and above-band gap photons have the potential to heat the free carriers. The portion of the below band gap region of the whole absorbed spectra can even reach up to 10% when the emitter layer has a thickness of 5 μm, and carrier density is 10^{20} cm^{-3}. It means that before the thermalisation and dissipation of their excess energy, the hot carriers can induce photocurrent, which has a detrimental influence on the solar cell operation. Hence, the theoretical efficiency limit would become lower if a direct negative impact of the hot carriers were considered, and this limit would come closer to the experimental solar cell efficiencies reached to date.
6. A graded gap layer positioned on the surface of a solar cell is a promising structure to reduce the negative HC effect on the total photosignal. The application of a porous layer onto a silicon solar cell increases the magnitude of the photovoltage. The surface porous Si layer decreases the surface reflectivity of the device. The obtained results show that the graded band gap of the porous Si extends the effective absorption of the short-wavelength region. In addition, the band offset between PSi and crystalline silicon expands the effective use of the long-wavelength range.
7. The ratchet-based $GaAs/Al_xGa_{1-x}As$ structure manifests itself as a promising novel type of infrared sensor operating based on the hot carrier effect. The band offsets between the heterolayers weakly depend on the temperature, which should make it possible to use the sensors in a wide temperature range. Higher photovoltage sensitivity can be achieved by increasing the number of active graded gap layers.
8. The hot carrier photocurrent dependence on the light intensity at cryogenic temperature in the *p–n* junction should be researched in more detail because of its ambiguous behaviour at different temperatures and light intensities.
9. To get the research closer to natural solar illumination conditions, ways should be searched to detect the hot carrier effect in a *p–n* junction under continuous wave illumination.

General Conclusions

1. The division model for the total photovoltage across a solar cell reveals that the output signal consists of three components caused by electron–hole pair generation, carrier heating, and lattice heating. The model shows the individual impact of the hot carrier phenomenon on the net signal. It is proven that the hot carriers give rise to the signal before they distribute their extra energy to the lattice and heat it. This result evidences that the hot carrier effect has to be accounted for as a new type of intrinsic loss in solar cells.
2. Calculated hot carrier distribution statistics with estimated carriers' temperature show that the hot carrier photocurrent across biased +0.7 V GaAs *p–n* junction has a recombination mechanism because the heated free carriers occupy the energy states that are much below the biased but still high potential barrier of the junction
3. In addition to the above-band gap absorption, the absorption of photons having energy lower than the band gap has the potential to heat the free carriers. This fact calls for revising the Shockley–Queisser limit by considering the below-band gap absorption.

4. The ratchet-based semiconductor-graded gap structure shows a potential to be used as an infrared radiation sensor operating on the base of the hot carrier effect at room temperature. The developed sensor has linear output photosignal dependence on the light intensity, which is convenient for device calibration.

References

Adachi, S. (1998). Optical dispersion relations for GaP, GaAs, GaSb, InP, InAs, InSb, $Al_xGa_{1-x}As$, and $In_{1-x}Ga_xAs_yP_{1-y}$. *Journal of Applied Physics*, *66*(12), 6030. https://doi.org/10.1063/1.343580

Adams, J. G. J., Elder, W., Stavrinou, P. N., Roberts, J. S., Gonzalez, M., Tischler, J. G., Walters, R. J., Abell, J., Vurgaftman, I., Meyer, J. R., Jenkins, P., Barnham, K. W. J., & Ekins-Daukes, N. J. (2010). Experimental measurement of restricted radiative emission in quantum well solar cells. *2010 35th IEEE Photovoltaic Specialists Conference*, 000001–000005. https://doi.org/10.1109/PVSC.2010.5614119

Ahmed, I., Shi, L., Pasanen, H., Vivo, P., Maity, P., Hatamvand, M., & Zhan, Y. (2021). There is plenty of room at the top: generation of hot charge carriers and their applications in perovskite and other semiconductor-based optoelectronic devices. *Light: Science & Applications 2021 10:1*, *10*(1), 1–28. https://doi.org/10.1038/s41377-021-00609-3

Aissat, A., Arbouz, H., & Vilcot, J. P. (2018). Optimization and improvement of a front graded bandgap CuInGaSe2 solar cell. *Solar Energy Materials and Solar Cells*, *180*, 381–385. https://doi.org/10.1016/J.SOLMAT.2017.09.017

Akinoglu, B. G., Tuncel, B., & Badescu, V. (2021). Beyond 3rd generation solar cells and the full spectrum project. Recent advances and new emerging solar cells. *Sustainable Energy Technologies and Assessments*, *46*, 101287. https://doi.org/10.1016/J.SETA.2021.101287

Ananthakumar, S., Kumar, J. R., & Babu, S. M. (2019). *Third-Generation Solar Cells: Concept, Materials and Performance - An Overview*. 305–339. https://doi.org/10.1007/978-3-030-04474-9_7

Araújo, G. L., & Martí, A. (1994). Absolute limiting efficiencies for photovoltaic energy conversion. *Solar Energy Materials and Solar Cells*, *33*(2), 213–240. https://doi.org/10.1016/0927-0248(94)90209-7

Ašmontas, S. (1984). *Electrogradient Phenomena in Semiconductors* (J. Požela, Ed.; Vol. 5). Vilnius, Mokslas.

Ašmontas, S., Gradauskas, J., Seliuta, D., & Šilėnas, A. (1997). *Photoemf of hot carriers in nonuniform GaAs* (E. A. Silinsh, A. Medvids, A. R. Lusis, & A. O. Ozols (eds.); pp. 104–109). https://doi.org/10.1117/12.266815

Ašmontas, S., Gradauskas, J., Seliuta, D., Šilėnas, A., & Širmulis, E. (1996). New GaAs infrared detector. *Gallium Arsenide Application Symposium GaAs96*, 1–4. https://www.researchgate.net/publication/44706692

Ašmontas, S., Gradauskas, J., Seliuta, D., & Širmulis, E. (2001). Photoelectrical properties of nonuniform semiconductor under infrared laser radiation. *Nonresonant Laser-Matter Interaction (NLMI-10), 4423*, 18–27. https://doi.org/10.1117/12.431223

Ašmontas, S., Gradauskas, J., Seliuta, D., Sužiedėlis, A., Širmulis, E., Tetyorkin, V. V., Urbelis, A., & Alusis, G. (2003). Influence of free carrier heating on IR light detection in narrow-gap semiconductors. In *proc. of conference of Advanced Optical Devices, Technologies, and Medical Applications* 243–247. https://doi.org/10.1117/12.517029

Barnham, K. W. J., & Duggan, G. (1998). A new approach to high-efficiency multi-band-gap solar cells. *Journal of Applied Physics*, *67*(7), 3493. https://doi.org/10.1063/1.345339

Cavassilas, N., Makhfudz, I., Daré, A.-M., Lannoo, M., Dangoisse, G., Bescond, M., & Michelini, F. (2022). Theoretical Demonstration of Hot-Carrier Operation in an Ultrathin Solar Cell. *Physical Review Applied*, *17*(6), 064001. https://doi.org/10.1103/PhysRevApplied.17.064001

Chung, S., Shrestha, S., Wen, X., Feng, Y., Gupta, N., Xia, H., Yu, P., Tang, J., & Conibeer, G. (2016). Hafnium nitride for hot carrier solar cells. *Solar Energy Materials and Solar Cells*, *144*, 781–786. https://doi.org/10.1016/J.SOLMAT.2014.10.011

Conibeer, G. (2007). Third-generation photovoltaics. *Materials Today*, *10*(11), 42–50. https://doi.org/10.1016/S1369-7021(07)70278-X

Conibeer, G., Shrestha, S., Huang, S., Patterson, R., Xia, H., Feng, Y., Zhang, P., Gupta, N., Tayebjee, M., Smyth, S., Liao, Y., Zhang, Z., Chung, S., Lin, S., Wang, P., & Dai, X. (2014). Hot carrier solar cell absorbers: materials, mechanisms and nanostructures. *Next Generation Technologies for Solar Energy Conversion V*, *9178*, 917802. https://doi.org/10.1117/12.2067926

Dargys, A., & Kundrotas, J. (1994). Handbook on the physical properties of Ge, Si, GaAs and InP by A Dargys and J Kundrotas. In *Physics-Uspekhi* (1st ed., Issue 7). Mokslo ir enciklopedijų leidykla. https://doi.org/10.1070/PU1996V039N07ABEH001526

De Vos, A., Landsberg, P. T., Baruch, P., & Parrott, J. E. (1993). Entropy fluxes, endoreversibility, and solar energy conversion. *Journal of Applied Physics*, *74*(6), 3631–3637. https://doi.org/10.1063/1.354503

Dupré, O., Niesen, B., De Wolf, S., & Ballif, C. (2018). Field Performance versus Standard Test Condition Efficiency of Tandem Solar Cells and the Singular Case of Perovskites/Silicon Devices. *Journal of Physical Chemistry Letters*, *9*(2), 446–458. https://doi.org/10.1021/ACS.JPCLETT.7B02277/ASSET/IMAGES/LARGE/JZ-2017-02277Q_0015.JPEG

Ehrler, B., Alarcón-Lladó, E., Tabernig, S. W., Veeken, T., Garnett, E. C., & Polman, A. (2020). Photovoltaics reaching for the shockley-queisser limit. *ACS Energy Letters*, *5*(9), 3029–3033. https://doi.org/10.1021/ACSENERGYLETT.0C01790

Geisz, J. F., France, R. M., Schulte, K. L., Steiner, M. A., Norman, A. G., Guthrey, H. L., Young, M. R., Song, T., & Moriarty, T. (2020). Six-junction III–V solar cells with 47.1% conversion efficiency under 143 Suns concentration. *Nature Energy 2020 5:4*, *5*(4), 326–335. https://doi.org/10.1038/s41560-020-0598-5

Glover, G. H. (2003). Study of electron energy relaxation times in GaAs and InP. *Journal of Applied Physics*, *44*(3), 1295. https://doi.org/10.1063/1.1662343

Green, M. A. (1982). Accuracy of analytical expressions for solar cell fill factors. *Sol. Cells; (Switzerland)*, *7:3*(3), 337–340. https://doi.org/10.1016/0379-6787(82)90057-6

Green, M. A. (2005). Silicon photovoltaic modules: a brief history of the first 50 years. *Progress in Photovoltaics: Research and Applications*, *13*(5), 447–455. https://doi.org/10.1002/pip.612

Green, M. A. (2008). Self-consistent optical parameters of intrinsic silicon at 300 K including temperature coefficients. *Solar Energy Materials and Solar Cells*, *92*(11), 1305–1310. https://doi.org/10.1016/J.SOLMAT.2008.06.009

Green, M. A. (2015). Forty Years of Photovoltaic Research at UNSW. *Journal and Proceedings of the Royal Society of New South Wales*, *148*, 2–14.

Grigor′ev, B. A., Nuzhnyĭ, V. A., & Shibanov, B. V. (1971). *Tables for calculating non-stationary temperatures of flat bodies when heated by radiation*. Nauka.

Guo, Z., Wan, Y., Yang, M., Snaider, J., Zhu, K., & Huang, L. (2017). Long-range hot-carrier transport in hybrid perovskites visualized by ultrafast microscopy. *Science (New York, N.Y.)*, *356*(6333), 59–62. https://doi.org/10.1126/SCIENCE.AAM7744

Henry, C. H. (2008). Limiting efficiencies of ideal single and multiple energy gap terrestrial solar cells. *Journal of Applied Physics*, *51*(8), 4494. https://doi.org/10.1063/1.328272

Hirst, L. C., & Ekins-Daukes, N. J. (2011). Fundamental losses in solar cells. *Progress in Photovoltaics: Research and Applications*, *19*(3), 286–293. https://doi.org/10.1002/PIP.1024

Ikeri, H. I., Onyia, A. I., & Asogwa, P. U. (2019). Investigation Of Optical Characteristics Of Semiconductor Quantum Dots For Multi Junction Solar Cells Applications. *INTERNATIONAL JOURNAL OF SCIENTIFIC & TECHNOLOGY RESEARCH*, *8*(10).

Kang, H. (2021). Crystalline Silicon vs. Amorphous Silicon: the Significance of Structural Differences in Photovoltaic Applications. *IOP Conference Series: Earth and Environmental Science*, *726*(1), 012001. https://doi.org/10.1088/1755-1315/726/1/012001

Kostylyov, V., Sachenko, A., Vlasiuk, V., Sokolovskyi, I., Kobylianska, S., Torchyniuk, P., V'yunov, O., & Belous, A. (2021). Synthesis and Investigation of the Properties of Organic-Inorganic Perovskite Films with Non-Contact Methods. *Ukrainian Journal of Physics*, *66*(5), 429. https://doi.org/10.15407/ujpe66.5.429

Landis, G. A., Belgiovane, D. J., & Scheiman, D. A. (2011). Temperature coefficient of multijunction space solar cells as a function of concentration. *Conference Record of the IEEE Photovoltaic Specialists Conference*, 001583–001588. https://doi.org/10.1109/PVSC.2011.6186260

Lee, T. D., & Ebong, A. U. (2017). A review of thin film solar cell technologies and challenges. *Renewable and Sustainable Energy Reviews*, *70*, 1286–1297. https://doi.org/10.1016/J.RSER.2016.12.028

Liu, N., Wang, L., Xu, F., Wu, J., Song, T., & Chen, Q. (2020). Recent Progress in Developing Monolithic Perovskite/Si Tandem Solar Cells. *Frontiers in Chemistry*, *8*, 1120. https://doi.org/10.3389/FCHEM.2020.603375/BIBTEX

Markvart, T. (2007). Thermodynamics of losses in photovoltaic conversion. *Applied Physics Letters*, *91*(6), 064102. https://doi.org/10.1063/1.2766857

Medvid, A. (2010). Nano-Cones Formed on a Surface of Semiconductors by Laser Radiation: Technology, Model and Properties. In *Nanowires Science and Technology*. InTech. https://doi.org/10.5772/39493

Min, H., Lee, D. Y., Kim, J., Kim, G., Lee, K. S., Kim, J., Paik, M. J., Kim, Y. K., Kim, K. S., Kim, M. G., Shin, T. J., & Il Seok, S. (2021). Perovskite solar cells with atomically coherent interlayers on SnO_2 electrodes. *Nature*, *598*(7881), 444–450. https://doi.org/10.1038/s41586-021-03964-8

Minnaert, B., & Veelaert, P. (2012). Guidelines for the Bandgap Combinations and Absorption Windows for Organic Tandem and Triple-Junction Solar Cells. *Materials*, *5*(10), 1933. https://doi.org/10.3390/MA5101933

Mohammad Bagher, A., Vahid Mirzaei, M. A., & Mohsen, M. (2015). Types of Solar Cells and Application. *American Journal of Optics and Photonics*, *3*(5), 94. https://doi.org/10.11648/j.ajop.20150305.17

Morgan, T. N. (1959). The mobility of electrons heated by microwave fields in n-type germanium. *Journal of Physics and Chemistry of Solids*, *8*, 245–249. https://doi.org/10.1016/0022-3697(59)90327-0

Myers, D. R., & Emery, K. (2002). Revising and Validating Spectral Irradiance Reference Standards for Photovoltaic Performance: Preprint. *ASES/ASME Solar 2002 Conference* , 1–13. http://www.osti.gov/bridge

Nguyen, D.-T., Lombez, L., Gibelli, F., Boyer-Richard, S., Le Corre, A., Durand, O., & Guillemoles, J.-F. (2018). Quantitative experimental assessment of hot carrier-enhanced solar cells at room temperature. *Nature Energy*, *3*(3), 236–242. https://doi.org/10.1038/s41560-018-0106-3

Polman, A., & Atwater, H. A. (2012). Photonic design principles for ultrahigh-efficiency photovoltaics. *Nature Materials 2012 11:3*, *11*(3), 174–177. https://doi.org/10.1038/nmat3263

Požela, J. (1993). Hot-Electron Transistors. In G. Vebrene (Ed.), *Physics of High-Speed Transistors* (1st ed., pp. 197–236). Springer US. https://doi.org/10.1007/978-1-4899-1242-8_7

Rajagopal, K. (2008). *Textbook of Engineering Physics, Part I* (1st ed.). PHI Learning Pvt. Ltd. New Delhi.

Rodziewicz, T., Rajfur, M., Teneta, J., Świsłowski, P., & Wacławek, M. (2021). Modelling and analysis of the influence of solar spectrum on the efficiency of photovoltaic modules. *Energy Reports*, *7*, 565–574. https://doi.org/10.1016/J.EGYR.2021.01.013

Rogalski, A. (2005). HgCdTe infrared detector material: history, status and outlook. *Reports on Progress in Physics*, *68*(10), 2267. https://doi.org/10.1088/0034-4885/68/10/R01

Ross, R. T., & Nozik, A. J. (1998). Efficiency of hot-carrier solar energy converters. *Journal of Applied Physics*, *53*(5), 3813. https://doi.org/10.1063/1.331124

Rühle, S. (2016). Tabulated values of the Shockley–Queisser limit for single junction solar cells. *Solar Energy*, *130*, 139–147. https://doi.org/10.1016/J.SOLENER.2016.02.015

Sah, C. T., Noyce, R. N., & Shockley, W. (1957). Carrier Generation and Recombination in P-N Junctions and P-N Junction Characteristics. *Proceedings of the IRE*, *45*(9), 1228–1243. https://doi.org/10.1109/JRPROC.1957.278528

Sasaki, M., Negishi, H., & Inoue, M. (1998). Pulsed laser-induced transient thermoelectric effects in silicon crystals. *Journal of Applied Physics*, *59*(3), 796. https://doi.org/10.1063/1.336600

Schaffner, J. S., & Shea, R. F. (1955). The Variation of the Forward Characteristics of Junction Diodes with Temperature. *Proceedings of the Institute of Radio Engineers*, 101. https://ieeexplore.ieee.org/stamp/stamp.jsp?tp=&arnumber=4055239

Schnier, T., Emara, J., Olthof, S., & Meerholz, K. (2017). Influence of hybrid perovskite fabrication methods on film formation, electronic structure, and solar cell performance. *Journal of Visualized Experiments : JoVE*, *2017*(120). https://doi.org/10.3791/55084

Shockley, W., & Queisser, H. J. (1961). Detailed balance limit of efficiency of p-n junction solar cells. *J. Appl. Phys.*, *32*(3), 510–519. https://doi.org/10.1063/1.1736034

Šilėnas, A., Steikuniene, A., & Steikunas, G. (2014). Formation technology of graded-Gap $Al_xGa_{1-x}As$ solar cell structure separated from GaAs substrate. *Materials Science*, *20*(2), 147–149. https://doi.org/10.5755/J01.MS.20.2.6327

Sze, S. M., & Ng, K. K. (2006). *Physics of Semiconductor Devices* (2nd ed.). Wiley. https://doi.org/10.1002/0470068329

Tanaka, T., Nakano, Y., & Kasai, S. (2013). GaAs-Based Nanowire Devices with Multiple Asymmetric Gates for Electrical Brownian Ratchets. *Japanese Journal of Applied Physics*, *52*(6S), 06GE07. https://doi.org/10.7567/JJAP.52.06GE07

Umeno, M., Sugito, Y., Jimbo, T., Hattori, H., & Amemiya, Y. (1978). Hot photo-carrier and hot electron effects in p-n junctions. *Solid-State Electronics*, *21*(1), 191–195. https://doi.org/10.1016/0038-1101(78)90137-5

van Sark, W. G. J. H. M., Meijerink, A., & Schropp, R. E. I. (2012). Solar Spectrum Conversion for Photovoltaics Using Nanoparticles. In *Third Generation Photovoltaics*. InTech. https://doi.org/10.5772/39213

Wasiak, M., Walczak, J., Motyka, M., Janiak, F., Trajnerowicz, A., & Jasik, A. (2017). Below-band-gap absorption in undoped GaAs at elevated temperatures. *Optical Materials*, *64*, 137–141. https://doi.org/10.1016/j.optmat.2016.11.028

Welser, R. E., Polly, S. J., Kacharia, M., Fedorenko, A., Sood, A. K., & Hubbard, S. M. (2019). Design and Demonstration of High-Efficiency Quantum Well Solar Cells Employing Thin Strained Superlattices. *Scientific Reports*, *9*(1), 13955. https://doi.org/10.1038/s41598-019-50321-x

Won, W., Yang, Y., Chang, T. G., Song, I. H., Cho, Y. S., Heo, J., Jeon, W. G., Lee, J. W., & Kim, J. K. (2009). *Signals and Systems with MatLab* (2009th ed.). Springer.

Yamaguchi, M., Takamoto, T., & Araki, K. (2006). Super high-efficiency multi-junction and concentrator solar cells. *Solar Energy Materials and Solar Cells*, *90*(18–19), 3068–3077. https://doi.org/10.1016/J.SOLMAT.2006.06.028

Yang, Y., Ostrowski, D. P., France, R. M., Zhu, K., van de Lagemaat, J., Luther, J. M., & Beard, M. C. (2016). Observation of a hot-phonon bottleneck in lead-iodide perovskites. *Nature Photonics*, *10*(1), 53–59. https://doi.org/10.1038/nphoton.2015.213

Yin, J., Maity, P., Naphade, R., Cheng, B., He, J. H., Bakr, O. M., Brédas, J. L., & Mohammed, O. F. (2019). Tuning Hot Carrier Cooling Dynamics by Dielectric Confinement in Two-Dimensional Hybrid Perovskite Crystals. *ACS Nano*, *13*(11), 12621–12629. https://doi.org/10.1021/ACSNANO.9B04085/ASSET/IMAGES/MEDIUM/NN9B04085_M006.GIF

Zanatta, A. R. (2019). Revisiting the optical bandgap of semiconductors and the proposal of a unified methodology to its determination. *Scientific Reports*, *9*(1), 11225. https://doi.org/10.1038/s41598-019-47670-y

Zekry, A., Yahyaoui, I., & Tadeo, F. (2019). Generic Analytical Models for Organic and Perovskite Solar Cells. *2019 10th International Renewable Energy Congress, IREC 2019*. https://doi.org/10.1109/IREC.2019.8754574

Zhang, Y., Jia, X., Liu, S., Zhang, B., Lin, K., Zhang, J., & Conibeer, G. (2021). A review on thermalization mechanisms and prospect absorber materials for the hot carrier solar cells. *Solar Energy Materials and Solar Cells*, *225*, 111073. https://doi.org/10.1016/J.SOLMAT.2021.111073

Zhou, J., You, Z., Xu, W., Su, Z., Qiu, Y., Gao, L., Yin, C., & Lan, L. (2019). Microwave irradiation directly excites semiconductor catalyst to produce electric current or electron-holes pairs. *Scientific Reports*, *9*(1), 5470. https://doi.org/10.1038/s41598-019-41002-w

List of Scientific Publications by the Author on the Topic of the Dissertation

Papers in the Reviewed Scientific Journals

Masalskyi, O., & Gradauskas, J. (2022). Pre-themalizational effect of hot carriers on photovoltage formation in a solar cell. *Ukrainian Journal of Physical Optics 23*(3): 117–125. https://doi.org/10.3116/16091833/23/3/117/2022

Gradauskas, J., Ašmontas, S., Sužiedelis, A., Šilenas, A., Vaicikauskas, V., Cerškus, A., Širmulis, E., Žalys, O., & Masalskyi, O. (2020). Influence of hot carrier and thermal components on photovoltage formation across the *p-n* junction. *MDPI Applied Science 10*: 1–8. https://doi.org/10.3390/app10217483

Ašmontas, S., Fedorenko, L., Vlasiuk, V., Gorbanyuk, T., Kostylyov, V., Lytovchenko, V., Gradauskas, J., Sužiedėlis, A., Širmulis, E., Žalys O., & Masalskyi, O. (2020). Suppression of hot carriers by nanoporous silicon for improved operation of a solar cell. *Ukrainian Journal of Physical Optics 21*(4): 207–217. https://doi.org/10.3116/16091833/21/4/207/2020

Ašmontas, S., Cerškus, A., Gradauskas, J., Masalskyi, O., Šilenas, A., Sužiedelis, A., & Žalys, O. (2020). Modelling of photoresponse components induced by laser pulse across

a *p-n* junction. In *Proc. of 6th International Conference on Sensors and Electronic Instrumentation Advances* Porto, Portugal, 2020, 21–23. https://www.sensorsportal.com/SEIA_2021/SEIA_2020_Proceedings_Contents.pdf

Papers in Other Editions

Ašmontas, S., Gradauskas, J., Sužiedėlis, A., Šilėnas, A., Čerškus, A., Vaičikauskas, V., Masalskyi, O., & Žalys, O. A. (2020). Influence of thermoelectricity on conversion efficiency of solar cells. In *Proc. of forum XVIII International Forum on Thermoelectricity in the following lines: theory of thermoelectricity metrology in thermoelectricity, thermoelectric material science, thermoelectric devices and instruments*, Chernivtsi, Ukraine, 2020, 23–24. https://vb.vgtu.lt/object/elaba:146766291/

Gradauskas, J., Ašmontas, S., Sužiedėlis, A., Šilėnas, A., Čerškus, A., Žalys, O. A., & Masalskyi, O. (2021). Hot carrier evidence in a solar cell. In *Proc. of conference Open Readings 2021: 64th international conference for students of physics and natural sciences*, Vilnius, Lithuania, 289. https://openreadings.eu/wp-content/abstracts/abstract-2021.pdf

Gradauskas, J., Ašmontas, S., Sužiedėlis, A., Šilėnas, A., Čerškus, A., Vaičikauskas, V., Masalskyi, O., & Žalys, O. A. (2020). Three components of photovoltage simultaneously induced across GaAs p-n junction. In *Proc. of conference 17th Advanced properties and processes in optoelectronics materials and systems*, Vilnius, Lithuania, 54. https://apropos.ftmc.lt/wp-content/uploads/2021/01/Abstract-book-Apropos-17-2020.pdf

Gradauskas, J., Ašmontas, S., Sužiedėlis, A., Šilėnas, A., Čerškus, A., Vaičikauskas, V., Žalys, O. A., & Masalskyi, O. (2020). Hot carrier evidence in a solar cell. In *Proc. of conference 37th European Photovoltaic Solar Energy Conference and Exhibition*, Virtual, 1–2. https://userarea.eupvsec.org/proceedings/EU-PVSEC-2020/1BV.4.2/, https://talpykla.elaba.lt/elaba-fedora/objects/elaba:147805520/datastreams/MAIN/content

Masalskyi, O., Gradauskas, J., Ašmontas, S., Sužiedėlis, A., Šilėnas, A., Čerškus, A., Rodin, A., & Zharchenko, I. (2022). Direct hot carrier impact on photovoltage of a solar cell. In *Proc. of symposium 23rd Sede Boqer Symposium on Solar Electricity Production*. Be'er Sheva, Israel, 1. https://vb.vgtu.lt/object/elaba:141914406/

Masalskyi, O., Gradauskas, J., & Zharchenko, I. (2022). Photovoltage formation across GaAs p-n junction under intense laser light. In *Proc. of international young scientist conference 18th Developments in optics and communications*. Riga, Latvia, 21–22. http://www.docriga.lv/assets/6260f21e00dd6/Abstract%20book%20DOC%202022.pdf

Masalskyi, O., & Gradauskas, J. (2021a). Hot carriers in a single junction solar cell. In *Proc. of international young scientist conference 17th Developments in optics and communications – 2021*, Riga, Latvia, 48. http://www.docriga.lv/assets/607588eeac53e/DOC%202021%20Abstract%20Book.pdf

Masalskyi, O., & Gradauskas, J. (2021b). Investigation of hot carrier phenomenon in GaAs p-n junction. In *Proc. of conference Lashkaryov's readings*. Kyiv, Ukraine, 76. https://drive.google.com/file/d/13RO-UyYfF7GKl-Rk6puz3kngzYEkUDF2/view

Masalskyi, O., Gradauskas, J., Ašmontas, S., Sužiedėlis, A., Šilėnas, A., Čerškus, A., Rodin, A., & Zharchenko, I. (2021). Direct impact of hot carriers on the operation of a p-n junction solar cell. In *Proc. of conference 44-oji Lietuvos nacionalinė fizikos konferencija*, Vilnius, Lithuania, 206.

http://lnfk.ftmc.lt/wp-content/uploads/2021/11/LNFK-44-pranesimu-medziaga-2021-spalio-6-8-Vilnius.pdf

Masalskyi, O., Gradauskas, J., Ašmontas, S., Sužiedėlis, A., Šilėnas, A., Čerškus, A., Rodin, A. (2021). Direct unfavorable impact of hot carriers on the operation of a single junction solar cell. In *Proc. of conference 38th European Photovoltaic Solar Energy Conference and Exhibition*, Virtual, 1–2. https://userarea.eupvsec.org/proceedings/EU-PVSEC-2021/1BV.3.1/

Summary in Lithuanian

Įvadas

Problemos formulavimas

Galimybės padidinti saulės elementų (SE) efektyvumą yra aktyviai tiriamos pastaraisiais dešimtmečiais. Vienos *p* ir *n* sandūros saulės elementas vis dar nepasiekė teorinės Shockley–Queisser efektyvumo 33 % ribos daugiausia dėl vadinamųjų vidinių (savųjų) nuostolių. Apie 80 % vidinių nuostolių yra dėl neabsorbuojamų fotonų (anot Shockley–Queisser teorijos), kurių energija yra mažesnė už draudžiamosios energijos tarpą, ir dėl termalizacijos proceso (Hirst & Ekins-Daukes, 2011). Tačiau mažos energijos fotonai gali būti sugerti laisvaisiais krūvininkais ir tokiu būdu juos kaitinti. Termalizacijos nuostolius sukelia fotonų, kurių energija didesnė už draudžiamosios energijos tarpą, sugertis. Energijos perteklius, t. y. skirtumas tarp fotono energijos ir tarpo pločio, taip pat kaitina krūvininkus, po to vyksta kristalinės gardelės kaitimas.

Nauji šiuolaikiniai saulės elementų dariniai (trečiosios kartos SE), pavyzdžiui, tokie kaip struktūros su kvantiniais šuliniais ar kelių sandūrų SE, leidžia sumažinti spektrinius nuostolius bei efektyviai panaudoti fotonų energijos perteklių. Pavyzdžiui, karštųjų krūvininkų saulės elementai efektyviai panaudoja tokių krūvininkų energiją ir tokiu būdu gali pasiekti 66 % efektyvumą, taip viršydami teorinę Shockley–Queisser ribą (Ross & Nozik, 1998). Deja, šių SE modelis yra dar toli nuo praktinio įgyvendinimo.

Darbo aktualumas

Trečiosios kartos saulės elementų koncepcijos yra perspektyvūs sprendimai, leidžiantys efektyviau panaudoti saulės spektrą, o kartu ir padidinti SE efektyvumą (Akinoglu et al., 2021). Deja, šių elementų kaina yra daug didesnė nei pirmosios ar antrosios kartos pramoninių SE.

Įprastuose plačiausiai taikomuose saulės elementuose didelė sugerto saulės spektro dalis (iki 55 %) potencialiai gali būti panaudota krūvininkams kaitinti (Masalskyi & Gradauskas, 2022). Todėl išsamesni karštųjų krūvininkų reiškinių tyrimai vienos sandūros saulės elemente gali atverti kelius, leidžiančius padidinti pramoninių saulės elementų efektyvumą. Be to, neišvengiamas karštųjų krūvininkų reiškinys gali būti svari priežastis, dėl kurios vertėtų peržiūrėti vienos sandūros saulės elemento Shockley–Queisser ribą. Galiausiai, spinduliuotės jutikliai, veikiantys karštųjų krūvininkų reiškinio pagrindu, turi didelį potencialą elektromagnetinės spinduliuotės detektavimo sprendimuose.

Tyrimo objektas

Tyrimo objektas yra karštųjų krūvininkų reiškinys *p* ir *n* dioduose ir jo taikymas elektromagnetinei spinduliuotei detektuoti puslaidininkiais dariniais.

Darbo tikslas

Ištirti karštųjų krūvininkų reiškinio ypatumus ir poveikį vienos *p* ir *n* sandūros saulės elemento veikimui, taip pat sukurti elektromagnetinės spinduliuotės jutiklį, veikiantį karštųjų krūvininkų reiškinio pagrindu.

Darbo uždaviniai

Siekiant darbo tikslo, suformuluoti šie uždaviniai:

1. Sukurti modelį, leidžiantį apibrėžti tiesioginį poveikį ir analizuoti karštųjų nešiklių poveikį saulės elemento išėjimo signalui.
2. Simuliuoti saulės elementų sugerties spektrą atsižvelgiant į krūvininkų kaitinimo procesą.
3. Atskleisti būdus, leidžiančius sumažinti karštųjų krūvininkų reiškinio įtaką saulės elementuose.
4. Sukurti darinį ir pagaminti infraraudonosios spinduliuotės jutiklį, veikiantį karštųjų krūvininkų reiškinio pagrindu.

Tyrimų metodika

Objektui tirti buvo pasirinktos šios tyrimo metodikos: eksperimentinė, kiekybinė ir analitinė. Siekiant išsamesnio supratimo apie metodikas, leidžiančias išvengti, įvertinti ir slopinti spektrinius ir termalizacijos nuostolius saulės elementuose, buvo išanalizuoti šiuolaikinių SE tipai. Taip pat atskleistas karštųjų krūvininkų fotoatsako kilimas *p* ir *n* sandūroje. Pagamintieji bandiniai buvo tiriami fotosrovės režimu. Sukurtas modelis padėjo pažvelgti į fotoatsako formavimosi procesą *p* ir *n* sandūroje. Modelis taip pat leido atskirti saulės elemento signalo komponentus. Tirtieji dariniai buvo apšviečiami neodimiu

legiruoto itrio aliuminio granato lazerio (bangos ilgis 1,064 μm) ir neodimiu legiruotu itrio ortovanadato lazerio (bangos ilgis 1,342 μm) šviesos impulsais. Elektriniai signalai buvo matuojami Agilent Technologies DSO6102A osciloskopu. Tirtieji GaAs *p* ir *n* fotodiodai ir $GaAs/Al_xGa_{1-x}As$ jutiklis buvo auginami skystosios fazės epitaksijos būdu, o silicio *p* ir *n* sandūros paimtos iš pramoninių silicio saulės elementų (SoliTek, Vilnius, Lietuva).

Darbo mokslinis naujumas

Disertacijos mokslinės naujovės yra šios:

1. Buvo sukurtas modelis, leidžiantis atskirti saulės elemento fotoatsako komponentus, sąlygotus elektronų-skylių generavimo, krūvininkų kaitimo ir gardelės kaitimo. Tai leido įvertinti tiesioginį karštųjų krūvininkų efekto poveikį ir išsamiau išnagrinėti fotoatsako formavimosi procesą.
2. Sumodeliuotas vienos sandūros saulės elemento sugerties spektras. Tai padėjo apibrėžti saulės spektro dalį, potencialiai galinčią kaitinti laisvuosius krūvininkus.
3. Pasiūlyta karštųjų krūvininkų temperatūros apskaičiavimo metodika panaudojant *p-n* sandūros voltamperinės charakteristikos įtampos kritimo koeficiento priklausomybę nuo temperatūros.
4. Nustatyta neigiama karštųjų krūvininkų įtaka pramoninio vienos sandūros saulės elemento išėjimo signalui.
5. Sukurtas reketinis $GaAs/Al_xGa_{1-x}As$ elektromagnetinės spinduliuotės jutiklis, veikiantis karštųjų krūvininkų reiškinio pagrindu.

Darbo rezultatų praktinė reikšmė

Gauti rezultatai turi didelę praktinę reikšmę.

Saulės elemento signalo komponentų atskyrimo modelis leidžia įvertinti tiesioginę karštųjų krūvininkų įtaką bendrajam fotoatsakui. Nustatytos sąlygos geriausiam saulės elemento veikimo režimui.

Karštųjų krūvininkų įtakos pramoniniams saulės elementams atskleidimas yra rimta priežastis, skatinanti peržiūrėti maksimalų teorinį vienos sandūros saulės elemento efektyvumą.

Varizoninio paviršiaus sluoksnio suformavimas gali prislopinti karštųjų krūvininkų įtaką ir taip praplėsti efektyvų saulės elemento sugerties spektrą.

Reketinis $GaAs/Al_xGa_{1-x}As$ jutiklis, veikiantis karštųjų krūvininkų reiškinio pagrindu, yra perspektyvus infraraudonųjų spindulių detektavimo įtaisas.

Ginamieji teiginiai

Remiantis pasiektais rezultatais, šie teiginiai išreiškiami kaip gintinos hipotezės:

1. Bendra fotosrovė per *p* ir *n* sandūrą atsiranda dėl vienu metu vykstančių procesų, sąlygotų elektronų-skylių porų generavimo, gardelės kaitimo ir laisvųjų krūvininkų kaitimo; pastarasis daro neigiamą poveikį vienos sandūros saulės elemento veikimui, kadangi karštųjų krūvininkų fotosrovės kryptis yra visada priešinga klasikinei krūvininkų generacijos indukuotai fotosrovei.

2. Karštųjų krūvininkų fotosrovė GaAs *p* ir *n* sandūroje 300 K temperatūroje turi rekombinacinę prigimtį esant iki +0,7 V priešįtampiui bei karštųjų krūvininkų 454 K temperatūrai.
3. Fotonai, kurių energija yra mažesnė už draudžiamosios energijos tarpą, kaitina laisvuosius krūvininkus ir sudaro iki 10 % visos sugertos saulės spektro energijos dalies Si ir GaAs vienos sandūros saulės elemento 5 μm storio emiterio paviršiaus sluoksnyje; ir šis efektas yra stipresnis stipriau legiruotuose ir storesniuose emiterio sluoksniuose.
4. Sukurtas reketinis $GaAs/Al_xGa_{1-x}As$ varizoninis darinys, veikiantis karštųjų krūvininkų reiškinio pagrindu, detektuoja infraraudonąją 1,064 μm bangos ilgio spinduliuotę $2 \times 10^{-8}\ \frac{A}{W}$ jautriu kambario temperatūroje.

Darbo rezultatų aprobavimas

Darbo rezultatai paskelbti 14 mokslinių publikacijų. Trys iš jų išspausdinti recenzuojamuose moksliniuose žurnaluose, įtrauktuose į *Clarivate Analytics Web of Science* duomenų bazės sąrašą ir turinčiuose citavimo rodiklį, vienas konferencijos pranešimuose, 10 iš jų – recenzuojamos publikacijos (santraukos) kituose recenzuojamose mokslo žurnaluose.

Tyrimo rezultatai pristatyti aštuoniose tarptautinėse, regioninėse ir vietinėse mokslinėse konferencijose ir simpoziumuose:

- 18-oji Tarptautinė jaunųjų mokslininkų konferencija *Developments in Optics and Communications* (DOC 2022), Ryga, Latvija.
- Jaunųjų mokslininkų konferencija *Puslaidininkių fizikos klausimais* (Laškariovo skaitymai 2021 m.), Kijevas, Ukraina.
- 6-oji tarptautinė konferencija *Sensors and Electronic Instrumentation Advances* (SEIA 2020), Portas, Portugalija.
- 23-iasis Sde Boker simpoziumas *Solar Electricity Production*, Midreshet Ben Gurion, Izraelis.
- 65-oji Tarptautinė fizikos ir gamtos mokslų studentų konferencija (*Open Readings* 2022), Vilnius, Lietuva.
- 44-oji *Lietuvos nacionalinė fizikos konferencija* (LMFK), Vilnius, Lietuva.
- 17-oji Tarptautinė jaunųjų mokslininkų konferencija *Developments in Optics and Communications* (DOC 2021), Ryga, Latvija.
- 64-oji Tarptautinė fizikos ir gamtos mokslų studentų konferencija (*Open Readings* 2021), Vilnius, Lietuva.

Disertacijos struktūra

Disertaciją sudaro įvadas, analitinė literatūros apžvalga, tyrimo metodologijos aptarimas, apibendrinti tyrimo rezultatai ir išvados, literatūros sąrašas, mokslinių straipsnių priedai, santrauka lietuvių kalba.

Bendras disertacijos puslapių skaičius – 116 puslapių. Darbe pateikta: 43 lygtys, 53 paveikslai, 4 lentelės ir 84 literatūros šaltiniai.

Padėka

Esu nuoširdžiai dėkingas:

Doc. dr. Jonui Gradauskui už pasitikėjimą ir pagalbą kiekviename tyrimo etape.

Doc. dr. Dainiui Jasaičiui už naudingus patarimus parengiant mano tyrimą.

Dr. Jovitai Damauskaitei, prof. dr. Artūrui Juknai, prof. dr. Dariui Ploniui ir prof. dr. Voitechui Stankevičiui už vertingą disertacijos peržiūrą, komentarus ir pastabas.

Vilniaus Gedimino Technikos Universitetui už galimybę parengti šią disertaciją.

Doktorantūros komitetui, visiems mano kolegoms iš Fizikos katedros ir Elektroninių procesų laboratorijos už jų įžvalgias pastabas ir pasiūlymus.

Fizinių ir Technologijos Mokslų Centrui už bandinių gamybą ir galimybę atlikti visus būtinus eksperimentus.

Prof. dr. Eugene Katzui už vadovavimą stažuotės metu Jacobo Blausteino tyrimų institute (Negevo BGU).

Mano šeimai ir draugai už jų paramą ir tikėjimą manimi.

1. Saulės elementų darinių ir karštųjų krūvininkų reiškinio apžvalga

Įvairių kartų ir tipų saulės elementai padeda pritaikyti saulės elementų (SE) technologiją konkrečioms reikmėms ir optimizuoti jų efektyvumą. Skirtingi saulės elementų tipai paprastai apibrėžiami atsižvelgiant į naudojamas medžiagas, vidinę architektūrą bei saulės spektro panaudojimą (Mohammad Bagher et al., 2015). Šie skirtumai apibūdina pirmosios, antrosios ir trečiosios kartos saulės elementus (Ananthakumar et al., 2019).

Pirmoji karta yra seniausias ir dažniausiai naudojamas technologijos tipas, apimantis mono- ir polikristalines saulės elementų konstrukcijas. Monokristalinių saulės elementų efektyvumas šiuo metu siekia 24,2 %, o polikristalinių saulės elementų – 15 % (Akinoglu et al., 2021).

Antrajai kartai priskiriama daugybė plonasluoksnių saulės elementų, pagamintų iš amorfinio silicio, galio arsenido, kadmio telūrido ar vario indžio galio selenido. Šio tipo SE yra lengva gaminti, jie pigūs, nes reikia mažiau medžiagų, jie yra lankstūs, todėl atveria kelius alternatyvioms reikmėms; taip pat jie yra mažiau jautrūs aukštai temperatūrai. Pažymėtinas šių saulės elementų privalumas yra galimybė gaminti juos didelių matmenų, tai atveria dar papildomą kelią jų panaudojimui (Mohammad Bagher et al., 2015).

Trečioji karta apima SE darinius, kurie vis dar yra kūrimo stadijoje. Šie elementai gaminami naudojant įvairias naujas medžiagas ir struktūras, tokias kaip nanovamzdeliai, organiniai sluoksniai, puslaidininkiniai kvantiniai šuliniai / vielos / taškai. Trečioji karta vystoma siekiant pagrindinio tikslo: įveikti Shockley–Queisser ribą ir padaryti saulės elementus labiau komerciškai prieinamus (Conibeer, 2007). Šią kartą sudaro įvairūs saulės spektro panaudojimo pavyzdžiai (Akinoglu et al., 2021): spektrinė konversija (saulės elemento sugeriamo spektro modifikavimas); spektrinis padalijimas (selektyvi saulės spektro sugertis skirtingais absorberiais viename saulės elemente); efektyvus papildomos fotonų energijos surinkimas naudojant energijai selektyvius kontaktus.

Tipiško vienos sandūros saulės elemento nuostoliai skirstomi į dvi grupes: išorinius ir vidinius nuostolius, o šių nuostolių mechanizmų ištyrimas yra būtinas žingsnis siekiant padidinti elementų efektyvumą.

Išoriniai SE nuostoliai apima kontaktų šešėliavimą, nuosekliąją varžą, parazitinę krūvininkų rekombinaciją ir kt. Paprastai išorinius nuostolius galima sumažinti pritaikant inovatyvius gamybos būdus. Vidinius nuostolius sudaro: 1) žemesni už draudžiamosios energijos tarpą, 2) termalizacijos, 3) emisijos, 4) Carnot ir 5) Boltzmann nuostoliai. Šie nuostoliai yra fizinių procesų, vykstančių daugumoje puslaidininkių, pasekmė, ir jų vargu ar įmanoma visiškai išvengti. Verta paminėti, kad termalizacijos ir žemesniųjų už draudžiamosios energijos tarpą nuostolių suma sudaro apie 80 % visų vidinių nuostolių (Hirst & Ekins-Daukes, 2011), tad pirmiausia juos reikia mažinti, kadangi jie yra pagrindinės neefektyvios saulės spektro sugerties priežastys; taip pat juose glūdi ir karštųjų krūvininkų (KK) reiškinys vienos sandūros saulės elementuose.

Karštieji krūvininkai yra laisvieji elektronai ir skylės, sužadinti į nepusiausvyrines didelės energijos būsenas (Ahmed et al., 2021). Apšvietus *p* ir *n* sandūrą fotonais, kurių energija yra mažesnė už draudžiamosios energijos tarpą, šie negali sukurti elektronų ir skylių poros dėl energijos trūkumo. Šiuos fotonus sugeria laisvieji krūvininkai taip tapdami karštaisiais krūvininikais. Fotonai, kurių energija yra lygi arba didesnė už draudžiamosios energijos tarpą, generuoja elektronų ir skylių poras su lygiagrečiai vykstančiu krūvininkų kaitinimo vyksmu.

Anksčiau buvo parodyta (Umeno ir kt., 1978; Wasiak ir kt., 2017; Zanatta, 2019), kad mažesnės už draudžiamosios energijos tarpą energijos fotonų sugertis sukelia vadinamąją anomalią karštųjų krūvininkų fotovoltinę (FV) įtampą, kurios poliškumas yra priešingas įprastajam fotovoltiniam reiškiniui. Stebėtoji KK fotovoltinė įtampa yra būdinga daugumai puslaidininkių medžiagų, naudojamų fotovoltinių įtaisų gamybai.

Apžvelgus tyrimus, susijusius su karštųjų krūvininkų reiškiniu FV įtaisuose, galima apibrėžti šias užduotis:

1. Karštųjų krūvininkų reiškinys vienos sandūros saulės elemente turėtų būti ištirtas siekiant rasti būdus ir sąlygas, leidžiančias nustatyti ir sumažinti šio reiškinio įtaką. Šiuo atveju turėtų būti analizuojama karštųjų krūvininkų efekto priklausomybė nuo temperatūros, priešįtampio ir šviesos spektro, siekiant nustatyti šio efekto ypatybes saulės elementuose.
2. Būtina ieškoti būdų sumažinti spektrinius ir termalizacijos nuostolius dariniuose su *p* ir *n* sandūra.
3. Turėtų būti įvertinta spektro dalis, sugeriama vienos sandūros saulės elementu, kuri gali kaitinti krūvininkus.
4. Reiktų sukurti infraraudonosios spinduliuotės jutiklį, veikiantį karštųjų krūvininkų reiškinio pagrindu.

2. Bandinių gamybos technologija ir tyrimo metodika

Siekiant įvykdyti 1 skyriuje suformuluotas užduotis, tokie bandiniai buvo sukurti:

1. GaAs *p* ir *n* diodai. Viršutinis 5 μm storio *p* tipo sluoksnis (skylių tankis 5×10^{17} cm^{-3}) skystosios fazės epitaksijos būdu užaugintas ant *n* tipo padėklo, kurio elektronų tankis yra 3×10^{17} cm^{-3}. Tradicinė fotolitografijos technologija ir terminis Au-Ge-Ni lydinio garinimas buvo naudojami gaminant $2{,}5 \times 2{,}5$ mm^2 bandinius su ominiais kontaktais. Kontaktai buvo suformuoti bandinio krašte

siekiant išvengti tiesioginio žadinančiojo lazerio spindulio apšvitos, galinčios sugeneruoti fotovoltinį signalą juose.

2. Polikristalinio silicio pramoniniai saulės elementai. Bandiniai išpjauti iš pramoninių Si saulės elementų (SoliTek, Vilnius, Lietuva). Krūvininkų tankis emiteryje ir bazėje yra atitinkamai $n \approx 10^{20}$ cm^{-3} ir $p \approx 10^{16}$ cm^{-3}. Bandinių matmenys yra 2 × 2 mm^2.
3. Akytieji Si diodai, turintys akytąjį paviršinį sluoksnį. Diodai buvo gaminami cheminio garinimo būdu nusodinant *n* tipo epitaksinį Si sluoksnį (elektronų tankis 6×10^{17} cm^{-3}) ant *p* tipo silicio padėklo (skylių tankis 6×10^{16} cm^{-3}). Nanoakytas sluoksnis kuriamas ant *n*-Si paviršiaus naudojant fotokatalitinį elektrocheminį anodinį procesą; elektrolitu naudojamas 1:4 etanolio ir koncentruoto HF (49 %) mišinys. Si paviršiaus elektrocheminis ėsdinimas atliekamas optinėje elektrocheminėje kameroje su Pt tinklelio elektrodu (Ašmontas, Fedorenko et al., 2020).
4. Reketinis jutiklis. Bandiniai pagaminti ant 350 μm storio *n* tipo GaAs plokštelės (elektronų tankis 5×10^{17} cm^{-3}). Du $Al_xGa_{1-x}As$ sluoksniai, kurių AlAs molinė dalis *x* tolygiai keičiasi nuo 0,2 iki 0, išauginti skystosios fazės epitaksijos būdu, palaikant elektronų tankį apie 10^{18} cm^{-3}. Ominiai kontaktai suformuojami fotolitografijos būdu bei garinant ir atkaitinant Au-Ge-Ni lydinį.

Silicis pasirinktas, nes jis yra labiausiai paplitęs puslaidininkis saulės elementų gamyboje, o GaAs – dėl jo 1,42 eV draudžiamosios energijos tarpo, kuris yra artimas optimaliai teorinei didžiausio SE efektyvumo vertei.

Matavimo grandinės schema pavaizduota S2.1 pav. Matavimai atlikti fotosrovės režimu. Apkrovos varža (R = 50 omų) parinkta priderinant prie grandinės impedanso ir siekiant gauti atitinkamas laikines fotoatsako charakteristikas. Matavimams su priešįtampiu buvo pagamintas nuolatinės įtampos šaltinis (0–9 V ir 0–0,3 A).

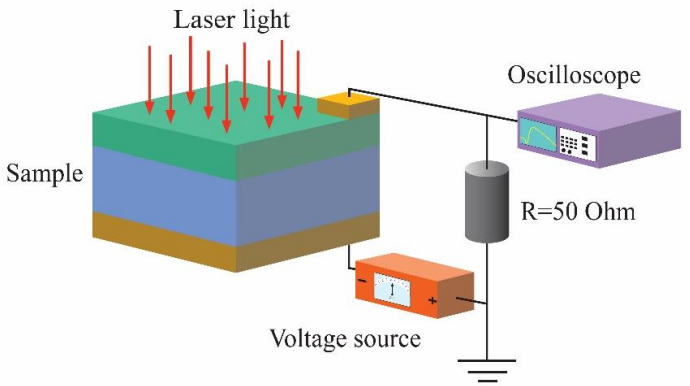

S2.1 pav. Matavimo grandinės schema (sukūrė autorius)

Laikinės fotoįtampos ir lazerio impulsų charakteristikos fiksuojamos skaitmeniniu osciloskopu *Agilent Technologies* DSO6102A, o lazerio impulsų forma – didelės spartos

optinio signalo atskaitos detektoriumi 11HSP-FS1 (*Standa Ltd*., Vilnius, Lietuva). Dviejų rūšių lazeriai buvo naudojami GaAs *p* ir *n* diodų, polikristalinio silicio pramoninių saulės elementų ir reketinio jutiklio bandiniams apšviesti. Neodimiu legiruotas itrio aliuminio granato lazeris buvo naudojamas kaip 1,064 μm ($h\nu$ = 1,17 eV) bangos ilgio spinduliuotės šaltinis; jo būdingi parametrai yra 17–25 ns impulso trukmė ir didžiausias intensyvumas 10 MW/cm^2. Vidutinė lazerio spinduliuotės galia buvo matuojama optiniu galios matuokliu (*Thorlabs Inc*., Naujasis Džersis, JAV). Kitas spinduliuotės šaltinis yra neodimiu legiruotas itrio ortovanadato lazeris; jo parametrai: bangos ilgis 1,342 μm ($h\nu$ = 0,92 eV), impulso trukmė 1,7 ns ir didžiausias intensyvumas 0,4 MW/cm^2. Šviesos intensyvumas buvo keičiamas reguliuojant lazerio kaupinimo galią. Eksperimentai atlikti 80–300 K temperatūrų ruože. Žemos temperatūros sąlygos palaikomos naudojant savadarbį optinį kriostatą.

Si diodų su akytuoju Si paviršiaus sluoksniu fotoįtampos matavimai atliekami nuo 400 iki 1200 nm bangos ilgių diapazone. Šviesa iš halogeninės lempos per monochromatorių ir spindulio skirstytuvą nukreipiama į tiriamąjį bandinį. Taikyta neardomoji metodika, kai naudojamas prispaudžiamas 7 × 7 mm² ploto ITO elektrodas (Kostylyov et al., 2021).

MatLab skaitmeninio skaičiavimo platforma buvo naudojama fotovoltiniam signalui atskirti į komponentus.

3. Karštųjų krūvininkų reiškinio tyrimo rezultatai

Spinduliuotės sukelta fotosrovė (fotoįtampa ant 50 omų apkrovos varžos) (S3.1 pav.) GaAs *p* ir *n* diode gali būti suskirstyta į dedamąsias, darant prielaidą, kad *p* ir *n* sandūra yra tiesinė laike invariantinė sistema (ang. *linear time invariant system*). Čia U_{G} yra fotoatsako dedamoji, atsirandanti dėl elektronų ir skylių porų generavimo, o jos spartą lemia rekombinacijos proceso sparta; U_{hc} yra priešingo poliškumo dedamoji, ji seka lazerio impulso formą; U_{T} yra dedamoji, sukelta gardelės kaitimo, vykstančio dėl karštųjų krūvininkų termalizacijos.

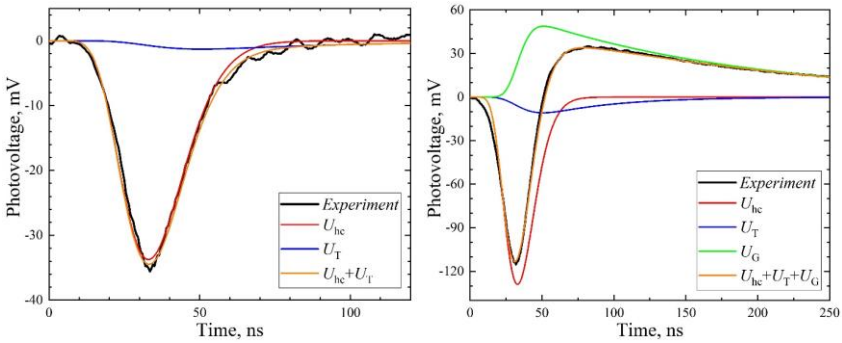

(a) (b)

S3.1 pav. Fotoatsako impulsų modeliavimas esant (a) 51 kW/cm^2 ir (b) 264 kW/cm^2 1,064 μm bangos ilgio sužadinimui. Palyginimui eksperimentinė fotoįtampa parodyta juoda spalva (Gradauskas et al., 2021; Masalskyi & Gradauskas, 2021b)

Verta paminėti, kad U_G dedamosios eksperimentinė vertė yra mažesnė nei modeliuotosios, nes šis skirtumas atsiranda dėl neigiamo ir teigiamo poliškumo fotoįtampų konkuravimo bendrame signale. U_T palaiko U_{hc} esant mažam intensyvumui (žr. S3.1 pav., a), o U_G mažina U_{hc} esant didesniam lazerio intensyvumui (S3.1 pav., b). Lėtosios gardelės kaitimo sukeltos dedamosios U_T indėlis didėja esant aukštesniam sužadinimo lygiui, nes dalis fotono energijos, likusios sugeneravus elektrono ir skylės porą, yra panaudojama krūvininkams kaitinti ir karštųjų krūvininkų fotovoltinei įtampai susidaryti (Gradauskas et al., 2020; Masalskyi et al., 2022a).

Kitas darbas yra skirtas FV įrenginių KK reiškinio ypatumų tyrimui priklausomai nuo priešįtampio, spinduliuotės spektro, temperatūros. Tirtų bandinių voltamperinių charakteristikų kreivės pavaizduotos S3.2 paveiksluose. Rezultatai rodo, kad ilgesnės spinduliuotės bangos atveju GaAs (S3.2 pav., a) trumpojo jungimo srovės, atsirandančios dėl generavimo, dydis sumažėja 20 kartų, o karštųjų krūvininkų srovės – tik 15 kartų, nes fotono energijos pokytis arčiau draudžiamosios energijos tarpo yra lydimas stipresnės tarpjuostinės sugerties lyginant su vidje-juostine sugertimi (Dargys & Kundrotas, 1994). Si bandinyje, apšviestame 1,064 μm lazerio šviesa (3.2 pav., b), generacijos fotosrovė yra daug stipresnė nei karštųjų krūvininkų (fotono energija yra didesnė už draudžiamosios energijos tarpą), o KK fotosrovę galima detektuoti tik esant dideliam tiesioginiam priešįtampiui, kai potencialo barjeras yra gana žemas.

Akivaizdu, kad tiesioginė įtampa yra palanki karštųjų krūvininkų srautui per sumažintą *p* ir *n* sandūros potencialinį barjerą. Verta paminėti, kad didžiausios galios režimu SE veikia esant tiesioginei įtampai, o tai sudaro palankias sąlygas karštųjų krūvininkų fotosrovei tekėti, taigi kartu daro neigiamą įtaką efektyviam saulės elemento veikimui.

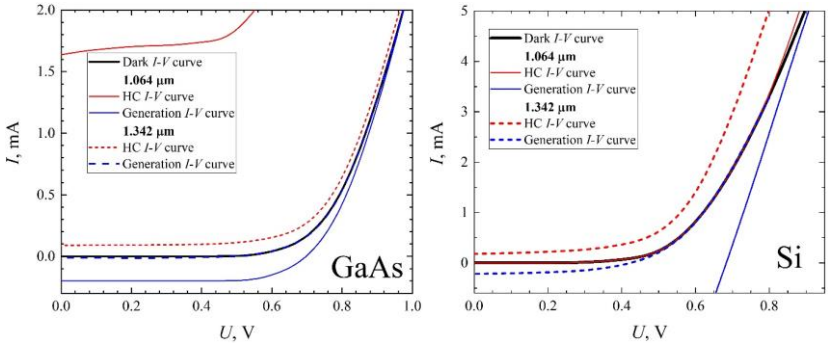

(a) (b)

S3.2 pav. (a) GaAs ir (b) Si *p* ir *n* sandūrų voltamperinės charakteristikos. Juoda kreivė žymi priklausomybę tamsoje, raudona kreivė rodo KK fotosrovę, mėlyna kreivė atitinka fotosrovę, sukeltą elektronas-skylė porų susidarymu (Masalskyi, Gradauskas, Ašmontas, Sužiedėlis, Šilėnas et al., 2021; Masalskyi, Gradauskas, Ašmontas, Sužiedėlis, Širmulis et al., 2021)

Siekiant įvertinti karštųjų krūvininkų temperatūrą GaAs *p* ir *n* sandūroje, buvo sukurta vadinamoji voltamperinės charakteristikos temperatūrinio įtampos koeficiento metodika. Šis koeficientas atitinka įtampos kitimo vienam temperatūros laipsniui vertę esant

pastoviai srovei ir yra pastovus tai pačiai medžiagai, kurios temperatūra viršija 20 K. Nustatytoji GaAs *p* ir *n* sandūros temperatūrinio koeficiento vertė yra lygi –2,2 mV/K, kuri yra artima kitų šaltinių vertei –2,0 mV/K (Landis et al., 2011). Darant prielaidą, jog aplinkos temperatūra lygi 300 K, gauta karštųjų krūvininkų temperatūra yra 454 K. Taikant tą pačią metodiką, karštųjų krūvininkų temperatūra skystajame azote nustatyta esanti lygi 262 K. Pažymėtina, kad skystajame azote krūvininkai pakaitinami apie 182 K, o kambario temperatūroje – tik apie 154 K. Tai rodo, kad krūvininkų kaitinimo procesas yra stipresnis esant žemai temperatūrai, tai susiję su karštųjų krūvininkų energijos relaksacijos trukmės pailgėjimu žemėjant temperatūrai (Dargys & Kundrotas, 1994).

Norint nustatyti karštųjų krūvininkų srovės tekėjimo pobūdį, buvo skaičiuojamas laisvųjų krūvininkų užimtų būsenų tankis (esant anksčiau įvertintai temperatūrai) *p* ir *n* sandūros *n* ir *p* srityse. Laisvųjų krūvininkų užimtų būsenų didžiausiosios vertės yra daug mažesnės nei potencialo barjero aukštis. Tai patvirtina hipotezę, kad karštieji krūvininkai nedifunduoja per barjerą, o srovė greičiausiai turi rekombinacinį pobūdį. Be to, šią prielaidą patvirtina ir faktas, kad net atskiras 1,064 μm ilgio sužadintas elektronas neturi pakankamai energijos, reikalingos difunduoti per potencialinį barjerą.

Įrodžius karštųjų krūvininkų fotosrovės buvimo faktą pramoniniuose saulės elementuose, apskaičiuojama sugertos saulės spinduliuotės spektro dalis, kuri naudojama krūvininkams kaitinti. Tirtos medžiagos taip pat yra Si ir GaAs. Skaičiavimų rezultatai rodo, kad 19,0 % viso saulės AM 1,5 G spektro, priskiriamo mažos energijos fotonams (kurių energija mažesnė už draudžiamosios energijos tarpą), ir 33,2 % didelės energijos fotonų prisideda prie krūvininkų kaitinimo silicyje. Galio arsenido atitinkamos vertės yra 33,0 % ir 21,7 %. Tai reiškia, kad net ir darant prielaidą, jog saulės elementas sugeria visą AM 1,5 G saulės spektro spinduliuotę, daugiau nei pusė jos potencialiai gali kurti karštuosius krūvininkus. Atsižvelgus į spinduliuotės sugertį medžiagoje, 59,8 % AM 1,5 G fotonų, turinčių energiją $hv > E_g$, panaudojama krūvininkams kaitinti silicyje. Nedidelis kiekis, tik 0,5 % absorbuotų fotonų, turinčių $hv < E_g$ energiją, naudojama krūvininkams kaitinti. Kalbant apie GaAs, 36,5 % absorbuotų AM 1,5 G didelės energijos fotonų yra priskiriami krūvininkams kaitinti; atitinkamai mažos energijos fotonų dalis yra 0,2 %. Skaičiavimai atlikti neatsižvelgiant į šviesos atspindį ir darant prielaidą, kad visi absorbuoti mažos energijos fotonai kaitina tik laisvuosius krūvininkus. Taigi, norint parodyti, kokia reikšminga gali būti ši sugertis, metodika taikyta tipiškam *n* tipo SE emiteriui, kurio krūvininkų tankis yra iki 10^{20} cm^{-3} ir storis 0,5 μm. Šiuo atveju absorbuoto saulės spinduliuotės AM 1,5 G spektro dalis, atitinkanti mažesniosios energijos fotonus, gali būti didesnė nei 4 %, o ši fotonų energija kaitina laisvuosius krūvininkus ir sukelia karštųjų krūvininkų fotosrovę ir vėliau vyksta gardelės kaitimas. Todėl yra slopinama klasikinė generacijos nulemta fotosrovė (Masalskyi & Gradauskas, 2022).

Ankstesni rezultatai atskleidė, kad karštųjų krūvininkų reiškinio įtaka bendrajam vienos sandūros saulės elementų elektriniam signalui turėtų būti sumažinta. Siekiant to, buvo pasiūlytas darinys su ant tipiško saulės elemento paviršiaus suformuotu varizoniniu puslaidininkiniu sluoksniu. Dėl kvantinio apribojimo reiškinio draudžiamosios energijos tarpas priklauso nuo jo matmenų; kintant puslaidininkio konstrukcijos matmenims, kinta ir energijos tarpas. Akytojo Si (PSi) sluoksnis buvo formuojamas Si *p* ir *n* diodo priekinėje pusėje. S3.3 pav., a, parodyta talpinės fotoįtampos spektrinė priklausomybė su viršutiniu

PSi sluoksniu ir be jo, o S3.3 pav., b, schemiškai paaiškintas fotoįtampų susidarymas (Ašmontas, Fedorenko et al., 2020).

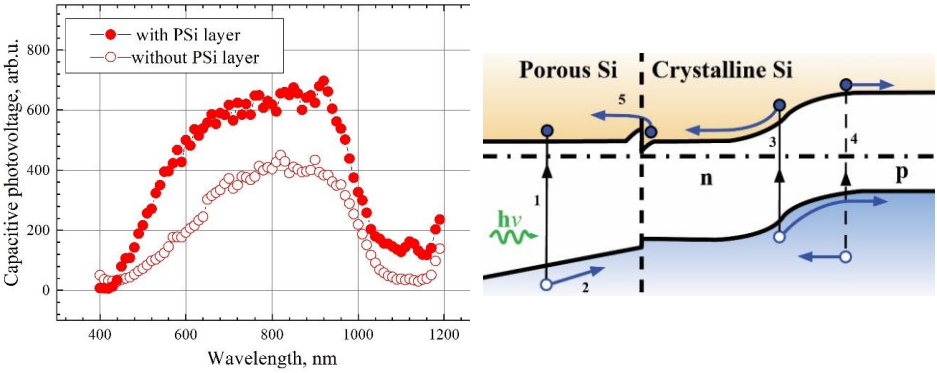

(a) (b)

S3.3 pav. (a) Talpinės fotoįtampos Si *p* ir *n* sandūroje spektrai be (tušti taškai) paviršinio PSi sluoksnio ir su juo (pilni taškai); (b) fotoįtampų susidarymo mechanizmai: 1 – elektrono ir skylės poros generavimas didelės energijos fotonu, 2 – skylės dreifas PSi varizoninio sluoksnio elektriniame lauke, 3 – klasikinis fotovoltinės įtampos susidarymas *p* ir *n* sandūroje, 4 – elektrono ir skylės generavimas didelės energijos fotonu ir atitinkamas karštųjų krūvininkų fotoįtampos susidarymas *p* ir *n* sandūroje, 5 – fotoįtampų susidarymas ties Psi / kristalinis Si riba (Masalskyi & Gradauskas, 2022)

Sukurtame darinyje bendra fotoįtampa didėja ne tik dėl sumažėjusio atspindžio, bet ir dėl papildomų 1, 2 ir 5 procesų (S3.3 pav., b); abiejų šių fotoįtampų poliškumas yra toks pat kaip ir klasikinės fotovoltinės įtampos (3 procesas). S3.3 pav., a, stebimas fotoįtampos padidėjimas trumpųjų bangų srityje atsiranda dėl varizoninio sluoksnio, kuris efektyviau sugeria didelės energijos fotonus (1 ir 2 procesai) ir taip sumažina žalingą karštųjų krūvininkų poveikį, parodytą 4 procesu. Be to, varizoninio sluoksnio vidiniame elektriniame lauke sugeneruotos skylės dreifuoja (2 procesas) taip išvengdamos didelės rekombinacijos. Galiausiai karštųjų krūvininkų fotoįtampa, susidaranti Psi / *n*-Si sandūroje, išplečia efektyvųjį spektrą ilgųjų bangų srityje (S3.3 pav., 5 procesas).

Kadangi viduj-juostinė ($hv < E_g$) spinduliuotės sugertis yra viena iš karštųjų krūvininkų fotosrovės atsiradimo priežasčių, ji gali būti naudojama infraraudonajai spinduliuotei detektuoti. Remiantis šia idėja, pasiūlyta jutiklio struktūra, veikianti karštųjų krūvininkų reiškinio pagrindu. Reketu pagrįstas varizoninis $GaAs/Al_{0.2}Ga_{0.8}As$ jutiklio darinys gali detektuoti elektromagnetinės spinduliuotės ilgųjų bangų ruožą. Sukurtojo jutiklio darbo režimas nereikalauja kriogeninių temperatūrų palaikymo ir sudėtingos gamybos technologijos. Fotosrovės impulso laikinė charakteristika parodyta S3.4 pav.

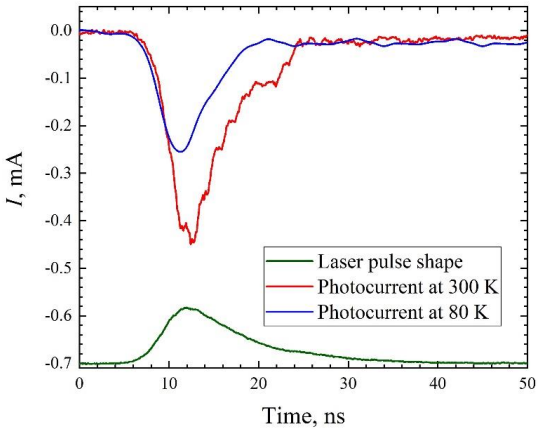

S3.4 pav. Reketiniame jutiklyje indukuotos fotosrovės impulsas, apšviečiant 1,064 μm lazerio spinduliuote, esant 7,5 MW/cm^2 intensyvumui. Žalia linija rodo lazerio impulso formą (sąlyginiais vienetais), mėlyna linija rodo fotosrovę esant 80 K temperatūrai, o raudona linija žymi fotosrovę esant 300 K temperatūrai (sukūrė autorius)

Jutiklis yra spartus – jo atsakas seka lazerio impulso signalą. Sukurtojo jutiklio atsakas tiesiškai priklauso nuo šviesos intensyvumo, o tai irgi yra privalumas taikymo atvejais. Elektrinio atsako signalo sumažėjimas 80 K temperatūroje, lyginant su 300 K, matyt, yra susijęs su GaAs absorbcijos koeficiento ir laisvųjų krūvininkų tankio sumažėjimu žemose temperatūrose (Dargys & Kundrotas, 1994). Šis jutiklis gali būti naudojamas įvairiuose darbinės temperatūros diapazonuose, nes jo draudžamosios energijos tarpo kitimas yra nereikšmingas (potencialinio barjero aukštis keičiasi tik 0,3 meV, kai temperatūra kinta nuo 80 K iki 300 K).

Bendrosios išvados

1. Saulės elemento fotoatsako padalijimo modelis rodo, kad bendras signalas yra sudarytas iš trijų dedamųjų, kurias sukelia elektronų-skylių porų generavimas, krūvininkų kaitimas ir gardelės kaitimas. Modelis rodo karštųjų krūvininkų reiškinio individualią įtaką bendrajam signalui. Įrodyta, kad karštieji krūvininkai indukuoja signalą prieš atiduodami papildomą savo energiją kristalinei gardelei kaitinti. Šis rezultatas patvirtina, kad karštųjų krūvininkų reiškinys turi būti laikomas nauja savųjų nuostolių rūšimi saulės elementuose.
2. Apskaičiuota karštųjų krūvininkų pasiskirstymo statistika panaudojant įvertintą krūvininkų temperatūrą rodo, kad karštųjų krūvininkų fotosrovė tekanti per GaAs *p-n* sandūrą, esant +0,7 V tiesioginei įtampai, yra rekombinacinjos prigimties, nes pakaitinti laisvieji krūvininkai užima energijos būsenas, kurios yra daug žemesnės už sumažintą bet vis dar aukštą sandūros potencialinį barjerą
3. Fotonų, kurių energija yra mažesnė nei draudžiamosios energijos tarpas, sugertis turi potencialą kaitinti laisvuosius krūvininkus kaip ir didesnės už tarpą energijos

fotonų sugertis. Šis faktas reikalauja peržiūrėti Shockley–Queisser ribą, įskaitant ir mažos energijos fotonų sugertį.

4. Reketinis puslaidininkinis varizoninis darinys gali būti naudojamas kaip infraraudonosios spinduliuotės jutiklis, veikiantis karštųjų krūvininkų reiškinio pagrindu kambario temperatūroje. Sukurto jutiklio išėjimo fotosignalas tiesiškai priklauso nuo šviesos intensyvumo, o tai yra patogu prietaiso kalibravimui.

Oleksandr MASALSKYI

INVESTIGATION AND APPLICATION OF HOT CARRIER PHENOMENON IN PHOTOVOLTAICS

Doctoral Dissertation

Technological sciences,
Electrical and electronic engineering (T 001)

KARŠTŲJŲ KRŪVININKŲ REIŠKINIO TYRIMAS IR PANAUDOJIMAS FOTOVOLTIKOJE

Daktaro disertacija

Technologijos mokslai,
elektros ir elektronikos inžinerija (T 001)

Lietuvių kalbos redaktorė Dalia Markevičiūtė
Anglų kalbos redaktorė Jūratė Griškėnaitė

2023 11 14. 9,5 sp. l. Tiražas 20 egz.
Leidinio el. versija *https://doi.org/10.20334/2023-046-M*
Vilniaus Gedimino technikos universitetas
Saulėtekio al. 11, 10223 Vilnius
Spausdino UAB „Ciklonas“,
Žirmūnų g. 68, 09124 Vilnius